

# Spectroscopic Study of Electron Transfer Processes in Transmission of Highly Charged Ions through Microcapillaries

Yuichiro Morishita \*

Institute of Physics, School of Science, University of Tokyo

March 30, 2003

\* e-mail: [morisita@radphys4.c.u-tokyo.ac.jp](mailto:morisita@radphys4.c.u-tokyo.ac.jp)

# Contents

<b>1</b>	<b>Introduction</b>	<b>3</b>
1.1	Overview . . . . .	3
1.2	Slow Highly Charged Ions . . . . .	4
1.3	Historical review . . . . .	5
1.3.1	Earlier Recognition of Neutralization . . . . .	5
1.3.2	Below Surface Neutralization . . . . .	8
1.3.3	Classical Over Barrier Model . . . . .	14
1.3.4	Above Surface Neutralization . . . . .	17
1.4	Insulator and Capillary Surface . . . . .	20
1.4.1	Insulator Surface . . . . .	20
1.4.2	Capillary Surface . . . . .	21
1.5	Motivation for Visible Light Spectroscopy . . . . .	26
<b>2</b>	<b>Experiment</b>	<b>29</b>
2.1	Ion Source . . . . .	29
2.2	Beam Line . . . . .	33
2.3	Experimental Set-up . . . . .	34
2.3.1	Preliminary Set-up . . . . .	34
2.3.2	Improved Set-up . . . . .	38
2.3.3	Wavelength and Resolution . . . . .	40
2.3.4	Data Acquisition . . . . .	43
2.3.5	Intensity Calibration . . . . .	45
<b>3</b>	<b>Spectroscopic Study</b>	<b>48</b>
3.1	Overall spectra . . . . .	48
3.2	High Resolution Spectrum . . . . .	51
3.2.1	Light from Sputtered Particles . . . . .	52
3.2.2	Light from HCI with multiple electrons transferred . . . . .	55
3.2.3	Light from HCI with a High Rydberg Electron . . . . .	55
3.2.4	Core Polarization Method . . . . .	58
3.2.5	Multi-Configuration Hartree-Fock Method . . . . .	61

3.3	Advantage of Capillary Technique . . . . .	69
3.4	Summary of Spectroscopy . . . . .	71
<b>4</b>	<b>Initial Population</b>	<b>73</b>
4.1	Rate Equation . . . . .	73
4.1.1	Transition Rates and Lifetimes . . . . .	75
4.2	Decay-curve Measurements . . . . .	76
4.3	Initial Population . . . . .	84
4.3.1	Stark Effect . . . . .	87
<b>5</b>	<b>Summary</b>	<b>93</b>
<b>A</b>	<b>Polarization Formula</b>	<b>94</b>
<b>B</b>	<b>Z-dependent Perturbation Theory</b>	<b>96</b>
<b>C</b>	<b>Ar<sup>Q<sub>in</sub>+</sup> Spectra</b>	<b>98</b>
<b>D</b>	<b>Remark</b>	<b>108</b>
D.1	Atomic Units . . . . .	108
D.2	Conversion of Energy . . . . .	109
D.3	Spectroscopic Notation . . . . .	109
D.4	Terminology . . . . .	110
	<b>Acknowledgment</b>	<b>111</b>

# Chapter 1

## Introduction

### 1.1 Overview

When a slow highly charged ion (HCI) approaches a metal surface, the HCI is neutralized through the successive electron transfer from the surface. The characteristic time involved in the neutralization is determined crucially by the image acceleration toward the surface and is evaluated to be quite short ( $\lesssim 10^{-13}$  sec). Most of the experimental studies of the neutralization have been performed using a flat metal surface, and as a result, have been limited only to measurements of reflected atoms, X-rays and Auger electrons (whose inverse transition rates should be shorter or comparable to the characteristic time). These measurements mainly revealed the last (X-rays and Auger electrons) or whole (reflected atoms) processes of the neutralization, however the initial and middle processes of the neutralization have not because of the short characteristic time and the flat surface.

To overcome the difficulty, we made use of a so-called micro-capillary foil as a target. The foil is thin ( $\sim 10 \mu\text{m}$ ) in thickness and has a multitude of straight capillaries (diameter  $\sim 100$  nm) perpendicular to the surface. Although the image acceleration is unavoidable even with the foil, it was expected that (1) HCIs impinging along the capillary capture electrons at the exit of the capillary and transmit into the vacuum, (2) the number of the captured electrons depends upon the distance between the capillary wall and the HCIs at the exit and hence (3) the initial and middle processes of the neutralization can be studied with the micro-capillary foil. It is noted here that because HCIs with some electron transferred are in the vacuum, even transitions with their lifetimes longer than the characteristic time can be observed.

We determined to focus on the initial process with the capillary foil in this study. For this purpose, we measured visible light emitted from the HCI in the vacuum which has captured only one electron in the capillary, and then evaluated the initial  $(n, \ell)$  distribution of the captured electron by analyzing the cascade of the transitions. It is worth noting again that transition rates are typically  $10^9 \text{ sec}^{-1}$  in the visible light

region, hence visible light measurement is feasible only with the micro-capillary foil (compare with the characteristic time). The results reveals for the first time that the average  $n$  values are consistent with the classical over barrier model (*i.e.*,  $n \approx Q_{in}$ , where  $Q_{in}$  is the incident charge). Further it is found that (1) the width of the distribution ( $\delta n$ ) is around 2 and (2) the angular momentum ( $\ell$ ) distributions are more or less statistical.

## 1.2 Slow Highly Charged Ions

Interaction between a slow highly charged ion (HCI) with matters, *e.g.*, atoms, molecules or surfaces has been one of the rapidly growing research fields in atomic physics. Its importance is closely related to many other physical fields like radiation-, plasma-, astro-, surface-... physics. Here the terms “*slow*” or “*fast*” refer physically to velocity of the HCI slower or faster than those of electrons involved in the interactions. In the fast HCI collisions, kinetic energy of the HCI is one of the most important parameters and the energy transferred to each of constituting atoms is supplied mainly from the kinetic energy. It is well known that the Born approximation is applicable to sufficiently fast collisions [1]. In many cases of the slow HCI collisions, on the other hand, the potential energy stored in the HCI becomes comparable or even larger than the kinetic energy of the HCI. For example, a fully-stripped  $U^{92+}$  ion has a potential energy of  $\sim 800$  keV. What will happen when such a slow HCI approaches closely to the matters ? At a larger distance where an overlap between the wave functions of the HCI and matters can be neglected, electrons in the matters start to rearrange their distribution through polarization, and at a smaller distance some of electrons are transferred to the HCI. As a result, the matters are charged, which means that part of the potential energy stored initially in the HCI is also transferred to the matters. After the electron transfer, a part of the potential energy further dissipates as photons and/or Auger-electrons.

In surface collisions, in fact, there is a specific difference from atomic or molecular collisions. While the total charge is conserved in atomic/molecular collisions, the charge conservation is less important in surface collisions because the solid can be regarded to have infinite number of electrons and the electrons correct disturbed charge distribution quite fast ( $\sim 10^{-15}$  sec) when a metal surface is used. As a result, the HCI is completely neutralized and the potential energy of the HCI dissipates around the surface. It is known that an area to which the potential energy is deposited is  $\sim 100$  nm<sup>2</sup> and the time interval of the neutralization is  $\sim 10^{-13}$  sec at longest. This corresponds to a density of energy flow with  $\sim 10^{17}$  J/sec·m<sup>2</sup> (for  $U^{92+}$ ).

In the following sections, some experimental and theoretical works remarkable for understanding of the neutralization of the HCI are described as an introduction of the present study.

## 1.3 Historical review

### 1.3.1 Earlier Recognition of Neutralization

Study of neutralization of a slow highly charged ion in front of a metallic surface was started by Arifov et al. [2, 3] in the early 1970's after the pioneering work by Hagstrum using singly or doubly charged ions [4]. At the time, total secondary electron yields,  $\gamma_{Q_{in}}$ , were mainly measured when HCIs impinge onto metal surfaces with kinetic energies,  $(10 - 15) \times Q_{in}$  keV, where  $Q_{in}$  is the incident charge of the HCI. As is shown in Figs. 1.1(A) and (B), Arifov et al. found that  $\gamma_{Q_{in}}$  can be scaled as [2, 3, 5],

$$\gamma_{Q_{in}} \propto Q_{in}^2 \propto \sum_{i=1}^{i=Q_{in}} V_i(Q_{in}, Z), \quad (1.1)$$

where  $V_i(Q_{in}, Z)$  is the  $i$ -th ionization energy of the HCI with its nuclear charge  $Z$ . The results are explained by extending the semi-empirical model given by Hagstrum [4]. Two elementary processes, *i.e.*, one- and two-electron transfer processes which are shown in Figs. 1.2(A)-(G), are taken into account to explain the whole neutralization process.

In the one-electron processes, the most important process was assumed to be Resonant Neutralization (RN in Fig. 1.2(A)) \*, where free electrons in the metal resonantly tunnel through the potential barrier to an excited state of the HCI when a wave function of the excited state extends to the surface,

$$d \approx r_n \approx \frac{n^2}{Q_{in}}, \quad (1.2)$$

where  $d$  is a distance of the HCI from the surface and  $r_n$  is the orbital radius of the excited state with a principal quantum number,  $n$ , (Atomic units are used throughout the thesis unless otherwise noted). When the topmost electrons in the valence band are involved in the RN process, the electron is transferred to the same energy level of the ions,

$$W \approx \frac{Q_{in}^2}{2n^2}, \quad (1.3)$$

where  $W$  is the work-function of the surface. Here it is noted that although energy levels of the HCI are shifted upward due to its image charge induced on the surface, it was neglected in Eq. 1.3. Equations 1.2 and 1.3 show that both  $d$  and  $n$  are

---

\* Although it is valid to use RN for the electron transfer to the singly charged ion, traditionally RN has been used even for an electron transfer to the highly charged ions

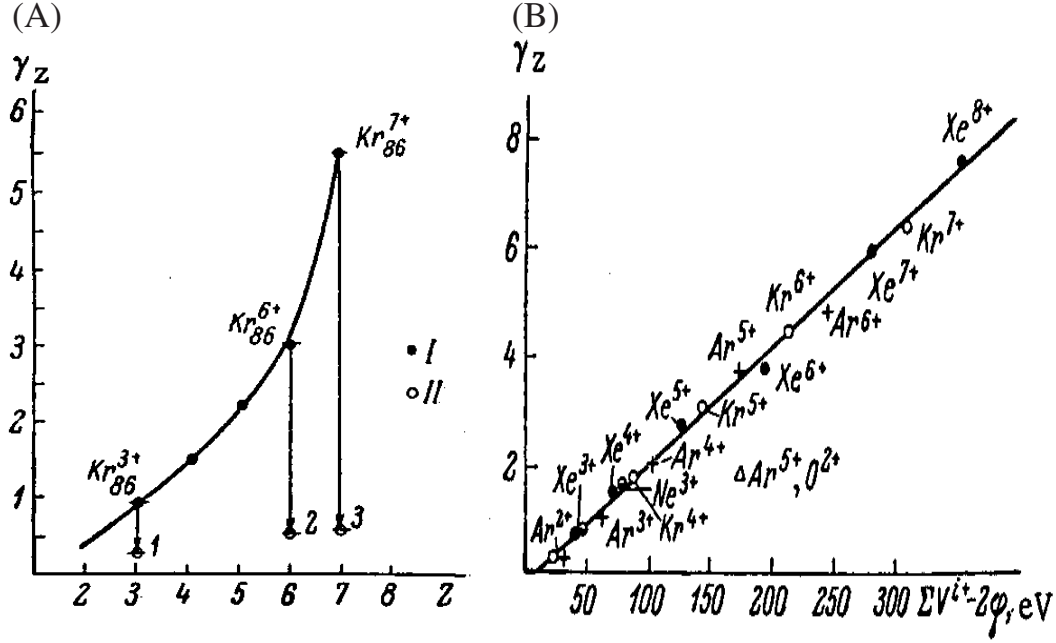


Figure 1.1: Total secondary electron yield as a function of incident charge  $Z$  (A) and that as a function of the total potential energy stored in the HCIs (B) [2].

proportional to the charge of the ions, *i.e.*,

$$d \approx r_n \approx \frac{Q_{in}}{2W}, \quad n \approx \frac{Q_{in}}{\sqrt{2W}}. \quad (1.4)$$

For example, when  $Q_{in} = 10$  and  $W = 0.2$  a.u.,  $n$  and  $d$  are estimated to be 16 and 25 a.u., respectively. When the HCI further approaches the surface, the energy level is shifted upward because of the image interaction and the transferred electrons can be transferred back to the metal if there are empty states available (Resonant Ionization in Fig. 1.2(B)). When deep atomic states of the HCI exist close to tightly bound states in the metal, Quasi-Resonant Neutralization (QRN in Fig. 1.2(A)) can take place. When  $Q_{in}$  is large enough, Radiative De-excitation after RN or that involving metal electrons can take place (Figs. 1.2(C) and (D)), because radiative transition rates for hydrogen-like ions increases with the fourth power of  $Q_{in}$ .

The two-electron processes consist of three kinds of Auger processes, Auger Neutralization, Auger De-excitation and Auto-Ionization. In Auger Neutralization (AN in Fig. 1.2(E)), two electrons in the conduction band collide with each other, and one electron tunnels into a vacant state of the HCI in front of the surface, and the other electron is emitted because of energy conservation. In Auger De-excitation (AD in Fig. 1.2(F)), an electron is initially bound in an excited state of HCI, which is formed, for example, via the RN process and the other electron is in the conduction band. Then an electron in the HCI is emitted when an electron in the metal tunnels into a deeper state of the HCI. In Auto-Ionization (AI in Fig. 1.2(G)), two electrons are bound in

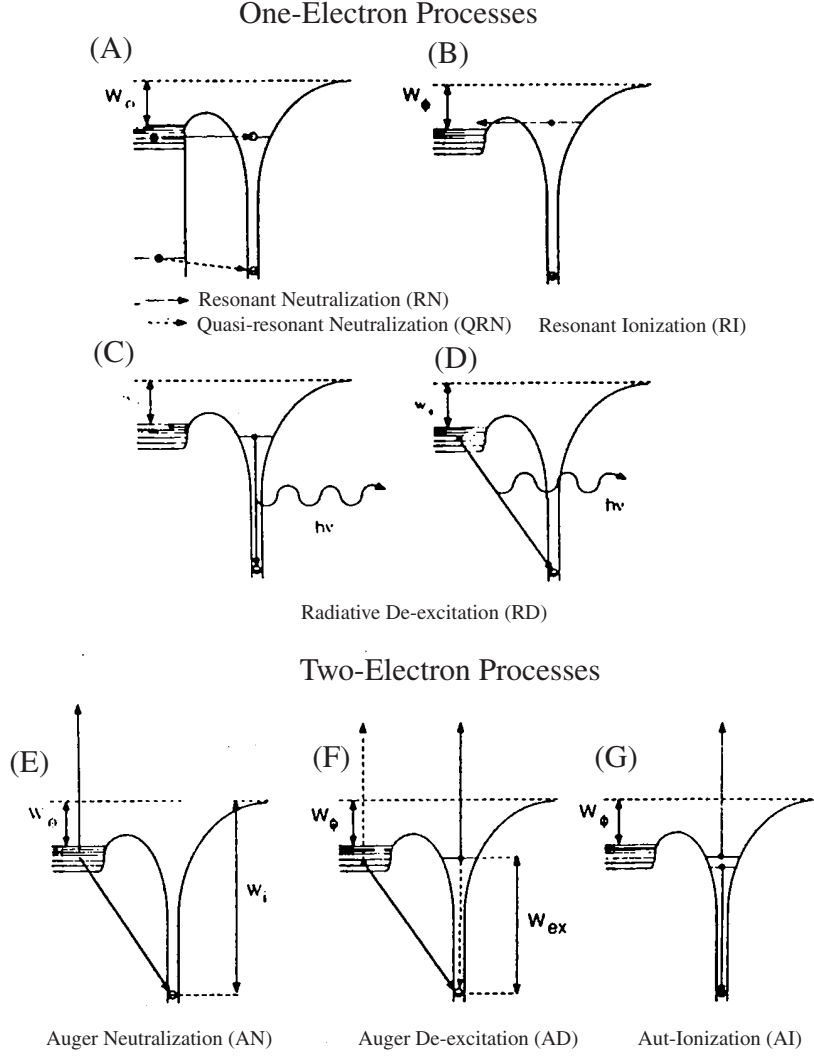


Figure 1.2: Possible and elementary electron transfer-, ionization- and de-excitation-processes for ions in front of the metallic surface [5].

excited states of the HCI, and one electron is emitted at the same time as a transition of the other electron to a lower state.

Among these elementary processes, RN, AN, AD and AI processes were thought to play important roles in the neutralization processes, *i.e.*, electrons are supplied into highly excited states of the HCI by RN and AN processes, and the potential energy stored in the HCI dissipates step-wisely by Auger electron emission through AD and AI processes. It is known that most of the Auger electrons have much lower energies around 10 eV than the sum of the ionization potentials ( $\sum V^i$ ). This means that the total potential energy dissipates dominantly through many Auger electrons which is the main reason for the observed proportionality between  $\gamma_Q$  and  $\sum V^i$ .

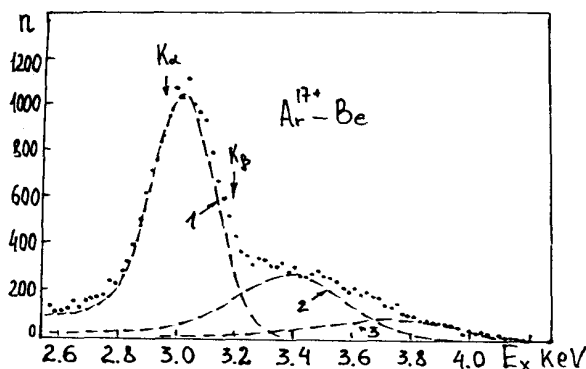


Figure 1.3: X-ray spectrum when  $\text{Ar}^{17+}$  ions were incident onto a beryllium target [13].

### 1.3.2 Below Surface Neutralization

In 1990's, invention and development of small but higher intensity and higher charge state ion sources enhanced the study of the interaction of HCIs with surfaces. As a result, more realistic scenario for neutralization of the HCIs has been developed (comprehensive reviews are found in Refs [6, 7, 8, 9, 10, 11]). In this section, neutralization processes of HCIs below the surface are introduced.

#### X-ray measurement

Donets, who invented the Electron Beam Ion Source (EBIS), first observed  $K$  X-rays with a semiconductor (Ge) X-ray detector when  $2.8 \times 10^5$  m/s  $\text{Ar}^{17+}$  (hydrogen-like) ions <sup>†</sup> were incident upon a beryllium target [13]. Figure 1.3 shows the resultant spectrum where arrows labeled by  $K_\alpha$  and  $K_\beta$  shows the energy positions for  $2p - 1s$  and  $3p - 1s$  transitions of the neutral argon atom whose  $L$  shell is completely filled. As is clearly seen, the observed  $K_\alpha$  peak shifts toward higher transition energy than the arrow labeled by  $K_\alpha$ . It was concluded referring to calculated data [14] that the shift results from incomplete filling of the  $L$  shell at the moment of  $K$  X-ray emission and the half width of the  $K_\alpha$  peak can be explained by changing the electron numbers in the  $L$  shell from 1 to 8.

To study the broad  $K_\alpha$  peak in Fig. 1.3 in more detail, Briand et al. measured  $K$  X-rays with a high resolution crystal spectrometer for 8.5 keV/amu  $\text{Ar}^{17+}$  ions incident normal to a silver surface ( $v_\perp = 1.3 \times 10^6$  m/s;  $v_\perp$  is the ion velocity perpendicular

<sup>†</sup> Crudely speaking of atoms with a  $K$ -shell vacancy, while Auger transition rates have a weaker dependence upon the atomic numbers ( $Z$ ) and the rates are  $\sim 10^{15}$  sec<sup>-1</sup>, radiative transition rates become larger as  $Z^4$ . For example, a ratio between radiative and Auger transition rates for Ar atoms with a  $K$ -shell vacancy is  $\sim 0.1$  [12], which makes it possible to study neutralization even with radiative transitions.

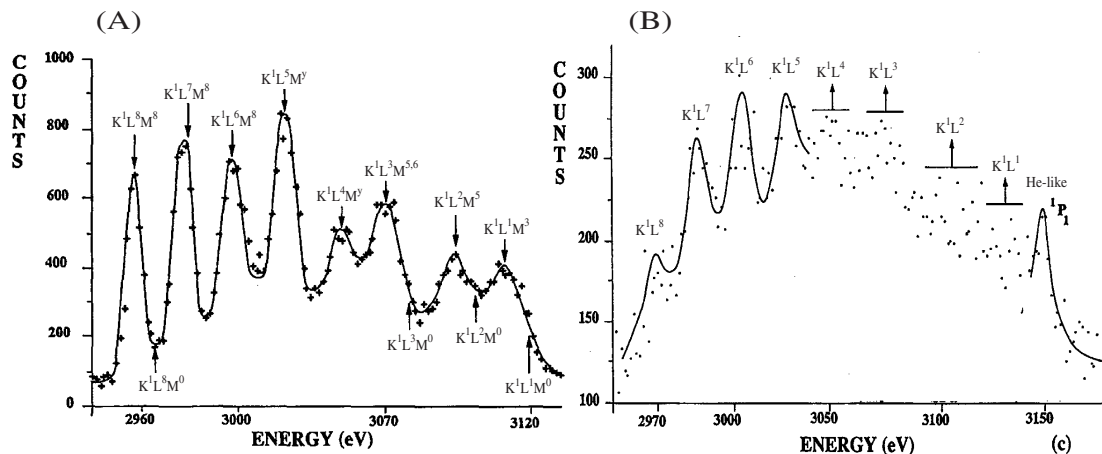


Figure 1.4: High-resolution spectra [16] observed with  $Ar^{17+}$  ions impinging on a silver target at normal incidence (A) and grazing angle incidence, ( $3^\circ$ ), (B)

to the surface) [15]. Figure 1.4(A) shows the observed spectrum <sup>‡</sup>, which exhibits eight separable peaks. Briand et al. identified these peaks comparing their energies with those calculated by a Dirac-Fock code. The initial electronic configurations of the transitions are shown like  $K^1L^xM^y$  in the figure. It is seen that the  $K$  and  $L$  shells are incompletely filled, and  $M$  shell is completely filled for  $L$ -shell populations greater than  $\sim 5$ . Such strange atoms/ions with sparsely filled inner-shells and filled outer-shells are called *Hollow Atoms* (HAs) and gather much attention.

At the time when the HAs were observed, it became a problem whether the HAs emit such X-rays above the surface, or below the surface (hollow atoms above and below the surface are referred to as HA1 and HA2 hereafter). Briand et al. considered that the X-rays are emitted from the HA2s by the following reasons. Firstly because of the large velocity of the ions normal to the surface, there is not enough time to populate the  $L$  shell through cascading from highly and multiply excited states discussed in Section 1.3.1. According to their calculation, Auger lifetimes for  $nl n' \ell'$  ( $n, n' \approx 10 - 20$ , and  $\ell, \ell' = 0$ ) states are around  $10^{-13}$  sec, which are longer than a survival time of HA1s, *i.e.*, time between the beginning of the electron capture and crushing onto the surface ( $t \lesssim 2 \times 10^{-14}$  sec). Secondly, energy levels of  $N$  shell ( $56 < E_N < 95$  eV) or  $M$  shell ( $367 < E_M < 712$  eV) of the silver target are close to those of  $3 \leq n < 7$  shells for Ar ion when Ar ion approaches the target atoms at distances of the order of 0.5 to 3 a.u. (the half inter-atomic distance of the target is 2.5 a.u.), where the capture cross section is so large ( $\sigma \approx 10^{-14}$  cm<sup>2</sup>) that many electrons are transferred in these shells. Such a process is called a side-feeding process [17] which is consistent with the observed lines reflecting many  $M$  spectator electrons.

<sup>‡</sup> This spectrum was copied from Ref. [16] with incident energy of 7.2 keV/amu. However overall features of the line intensities look the same.

Later, Briand et al. measured a similar spectrum under grazing angle collision of  $3^\circ$  ( $v_\perp = 6.7 \times 10^4$  m/s) to search signals from HA1s (the grazing angle is defined with respect to the surface plane). The resultant spectrum is shown in Fig. 1.4(B) [16]. It is noted that the incident ions inevitably crush into the solid and hence the observed lines result from both HA1s and HA2s. In Fig. 1.4(B), while the widths of  $KL^{8-5}$  lines look similar to those in Fig. 1.4(A),  $KL^{1-4}$  lines scatter (broaden). This means that the number of spectator electrons in the  $M$  shell has a broader distribution than that for the normal incidence. In addition, the  $KL^1M^0$  ( $^1P_1$ ) component were observed clearly. Because  $M$  shell is quickly filled below the surface, these features indicate that  $M$  shell is populated not only by the side-feeding process but also by cascading AI processes from upper levels, *i.e.*, signals from HA1s also contribute to the spectrum.

Briand et al. further noted that intensities of  $KL^{5-8}$  lines relative to  $KL^{1-4}$  become weaker for grazing angle incidence (especially for  $KL^8$ ). Such a feature was more clearly observed for  $Ne^{9+}$  incidence [18]. They proposed two characteristic times for an explanation, *i.e.*, a mean time ( $\tau_{n \rightarrow L}$ ) for filling of  $L$  shell from upper states and a lifetime ( $\tau_{L \rightarrow K}$ ) of the  $K$ -shell vacancy by electrons in  $L$  shell. In a case of  $\tau_{L \rightarrow K} \gg \tau_{n \rightarrow L}$ ,  $L$  shell is filled up at the moment of the  $K$ -shell vacancy is filled up, *i.e.*,  $K$  X-rays with more  $L$ -shell electrons are expected to be strong. In the normal incidence,  $L$  shell of HA2s is quickly filled via  $LMM$ -Auger transitions ( $M$  shell is always quasi-closed, because of the side-feeding), which makes the  $L$ -shell population larger at the moment of  $KL$  transitions. On the other hand, in a case of  $\tau_{n \rightarrow L} \gg \tau_{L \rightarrow K}$ , as soon as electrons from upper states are fed to the  $L$  shell, the  $K$  shell hole is filled up, *i.e.*,  $K$  X-rays with less  $L$ -shell electrons are expected to be strong. In the grazing angle incidence, the  $L$  shell of HA1s is slowly and one-by-one filled up due to facts that large number of cascades are necessary and that one electron is emitted in a transition, which makes the  $L$ -shell population smaller at the time of the  $KL$  transitions.

It is noted that fluorescence yield of the helium-like Ar ( $1sn\ell$ ) is unity (no auto-ionization), and the mean fluorescence yield of Ar ions with a  $K$  shell vacancy in solid is 0.04, *i.e.*, fluorescence yield in the solid is about 20 times smaller than the helium-like Ar. As is seen in Fig. 1.4(B), the observed line intensity for the helium-like Ar is very weak in spite of the larger fluorescence yield. Briand et al. concluded that the  $K$ -shell filling events above the surface are much less than 1 % taking into account of the fluorescence yields and the line intensities. This indicates that X-ray measurements probe HA2s rather than HA1s.

## Auger Electron Measurement

Auger electron emission processes, which are competitive with the X-ray emission processes, have been studied by several groups. They have mainly focused on the  $K$ -shell filling events by observing energetic  $KLL$ -Auger electrons.

Meyer et al. measured  $K$ -Auger electrons at the angle perpendicular to the beam direction when 4.3 keV/amu  $N^{6+}$  ions bombarded a clean gold surface at grazing angles between  $0.5^\circ$  ( $v_\perp = 7.9 \times 10^3$  m/s) and  $19.5^\circ$  ( $v_\perp = 3.0 \times 10^5$  m/s). Figure 1.5(a) shows the resultant  $K$ -Auger electron spectra [19], in which a continuum background has been subtracted. The peak heights are normalized to each other by multiplying factors shown in the figure. Meyer et al. found that (1) the total intensity decreases with the increasing grazing angle, and that (2) while the shape of the spectrum looks unchanged for the grazing angle larger than  $4.5^\circ$ , a bump (highlighted in black in the figure) is recognizable on the lower energy side of the peak when the grazing angle is less than  $1.5^\circ$  and increases as the grazing angle gets smaller.

Meyer et al. performed Monte Carlo simulations of the projectile trajectories inside the solid to reproduce the intensity variation with the incident angle. The projectiles with a  $K$  vacancy capture electrons dominantly into their  $M$  shell below the surface, and the subsequent Auger cascades fill the  $L$ - and  $K$ -shell holes. After  $K$ -Auger transitions at the depth  $z$  below the surface, total number of the  $K$ -Auger electrons escaping from the surface without any inelastic scattering was simulated accounting for an escape probability,  $\exp(-z/\lambda \cos \theta)$ , where  $\lambda$  is the inelastic mean free path of the electrons having the corresponding energies. Meyer et al. concluded that most of the  $K$ -Auger electrons are emitted below the surface (subsurface component) comparing total  $K$ -Auger yields with results of the simulations.

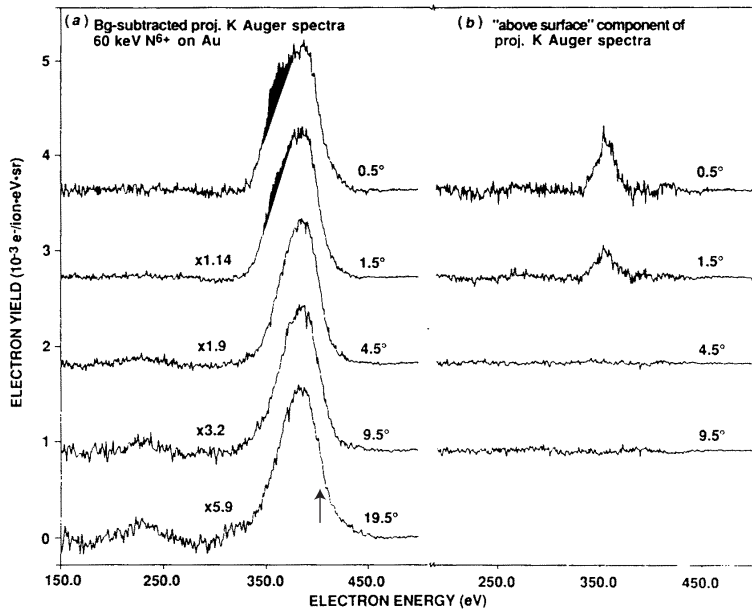


Figure 1.5: (a):  $K$ -Auger electron spectra observed for various grazing angles of incidence of 4.3 keV/amu  $N^{6+}$  ions on a gold surface. (b): Above-surface component [19].

The small bumps highlighted in black in Fig. 1.5(a) were attributed to  $KLL$ -Auger electrons with a few (two or three)  $L$ -shell electrons. Figure 1.5(b) shows the intensities of the bumps which were evaluated assuming that the subsurface component does not change its peak shape and only changes its intensity as a function of the grazing angle. Meyer et al. calculated cascades of transitions above the surface, assuming that electrons are always supplied into  $n = 7$  shell. The calculated intensity agrees with the observed one. It was concluded that the bump is formed as a result of  $KLL$ -Auger transitions above the surface (above-surface component).

Following the above experiment, Das and Morgenstern [20] investigated on the origin of the  $KLL$  peak in more detail. They measured  $KLL$ -Auger electrons as a function of the detection angle ( $\Theta$ ) when 2.0 keV  $N^{6+}$  ions were incident on a nickel surface with grazing angles ( $\Psi$ ) of  $5^\circ$  ( $v_\perp = 1.4 \times 10^4$  m/s) and  $15^\circ$  ( $v_\perp = 4.3 \times 10^4$  m/s). Figure 1.6(a) shows the centroid energy of the above-surface component as a function of the detection angle, and Fig. 1.6(b) shows the energy at the half maximum of the high energy side in the subsurface component (this electron energy corresponds to that pointed by the arrow  $\sim 400$  eV in Fig. 1.5). These energies in Figs. 1.6(a) and (b) are shifted due to the Doppler effect. Solid curves in Figs. 1.6(a)

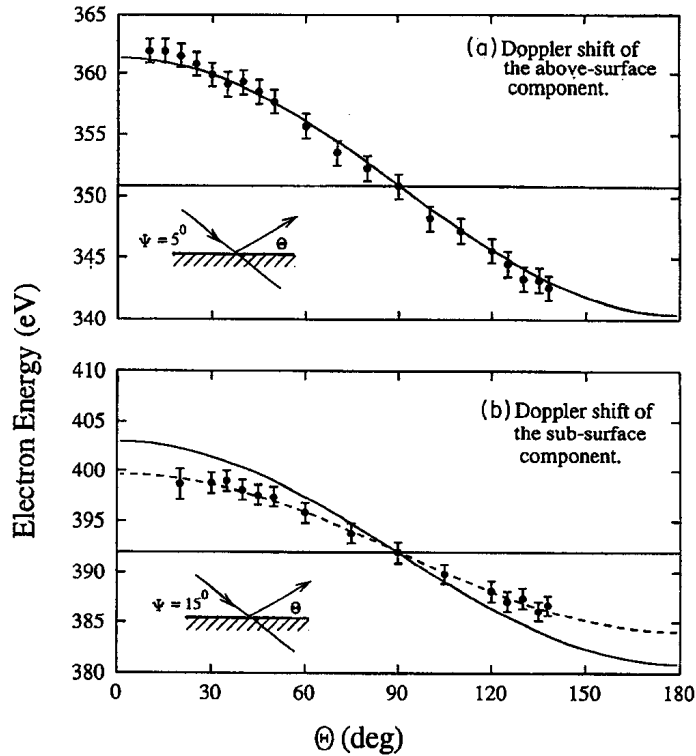


Figure 1.6: Energy position of the center of the above-surface component and that of half maximum at the high energy side of the subsurface component as a function of the detection angle [20].

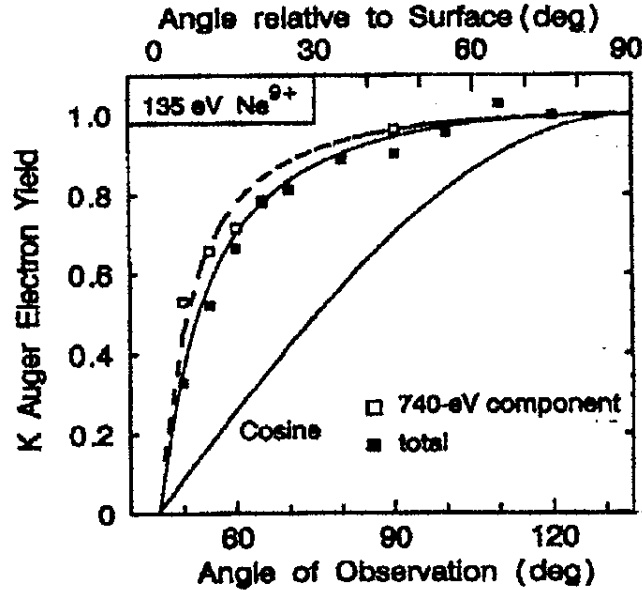


Figure 1.7: Intensity of the above-surface component ( $\square$ ) and total Auger electrons ( $\blacksquare$ ) at various detection angles [22].

and (b) show the Doppler shifts calculated assuming that the incident ion impinges with a straight trajectory to the surface keeping its initial kinetic energy (2.0 keV). Agreement between the observation and the calculation is better for the above-surface component than the subsurface component. From the Doppler shift for the subsurface component, they estimated the kinetic energy of the ions to be 1.5 keV at the moment of the Auger transitions, which is shown by the dotted curves in Fig. 1.6(b). They attributed this kinetic energy reduction to the energy loss by target atoms.

At almost the same time as the Doppler shift experiment, Köhrbrück et al. [21] also performed similar experiments using 90 keV  $\text{Ne}^{9+}$  ions impinging at a grazing angle of  $10^\circ$  ( $v_{\perp} = 1.6 \times 10^5$  m/s) onto a Pt(100) target. Here again, the observed electron energies show the Doppler shifts depending on the observation angles of  $\Theta = 20, 40, 60, 100$  and  $140^\circ$ . They attributed the Doppler shifts to the deflection of the ions inside the solid. Using a constant deflection angle of  $10^\circ$ , they reproduced the shifts measured at all of the detection angles (due to deflection, the ion results in moving parallel to the surface). Köhrbrück et al. pointed out that Auger electrons emitted below the surface lose their energies by inelastic collisions with the target, *i.e.*, it can be considered that the low energy side of the *KLL* peak results from Auger electrons emitted below the surface.

Grether et al. [22] also measured the intensity of *KLL*-Auger electrons when 0.135 keV  $\text{Ne}^{9+}$  ions were incident on an aluminum (111) surface with a fixed incident angle of  $45^\circ$  ( $v_{\perp} = 2.54 \times 10^4$  m/s). Figure 1.7 compares the intensities of the above-surface component (open squares) with those of the total *KLL*-Auger electrons (closed squares)

as a function of the detection angle. If the Auger electrons are emitted above the surface, their angular distribution is expected to be isotropic because the surface hardly influences trajectories of the electrons. On the other hand, if the Auger electrons are emitted below the surface, their angular distribution is expected to be anisotropic because some of them are scattered on their way to the surface. The observed angular distributions, however, show that both components have similar angular distributions, which indicates that the so-called above-surface component is not a convincing evidence for the above-surface emission.

Now it is commonly recognized that most of the *KLL*-Auger electrons are emitted below the surface, however it is still an open question whether the above-surface component results really from the emission above the surface or not.

As was reviewed, although the HA above surface was pursued intensively in X-ray and Auger electron measurements, these measurements are more useful to study the HA below the surface than above the surface.

### 1.3.3 Classical Over Barrier Model

After some of the experiments reviewed above, Burgdörfer et al. proposed a theoretical model [23] of neutralization above the surface. The model is an extension of what was developed by Ryufuku et al. [24] for atom-HCI collisions and later extended by Bárány et al. [25] and Niehaus [26] for multiple electron transfers. The model is called *Classical Over Barrier model* (COB model).

Let us consider a slow HCI with charge  $Q_{in}$ , an active electron and a surface with work-function  $W$ . Rectangular coordinates are adopted with  $x$  and  $y$  axes on the surface plane and  $z$  axis normal to the surface. Here the slow HCI means that its velocity is much smaller than the Fermi velocity ( $v_F$ ) of the solid, *i.e.*, valence electrons screen the HCI charge completely, and electron transfer can be treated as adiabatic.

When the HCI is located at  $(0, 0, R)$  and the electron at  $(x, y, z)$ , the electron is subject to the total potential

$$\begin{aligned} V(x, y, z, R) &= -\frac{Q_{in}}{\sqrt{(R-z)^2 + r^2}} + \frac{Q_{in}}{\sqrt{(R+z)^2 + r^2}} - \frac{1}{4z}, \\ r^2 &= x^2 + y^2, \end{aligned} \quad (1.5)$$

where the first, second and third terms in the right-hand side of Eq. 1.5 represent the interaction potential between the electron and the HCI, the electron and the image charge of the HCI, and the electron and the image charge of the electron itself. The total potential when an HCI with  $Q_{in} = 10$  is located at  $R = 20$  a.u., is shown in Fig. 1.8, in which a saddle point (potential barrier) is seen very close to the surface.

Equation 1.5 predicts that the distance of the saddle point,  $z_s$ , from the surface is given by

$$z_s \approx \frac{R}{\sqrt{8Q_{in} + 2}}; \text{ for } Q_{in} \gg 1. \quad (1.6)$$

and the potential at the saddle point is

$$V_s = V(0, 0, z_s, R) \approx -\frac{\sqrt{8Q_{in} + 2}}{2R}. \quad (1.7)$$

In the COB model, electron transfer starts when the potential at the saddle point becomes lower than the Fermi level of the surface, which is satisfied at a critical distance,  $d_c(Q_{in})$ ,

$$d_c(Q_{in}) \approx \frac{\sqrt{8Q_{in} + 2}}{2W} \approx \frac{\sqrt{2Q_{in}}}{W}. \quad (1.8)$$

The energy levels of the HCI located at  $R$  are shifted upward compared with those in a free space, because of the image charges of the HCI and the transferred electron itself. Assuming that the energy level of HCI is hydrogen-like and that the image potential is represented by that evaluated at the position of the HCI, the energy level is given by

$$E_n(R) = -\frac{Q_{in}^2}{2n^2} + \frac{Q_{in}}{2R} - \frac{1}{4R}, \quad (1.9)$$

where  $n$  represents the principal quantum number of the transferred electron. Because  $E_n(d_c(Q_{in})) = -W$  is satisfied in the over-barrier condition, one may obtain a critical

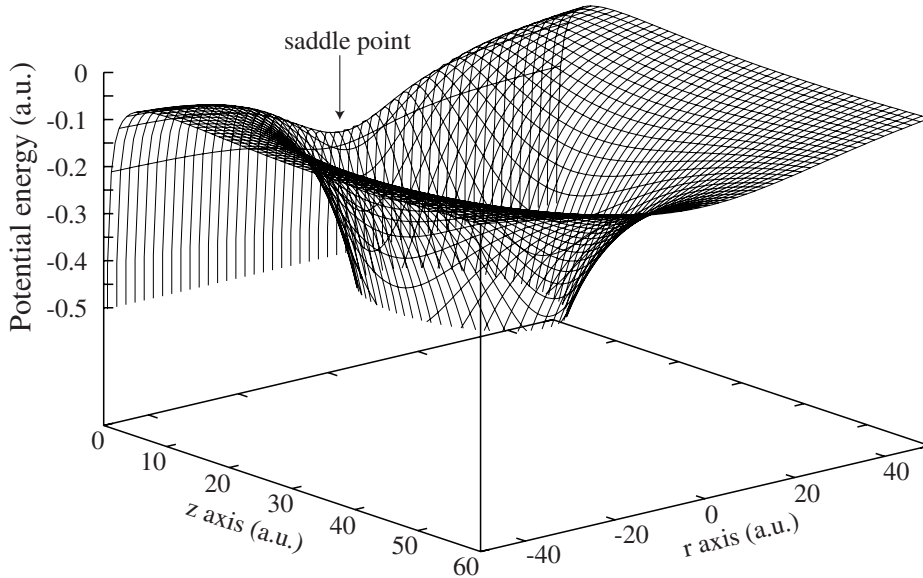


Figure 1.8: Total potential experienced by an active electron when an HCI with  $Q_{in} = 10$  is located at  $R = 20$ .

principal quantum number  $n_c(Q_{in})$ ,

$$n_c(Q_{in}) \approx \frac{Q_{in}}{\sqrt{2W}} \left( \frac{1}{1 + \frac{Q_{in}-0.5}{\sqrt{8Q_{in}}}} \right)^{\frac{1}{2}}. \quad (1.10)$$

Substituting, for example,  $Q_{in} = 10$  and  $W = 0.2$  a.u.,  $n_c(Q_{in})$  is estimated to be 11 and  $d_c(Q_{in})$  to be 23 a.u.. Eq. 1.10 is well approximated by

$$n_c(Q_{in}) \approx Q_{in} + 1, \quad (1.11)$$

around  $Q_{in} \approx 10$  and  $W \approx 0.2$  a.u.. Unlike Eq 1.4, Eqs 1.8 and 1.10 show that the electron transfer takes place to the lower  $n$  state of the HCI at the closer distance to the surface.

The angular momentum quantum number,  $\ell$ , of the transferred electron is expected to be small because the electron should pass through the narrow groove of the potential barrier [23]. It is also proposed [27] that  $\ell$  is determined by kinematically, *i.e.*, of the order of  $m_e v_H d_c(Q_{in})$ , where  $m_e$  is the electron mass and  $v_H$  is the velocity component of the HCI parallel to the surface.

If it is assumed that core charge is screened completely by the first transferred electron, *i.e.*, the core charge is  $Q_{in} - 1$ , the next COB resonance may take place to the lower energy levels with  $n_c(Q_{in} - 1)$  when the HCI approaches the surface to  $d_c(Q_{in} - 1)$ , which leads to formation of an HA1. In this case, the first electron can be returned back to an empty levels of the target (resonant ionization), or emitted in vacuum, if possible, because the second electron causes a screening shift and closer distance between the surface and the HCI pushes energy levels of the first electron upward (image shift). Through these processes, the size of the HA1 shrinks as it approaches the surface.

The HA1 finally gets below the surface, where two types of electron transfer processes are considered. When the HA1 approaches very close to one of the target atoms, quasi-resonant neutralization of deeply bound target electrons can take place. Further electrons in the valence band screen the HCI with a screening length of  $\lambda_D$ ,

$$\lambda_D = \frac{v_F}{\omega_p}, \quad (1.12)$$

where  $\omega_p$  is plasma frequency of the surface or bulk mode. Hence  $n_s$  shell with nearly the same radius as the screening length is rapidly populated,

$$\langle r \rangle \approx \frac{n_s^2}{Q} \approx \lambda_D, \quad (1.13)$$

where  $Q$  is the charge within  $\langle r \rangle$ . If an HCI has any empty shells with  $n \leq n_s$ , hollow atoms below the surface (HA2) are formed. As soon as the HA2 is formed, electrons bound in higher excited states than  $n_s$  are released (so-called peer-off).

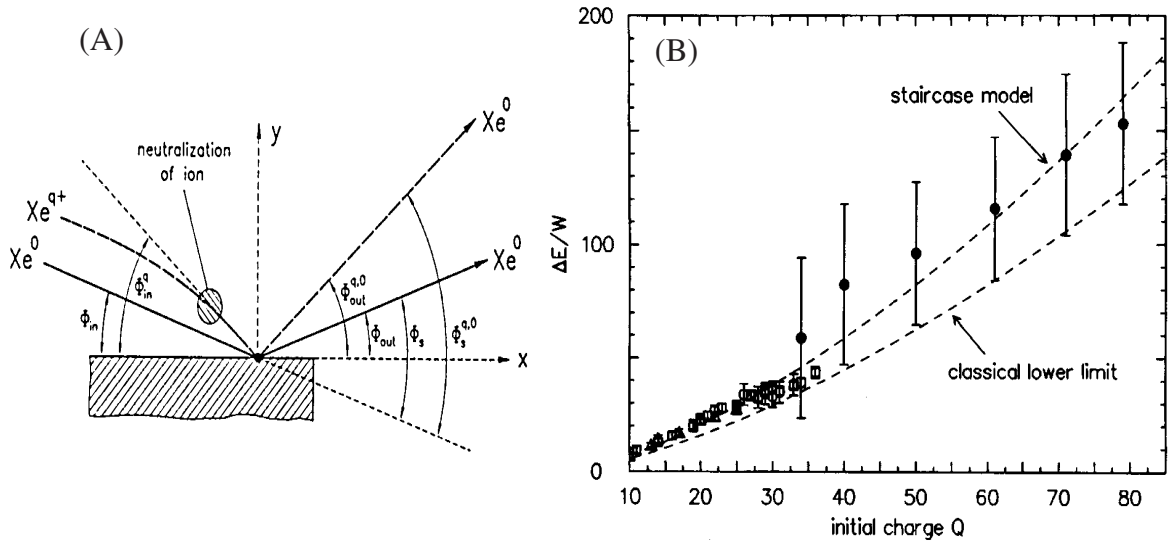


Figure 1.9: (A): Schematic [28] drawing of a reflection angle measurement, and (B): energy gain as a function of the incident charge deduced from reflection angle measurements ( $Q \leq 36$ ) [28, 29, 30, 31] and from secondary electron measurements (closed circle) [32].

### 1.3.4 Above Surface Neutralization

#### Reflection Angle Measurement

H. Winter et al. bombarded an aluminum (111) flat surface with argon ions ( $1 \leq Q \leq 6$ ) and xenon ions ( $1 \leq Q \leq 33$ ) at grazing angle of  $\sim 1.5^\circ$ , and measured a reflected angle ( $\Phi_{out}^{Q \rightarrow 0}$ ) of the neutralized atoms [28, 29]. As is shown in Fig. 1.9(A), the incident ion is accelerated toward the surface by its image charge prior to the electron transfer. Within a certain distance from the surface, the ion successively captures electrons. The image acceleration continues until the ion is completely neutralized. As a result, the incident angle  $\Phi_{in}^Q$  at the surface becomes larger than the initial incident angle  $\Phi_{in}$ . When the ions touch the surface, most of the ions are neutralized [30], and reflect specularly. Such atoms fly away from the surface without any deflection, *i.e.*,

$$\Phi_{in}^Q = \Phi_{out}^{Q \rightarrow 0}. \quad (1.14)$$

Therefore  $\Phi_{out}^{Q \rightarrow 0}$  reflects the charge variation of the incident ions above the surface. In other words,  $\Phi_{out}^{Q \rightarrow 0}$  reflects an energy gain  $V_{im}$  of the incident ion above the surface due to its image acceleration, which is given by

$$V_{im} = E \left( \sin^2 \Phi_{in}^Q - \sin^2 \Phi_{in} \right), \quad (1.15)$$

where  $E$  is the kinetic energy of the incident ion. Figure 1.9(B) plots  $V_{im}/W$  as a function of incident charge ( $1 \leq Q \leq 36$  [28, 29, 30, 31]).

## Secondary Electron Measurement

Kurz et al. paid their attentions not to energetic Auger electrons, but to slow secondary electrons with energies below 50 eV, and measured total secondary electron yields  $\gamma_Q$  with charge states as high as  $\text{Th}^{80+}$  [32, 33, 34]. The HCIs were incident on a polycrystalline gold surface with normal impact velocities ( $v_p$ ) below  $5 \times 10^5$  m/s <sup>§</sup>. Figure 1.10 shows the result for  $\text{Th}^{71+}$  in which  $\gamma$  decreases with increasing  $v_p$  (the abscissas is  $1/v_p$ ).

They explained the result by dividing  $\gamma$  into two parts,

$$\gamma(v_p) = c_1 v_p^{-\alpha} + \gamma_\infty \quad (0 \leq \alpha \leq 1). \quad (1.16)$$

The velocity-dependent first term results from an expectation that the number of electrons emitted via AI process should be proportional to the survival time of the HAI above the surface. The velocity-independent second term in Eq. 1.16 results from an expectation that electrons in highly excited states are emitted due to the image shift or screening shift above the surface, and are peered off due to side-feeding below the surface. The first term was fitted to the electron yields measured at smaller  $1/v_p \leq 0.4 \times 10^{-4}$  s/m, which is shown by the dotted curve in Fig. 1.10. The resultant  $\alpha$  was around 0.5.

When  $1/v_p$  becomes larger than  $0.4 \times 10^{-4}$  s/m (*i.e.*,  $v_p$  becomes smaller), the electron yield deviates from the dotted curve, and approaches a constant value. This shows that the survival time for the HCI above the surface has an upper limit due to the image acceleration. An intersection of the saturated yield with an extrapolation of the velocity-dependent yield gives the lowest achievable impact velocity, *i.e.*, energy gain. Energy gain deduced from this method is plotted with closed circles in Fig. 1.9(B) (data points with larger error bars).

## Interpretation

The energy gain can be calculated in the framework of the COB model as

$$V_{im} = \int_{\infty}^0 \frac{(Q(R))^2}{4R^2} dR, \quad (1.17)$$

where  $Q(R)$  is the charge state of the HCI at a distance,  $R$ , from the surface [35, 36].  $Q(R)$  is a function of not only the distance between the ion and the surface, but also the velocity of the ion toward the surface. Two extreme assumptions are considered, *i.e.*, one-step model and staircase model.

---

<sup>§</sup> Secondary electron emission can be classified into two categories. One is potential emission, in which electrons are emitted via AI or AN processes. The other is kinetic emission (KE), in which electrons are liberated through a direct momentum transfer by incident ions. However electrons emitted by the KE process make a negligible contribution to the total yield in this velocity range.

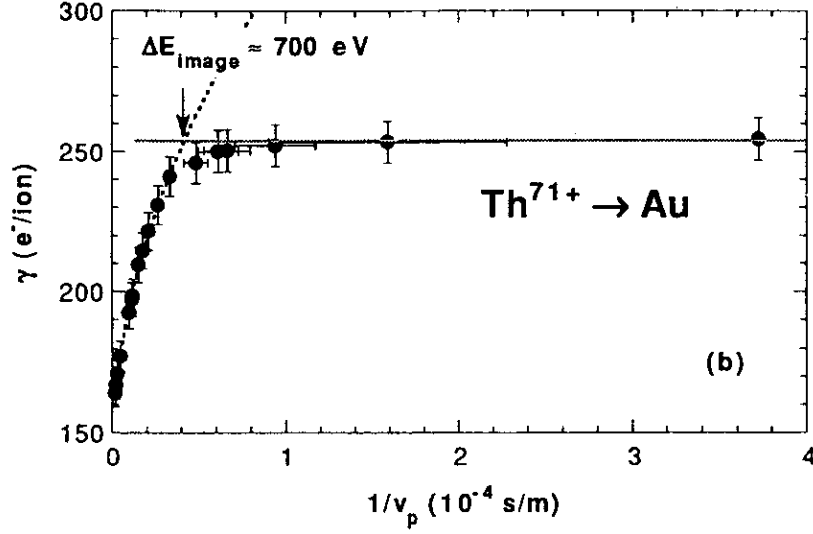


Figure 1.10: Total secondary yield,  $\gamma$ , vs inverse normal projectile velocity,  $v_p$ , for impact of  $\text{Th}^{71+}$  on a polycrystalline gold surface [32].

In the one-step model, the incident ion is assumed to be neutralized completely as soon as the ion arrives at the critical distance  $d_c(Q)$ , and the subsequent electron loss processes via auto-ionization or resonant transfer to a vacant state of the solid are ignored. Hence the resultant energy gain is given by

$$V_{im} = \int_{\infty}^{d_c(Q)} \frac{Q^2}{4R^2} dR = \frac{Q^2}{4d_c(Q)} = \frac{W}{4\sqrt{2}} Q^{\frac{3}{2}}. \quad (1.18)$$

This quantity gives an upper limit of the existing time,  $\Delta t$ , for HAIs to be above the surface and to emit decay signals above the surface, which is given by

$$\Delta t = d_c(Q) \sqrt{\frac{M}{2V_{im}}} = \sqrt{\frac{4\sqrt{2}QM}{W^3}}, \quad (1.19)$$

where  $M$  is the mass of the incident ion. For example,  $\text{Ar}^{10+}$  ion is incident on the surface with  $W = 0.2$  a.u.,  $V_{in}$  and  $\Delta t$  are estimated to be 30 eV and  $\sim 1.0 \times 10^{-13}$  sec, respectively.

In the staircase model, electrons are assumed to be transferred step-by-step and one-by-one to the incident ions where screening by the previously transferred electrons is regarded to be complete, *i.e.*, the second and third and .... electron transfers occur at  $d_c(Q-1)$  and  $d_c(Q-2)$  and .... to the corresponding atomic states, respectively. Hence the energy gain is given by

$$V_{im} = \sum_{i=0}^{Q-1} \frac{(Q-i)^2 - (Q-i-1)^2}{4d_c(Q-i)} = \frac{W}{4} \sum_{i=0}^{Q-1} \frac{2(Q-i)-1}{\sqrt{2(Q-i)}} \approx \frac{W}{3\sqrt{2}} Q^{\frac{3}{2}}. \quad (1.20)$$

It is noted here that the AI process above the surface are neglected in the above two expressions for  $V_{im}$ . Equations 1.18 and 1.20 are plotted with dashed lines in Fig. 1.9(B), where one-step model is referred to as the classical lower limit. The energy gain predicted by the staircase model agrees well with the observed ones.

## 1.4 Insulator and Capillary Surface

As was shown above, the formation of the HA1 above the surface is confirmed by the energy gain measurements, however few is known about detailed information of the HA1. Although spectroscopic measurements, *i.e.*, X-ray and Auger electron measurements are expected to give the detailed information of the HA1, there are unavoidable difficulties to study the HA1 with the flat metallic surfaces, *i.e.*,

- The survival time of the HA1 is limited to be less than  $10^{-13}$  sec by the image acceleration, therefore only transitions from states with shorter lifetimes than the survival time can be observed. However as far as measuring  $K$  X rays or  $KLL$ -Auger electrons, it takes a long time to populate  $L$  shell by electron cascades from the upper shells of the HA1.
- Very weak signals emitted from the HA1 are superimposed by relatively intense signals from the HA2 in almost the same energy region.

To observe HA1 above the surface, experiments with an flat insulator surface or with a metallic capillary surface (an insulator capillary is also available) attract growing interests, in which the difficulties with the flat metallic surface are removed to some degree.

### 1.4.1 Insulator Surface

In the neutralization process, the surface is positively charged due to the successive electron transfer from the surface to the HCI. This charged area on the surface is neutralized with a time constant of  $\epsilon/\sigma \approx 10^{-15}$  sec when the metallic surface is used ( $\epsilon$  and  $\sigma$  are the dielectric constant and conductivity of the metal). When the insulator surface is used, the charged area remains for a longer time, which is expected to decelerate the HCI and to make the survival time of the HA1 longer. As a result, the longer time is available for the HA1 to de-excite to lower energy levels.

Limburg et al. measured  $KLL$ -Auger electrons when  $N^{6+}$  with  $v_{\perp} \approx 2.3 \times 10^4$  m/sec were incident on a LiF surface [37]. They found that the above-surface component

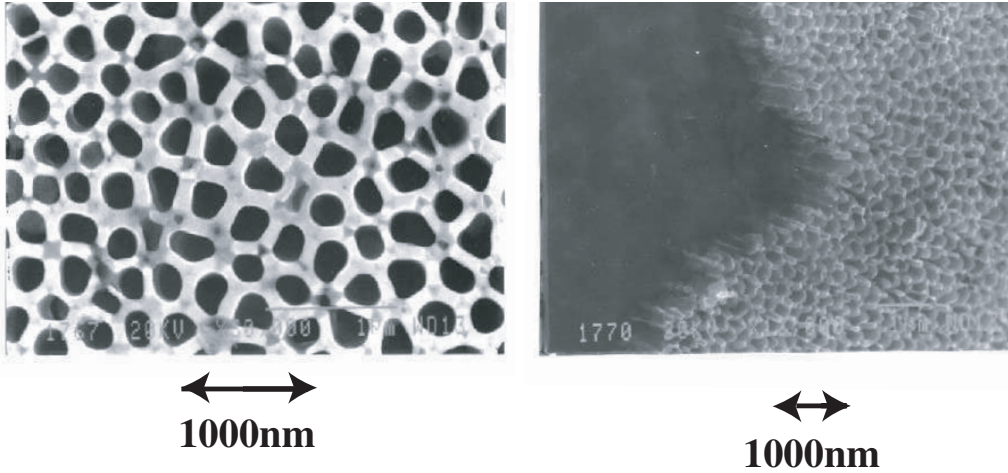


Figure 1.11: Photographs of an micro-capillary target by the scanning electron microscope. The left figure was taken in front of the surface, and the right one taken at a diagonal angle.

which was observed with a metal surface was not clearly observed and the subsurface component was dominant (see Fig. 1.5), although a longer survival time of the HA1 was expected (memorize that the smaller grazing angle in Fig. 1.5 corresponds to the longer survival time of the HA1). Limburg et al. concluded that the HA1 is not formed when the insulator surface is used, because the energy levels of valence electrons of the insulators are generally deeper than those of metallic surfaces, which reduces resonant electron transfer rates.

Briand et al. measured  $KL$  X-rays when  $v_{\perp} \approx 0.1 \times 10^4$  m/sec  $\text{Ar}^{17+}$  ions were incident on a  $\text{SiO}_2$  surface [38]. They reported that, in the contrary to the Auger electron measurement with LiF surface, above-surface component ( $KL^1$  in Fig. 1.4) was observed strongly, while subsurface components like  $KL^8$  is very weak. From the result, they proposed that the incident HCI is decelerated by positive charges induced by successive electron transfers, and finally reflected back before the HCIs touches the surface. Their proposal was, however, criticized because there were no direct evidence of such reflected ions [39].

## 1.4.2 Capillary Surface

To avoid the difficulties with a flat metal surface, our group has been making use of a micro-capillary foil [40, 41], a thin foil with many small straight holes perpendicular to the surface. Figures 1.11 shows images of a Ni micro-capillary foil taken with a scanning electron microscope (SEM). The thickness and hole diameter  $2r_{cap}$  are approximately  $1.5 \mu\text{m}$  and  $200 \text{ nm}$ , respectively. Figure 1.12 shows possible trajec-

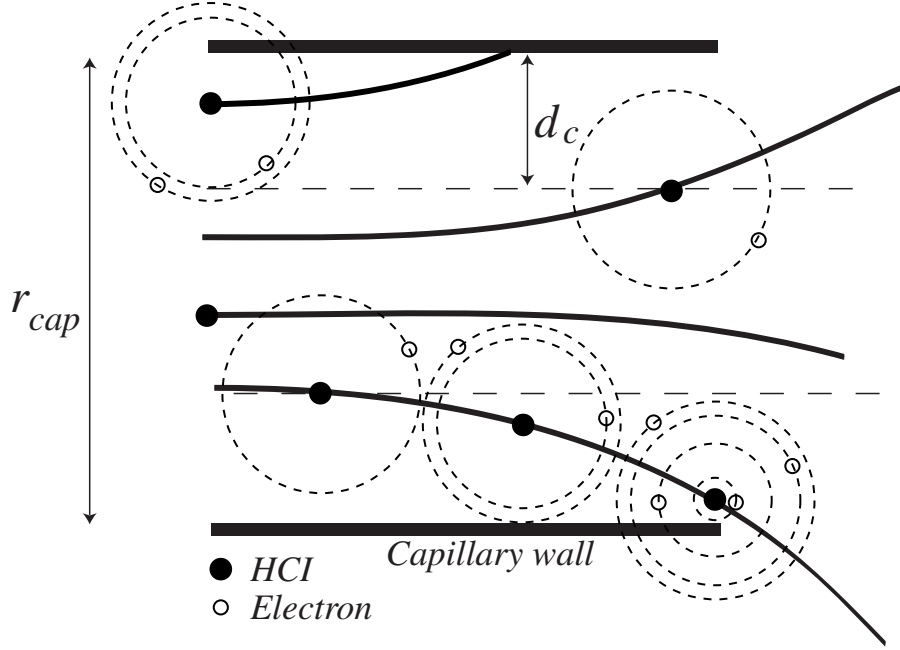


Figure 1.12: Possible process expected in capillary-HCI collision.

jectories of HCIs injected along the capillary axis. The trajectories of the HCIs can be classified into three according to the closest approach,  $r_{close}$ , to the capillary wall. For  $r_{close} > d_c \approx \sqrt{2Q}/W$ , HCIs pass through the capillary without capturing any electron. This fraction is the dominant for the capillary with some hundred nanometer diameter, and evaluated as  $\sim 1 - 2d_c/r_{cap}$ . In the case of the Ni capillary with  $W = 0.18$  a.u., this fraction is calculated to be  $\sim 97\%$  for  $Q_{in} = 10$  and  $r_{cap} = 1890$  a.u. (100 nm). For  $r_{close} = 0$ , HCIs collide with the capillary wall, which is similar to the situation in the grazing angle collision with a flat surface. Most of the HCIs are neutralized. For  $0 \leq r_{close} \leq d_c$ , HCIs pass through the capillary with some electrons captured. Electron capture may start to the higher excited states, and continue to lower states as the HCIs approach closer to the surface, *i.e.*, HA1s are formed. The number of the captured electrons depends upon the  $r_{close}$ . The transmitted HA1s de-excite through Auger and/or radiative transitions in vacuum, *i.e.*, because the HA1s formed do not crush into the surface, even transitions with lifetimes longer than the survival time can be observed. Further limiting the observed region to the downstream region of the capillary, only signals from HA1 can be selected.

The capillary foil was first applied by Ninomiya et al. to X-ray measurements [42, 43, 44, 45, 46]. They bombarded a micro-capillary foil made of  $\text{Al}_2\text{O}_3$  with hydrogen-like  $\text{Ne}^{9+}$  ions, and observed  $K$  X-rays downstream of the foil with a Si(Li) detector. Figure 1.13(A) [44] shows the Ne  $K$  X-rays spectra measured downstream of the foil (closed circles) as well as at the entrance of the foil (solid line). As is seen in the spectra, the downstream spectrum shifts by about 50 eV toward higher energy side

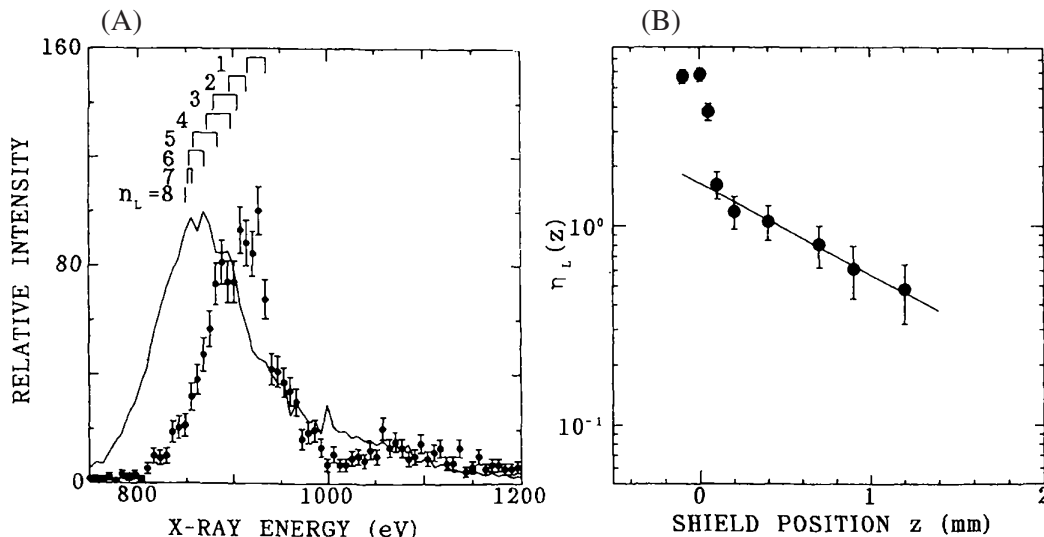


Figure 1.13: (A) Ne K X-rays emitted downstream of the capillary (closed circle) and those emitted from the entrance surface of the capillary (solid line). (B) Decay curve of the integrated K X-ray yield [44].

compared with the entrance spectrum. The shift was attributed to the number of electrons in the  $L$  shell at the moment of the transitions.  $K$  X-ray energies with different number of  $L$  electrons are shown with the bars in Fig. 1.13(A), *i.e.*, less  $L$  electrons in the downstream spectrum and more  $L$  electrons in the entrance spectrum. As was seen in Section 1.3.2,  $L$  shell of the HA2 is quickly filled by target electrons, which results in larger number of  $L$  electrons in the entrance spectrum. On the other hand, HA1 formed at the exit of the capillary de-excites mainly through Auger-cascades, which results in less  $L$  electrons in the downstream spectrum.

$K$  X-ray yields were measured shadowing the region between the exit of the capillary and a position  $z = vt$  downstream of the capillary ( $v$  is the ionic velocity). Figure 1.13(B) [44] shows the integrated  $K$  X-ray yield defined by

$$\eta(z) = \int_z^\infty \zeta(z') dz', \quad (1.21)$$

where  $\zeta(z')$  is the differential  $K$  X-ray yield at  $z'$  along the beam path. It is seen that the decay time is as slow as  $\sim 0.8$  ns, which is more than  $10^4$  and  $10^6$  times longer than typical radiative and Auger lifetimes of Ne atoms/ions with a filled  $L$  shell and a  $K$ -shell vacancy. Calculations by multi-configuration Dirac-Fock code revealed that such long lifetime components can be attributed to transitions of highly spin-aligned states with half-filled inner-shells and a less than half-filled outermost shell, such as  $\text{Ne}^{8+} 1s2p \ ^3P_1 - 1s^2 \ ^1S_0$  (0.16 ns and 915.2 eV) and  $\text{Ne}^{7+} 1s2s2p \ ^4P_j - 1s^2 2s \ ^2S_{1/2}$  with  $j = 1/2, 3/2$  (0.4 and 0.6 ns, and 895.0 eV). Such meta-stabilities were also observed for lower exit charge state ions [42]. For better understanding of the capillary spectra,

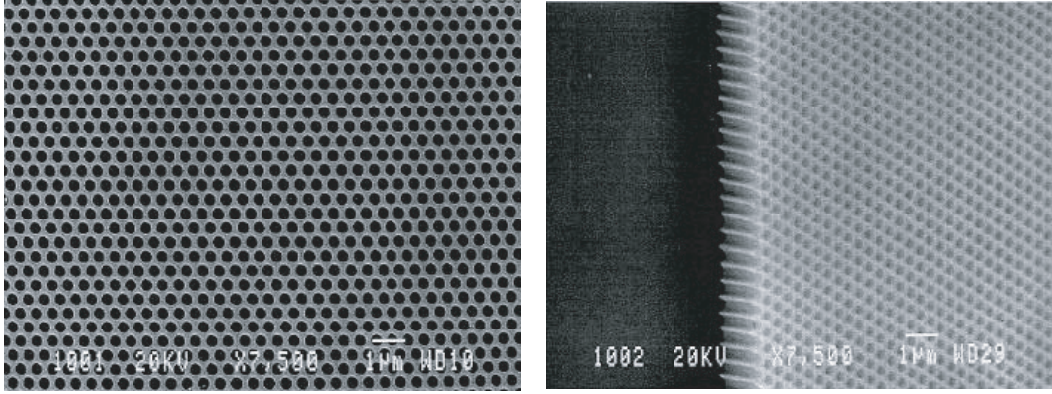


Figure 1.14: A target with comparatively uniform in diameter and regularly distributed capillaries.

not only lifetime measurements but also measurements with much higher energy resolution were desired. High-resolution experiments have been performed with a grating spectrometer [47]. The transitions from the states predicted above are successfully observed at the same energy positions [48, 49].

An angular distribution of HCIs passing through the capillary was measured to confirm the relation between the exiting angle and the exiting charge states [50, 51, 52]. As is drawn in Fig. 1.12, the exiting angle is expected to have a close relation with the exiting charge states. Angular distributions of the exiting ions/atoms after charge state selection were measured with three different types of capillary targets, a target with randomly distributed capillaries (Figure 1.11, referred hereafter to as random target) and that with comparatively uniform diameter and regularly distributed capillaries (Figure 1.14, uniform target) and a micro-channel plate (MCP). The results were as follows.

(1) Transmitted current ( $I_t$ ) was successfully reproduced by the product of the opening ratio ( $k$ ) of the capillary and the injected current ( $I_i$ ),

$$I_t \approx kI_i, \quad (1.22)$$

in the case of the uniform target and the MCP. However for the random target,  $I_t$  is about 25 times less than the expected current, which was attributed to non-uniformity of the capillary diameters.

(2) Figures 1.15(A) and (B) show charge-state distributions of exiting ions from the random and uniform targets, respectively. The theoretical predictions taking account of both the COB model and Auger cascade after transmission through the targets [53, 54, 55] are given by the dotted lines. The predictions reproduce well the observed charge state distributions.

(3) Observed angular distributions were found to be much narrower than those expected theoretically. Actually the experimentally-estimated energy gain for each final

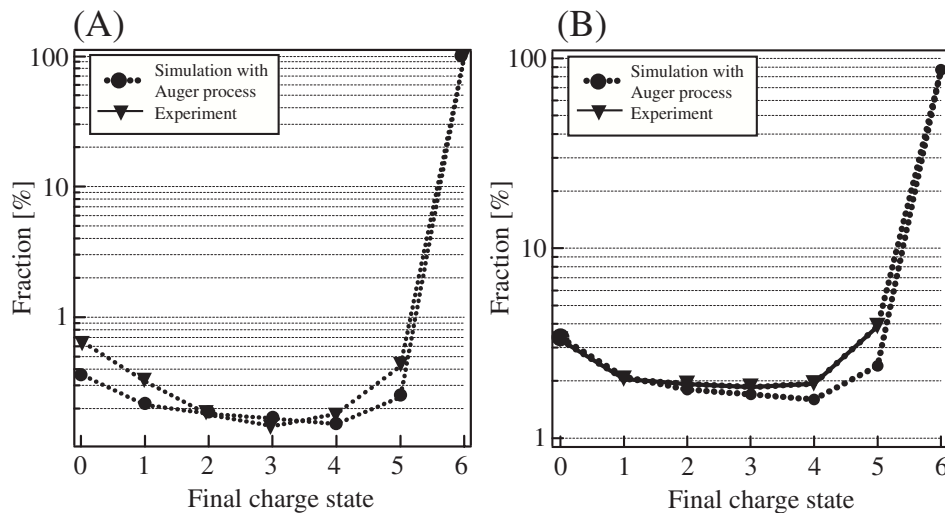


Figure 1.15: Charge state distributions under injection of  $800 \text{ eV/q Xe}^{6+}$  ions to the random target (A), and to the uniform target (B). Theoretical predictions based on the COB model are also shown.

charge was about 1 order of magnitude smaller than the theoretical prediction [50]. These observations were not satisfactorily explained till now.

Recently, Stolterfoht et al. also measured charge state distributions when  $3 \text{ keV Ne}^{7+}$  ions impinged onto an insulator capillary foil. The foil is made of polyethylene therephalate (Myler or PET) [56], the thickness and hole diameter of which were  $10 \mu\text{m}$  and  $100 \text{ nm}$ , respectively. They evaporated Au deposited on both sides of the capillary to avoid charge-up of the PET foil. They found that the HCIs can transmit through the capillary foil even when it was tilted with respect to the incident beam direction (the experimental configuration is shown in Fig. 1.16(A)). Broad peaks in Fig. 1.16(B) shows a fraction of  $\text{Ne}^{7+}$  ions, where the tilt angle is shown at the top of each distribution. Although the tilt angle is much larger than the aspect ratio of the capillary  $\sim 0.5^\circ$ , large fractions of  $\text{Ne}^{7+}$  ions transmit through the capillary in a direction corresponding to the tilt angle. They also measured the angular distributions with a capillary whose inner walls were covered with Ag to compare the difference between metallic and insulator surfaces. The resultant distribution shown in Fig. 1.16(B), was much narrower than the others, and only a small fraction of ions which never touched the surface transmitted through the capillary.

Figure 1.16(C) shows the time variation of the transmitted  $\text{Ne}^{7+}$  ions with the PET capillary. At the start in the “Beam on” region, transmitted  $\text{Ne}^{7+}$  ion current is increasing and become saturated with a time constant of  $\sim 10 \text{ min}$ . This indicates that inner-wall of the capillary is more or less charged and as a result, some electric field is formed in the capillary so that the incident ions are guided without hitting the

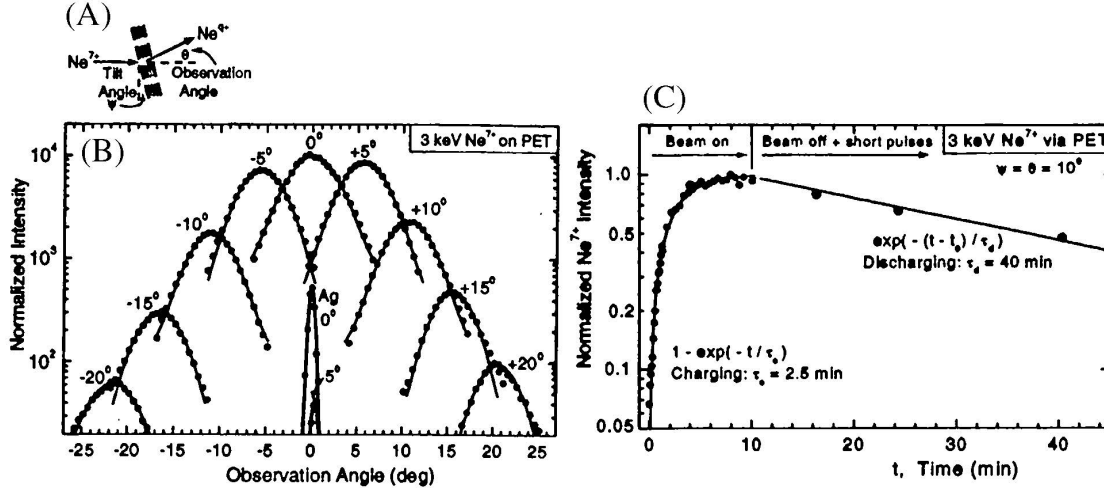


Figure 1.16: (A): Experimental configuration. (B): Angular distributions of transmitted  $\text{Ne}^{7+}$  ions for an insulator (broader peaks) and metallic (narrower peaks) capillaries. (C): Time variation of the transmitted  $\text{Ne}^{7+}$  ions. Stored charges on the capillary wall are saturated at  $\sim 10$  min. After the stop of the incident beam, the stored charges dissipate with a time constant of 40 min.

capillary wall.

## 1.5 Motivation for Visible Light Spectroscopy

As was reviewed above, the signals observed in most of the experiments were limited to  $K$  x-rays and  $KLL$  Auger electrons emitted from the HA2, those from the HA1 at the late stage of the neutralization above the surface, or energy gain (reflection angle and total secondary electron yield) in the whole neutralization process. Although these experimental results seem to be explained consistently with the COB model, there has been no experiment to test the COB model quantitatively (note that the COB model clearly predicts the first electron transfer). This may be partially because a very large number of electrons ( $\sim 3Q_{in}$ ) are involved in the whole process and, hence, detailed information on each electron transfer is difficult to extract.

As was expected, transmitted ions through a microcapillary foil are in various charge states depending upon the closest approach to the capillary wall. Among them, ions with one electron transferred (the COB model clearly predicts the first electron transfer) give a unique chance to study the very initial stage of the neutralization easier and clearer than the experiments reviewed above. Considering hydrogen-like energy levels,

$E_n$ , and de-excitation through  $\Delta n = n_u - n_l = 1$  radiative transition ( $n_u$  and  $n_l$  show principal quantum numbers of upper and lower states involved in the transition, respectively), the resultant photon will be emitted with an energy  $\Delta E$

$$\Delta E = E_{n_u} - E_{n_u-1} \approx \frac{Q_{in}^2}{n_u^3} \approx \frac{1}{Q_{in}}. \quad (1.23)$$

The third and fourth relations are obtained considering that  $n_u \gg 1$  and  $n_u \approx Q_{in}$  (see Eq. 1.11), respectively. Figure 1.17 shows the resultant transition wavelengths for various incident charges ( $8 \leq Q_{in} \leq 20$ ) as a function of  $n_u$ . The solid line shown in the figure connects points with critical principal quantum numbers ( $n_c$ ) predicted by the COB model (Eq. 1.11).  $\Delta n = 1$  transitions from such  $n_c$ 's result in emission of visible lights for wide range of the incident charges. As will be shown later, our detection system has sensitivity between 200 nm and 1000 nm, *i.e.*, we can study the initial process of the neutralization with visible light spectroscopy. It is noted here that a lifetime of such a high-lying Rydberg state is of the order of 1 ns which is  $\sim 10^4$  longer than the survival time of the HA above the surface, hence only the micro-capillary technique makes observations of visible light feasible.

It is easier to make an observed line resolution higher in the visible light spectroscopy than other techniques like in the X-ray or Auger spectroscopies. It is expected that such an advantage helps not only to understand the first electron transfer process clearly, but also to construct more precise theory for the electron transfer above the surface than the COB model. To understand the first electron transfer process may lead to understand the subsequent electron transfer, which gives a clue to predict the intrinsic nature of the HA1.

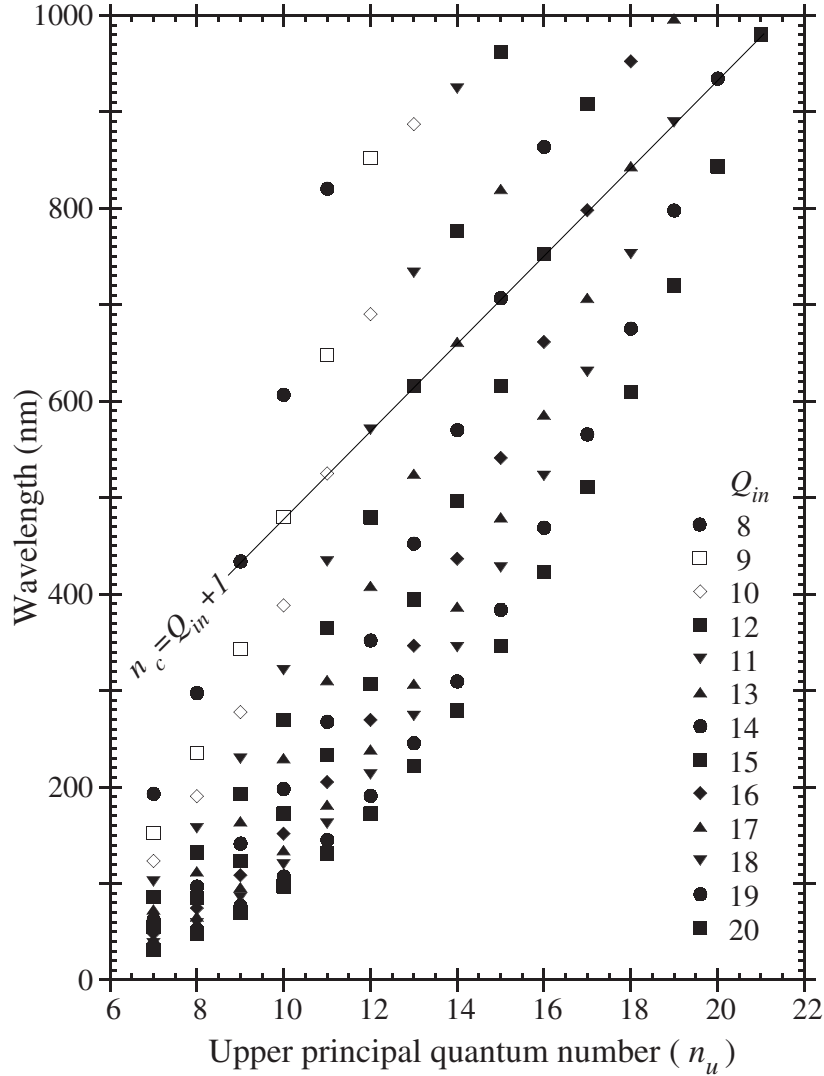


Figure 1.17: Wavelengths for  $\Delta n = 1$  transitions with their upper principal quantum numbers of  $n_u$  for various core charges ( $8 \leq Q_{in} \leq 20$ ). Initial states, which is expected from the COB model to populate most effectively ( $n_c \approx Q_{in} + 1$ ), are connected with the solid line. This shows that the micro-capillary method can serve not only as a tool for the study of electron transfer processes, but also as a visible light source of highly charged ions with various charge states.

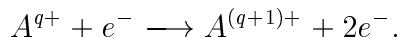
# Chapter 2

## Experiment

As was shown in Section 1.5, the initial process of the neutralization can be studied with the micro-capillary target by measuring visible lights when the incident charges of the incoming HCIs are around 10. This chapter first describes the experimental apparatus (ion source, beam line, focusing element, spectrometer and detector) necessary for the visible light measurement, and after that, explains how to calibrate observed wavelengths and to normalize line intensities.

### 2.1 Ion Source

Ion sources which can prepare slow highly charged ions (HCIs) were developed rather recently, *i.e.*, around 1990 [57, 58]. The most popular ion sources in atomic physics experiments are an *Electron Beam Ion Source* (EBIS) invented by Donets [58] and an *Electron Cyclotron Resonance Ion Source* (ECRIS) by Geller [57]. Figures 2.1(A) and (B) show schematic drawings of EBIS and ECRIS. In both cases, HCIs are produced by successive ionization with energetic electrons, *i.e.*,



In the case of the EBIS in Fig. 2.1(A), effective ionizations are realized with the high-density energetic electron beam, which is prepared by compressing the electron beam with the strong magnetic field. It is noted that the strong electric field formed by the electron beam radially attracts the resultant HCIs toward the electron beam, which extremely enhances the probability of further ionizations. The HCIs are trapped axially by an electric potential well formed by the drift tube. The HCIs so produced collide with residual gas atoms/molecules and reduce their charge states through electron capture, *i.e.*, the EBIS requires ultra high vacuum (UHV). It is reported [59], for example, that ten fully stripped  $U^{92+}$  ions and  $\sim 500$  hydrogen-like  $U^{91+}$  ions were produced with an electron beam of 198 keV and 205 mA (the diameter of the electron beam was compressed down to 70  $\mu\text{m}$  with 3 Tesla magnetic field and the current

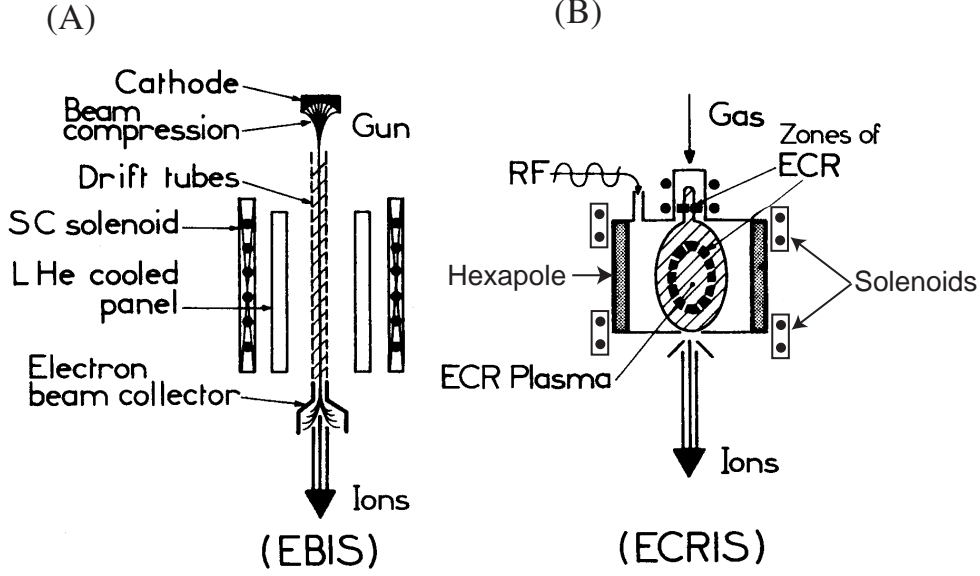


Figure 2.1: Schematic [57] of (A) an Electron Beam Ion Source (EBIS) and (B) an Electron Cyclotron Resonance Ion Source (ECRIS).

density achieved was  $5000 \text{ A/cm}^2$ ). Because well-collimated electron beam radially attracts HCIs with low energy, the emittance of the extracted beam is quite small. On the other hand, because of the UHV requirement and the radial trap of the HCIs by the electron beam, the extracted beam current is rather low.

Figure 2.1(B) shows the structure of an ECRIS, which is used not only for scientific but also for industrial purposes. An electron in a uniform magnetic field (strength  $B$ ) circulates around the magnetic field with the cyclotron frequency,  $\omega_c^B$ , given by

$$\omega_c^B = 2\pi f = \frac{eB}{m}. \quad (2.1)$$

For example in a magnetic field of 1 Tesla,  $\omega_c^B/2\pi$  is around 28 GHz. When a microwave with a frequency of  $\omega_{rf}(=\omega_c^B)$  is introduced with its electronic vector perpendicular to  $B$ , electrons are resonantly accelerated \*. Energetic electrons so prepared ionize atoms/ions successively. By combining the solenoids and the hexapole magnet as shown in Fig. 2.1(B), a so-called minimum B structure is formed in the ECRIS, *i.e.*, the strength of the magnetic field from the center of the plasma chamber becomes stronger for all directions (for axial directions by the solenoids and for radial directions by the hexapole magnet). Therefore there exists a closed surface (so called ECR zone) which satisfies  $\omega_c^B = \omega_{rf}$ .

When the spatial variation of the magnetic field,  $\delta B$ , along one cyclotron motion is so small ( $\delta\omega_c^B \ll \omega_c^B$ ) that the electron motion is regarded as adiabatic, the magnetic moment of the electron  $\mu_m = mv_\perp^2/2B$  conserves, where  $v_\perp$  is the electron velocity

\* It is known that electrons are accelerated up to 700 keV [60] by this scheme.

perpendicular to the magnetic field. The total energy  $E = \mu_m B + mv_{\parallel}^2/2$  of the electron also conserves ( $v_{\parallel}$  is the parallel velocity). Because of the minimum B structure for all directions in the plasma chamber,  $v_{\parallel}$  becomes smaller when the electron moves toward stronger B field, *i.e.*, the electron is trapped in an area around the center of the plasma chamber which satisfies  $B \leq E/\mu_m$  (mirror effect). When a large number of electrons are confined in a region in this way, a negative potential well is formed (several volt [61]), which attracts ions toward the electron cloud and enhances the probability of further ionizations. As is similar to the electron confinement, the ions are also confined by the mirror effect.

A buffer gas with a mass smaller than the ions to be used is often introduced in the ion source under operation for both ECRIS and EBIS. It is considered that the heavier ions are effectively cooled down by collisions with the smaller mass ions, which results in longer confinement time of the heavier ions in the plasma [62]. For example, we use helium gas for extraction of neon ions and oxygen or nitrogen gas for extraction of argon ions in the following experiments. As is shown in Fig. 2.2, charge states of the extracted HCIs from ECRIS is generally lower than those from EBIS, because ECRIS is operated under  $\sim 10^{-7}$  Torr vacuum to maintain the plasma. On the other hand, ECRIS can supply several orders of magnitudes stronger beams than EBIS can.

As was shown in Fig. 1.17, wavelengths for  $\Delta n = 1$  transitions from Rydberg ions are expected to be in the visible light range when the incident charges are less than 20, and ECRIS can supply more ion currents in this charge state range than EBIS can. Hence ECRIS was selected as the ion source for the present study.

Two types of ECRISs were used, *i.e.*, Hyper ECRIS [60] installed<sup>†</sup> at the Center for Nuclear Study (CNS), University of Tokyo and Caprice ECRIS [64, 65] installed at the Institute of Physical and Chemical Research (RIKEN). The former was used for the feasibility study and the latter for the improved study (see Section 2.3). Figure 2.3

<sup>†</sup> Now the Hyper ECRIS is used as an injector for an accelerator in RIKEN.

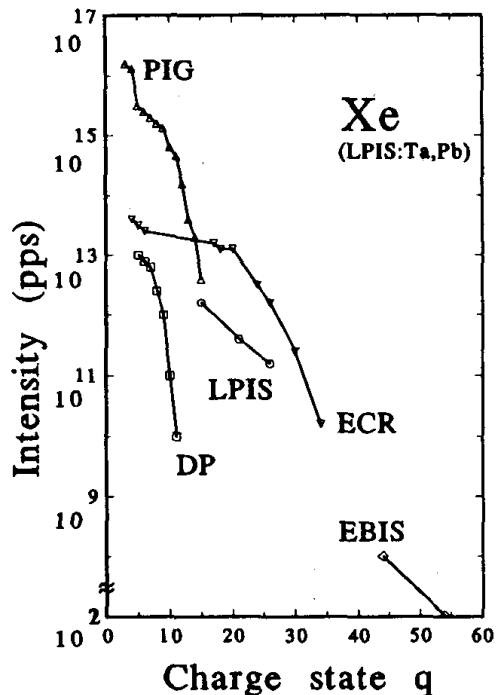
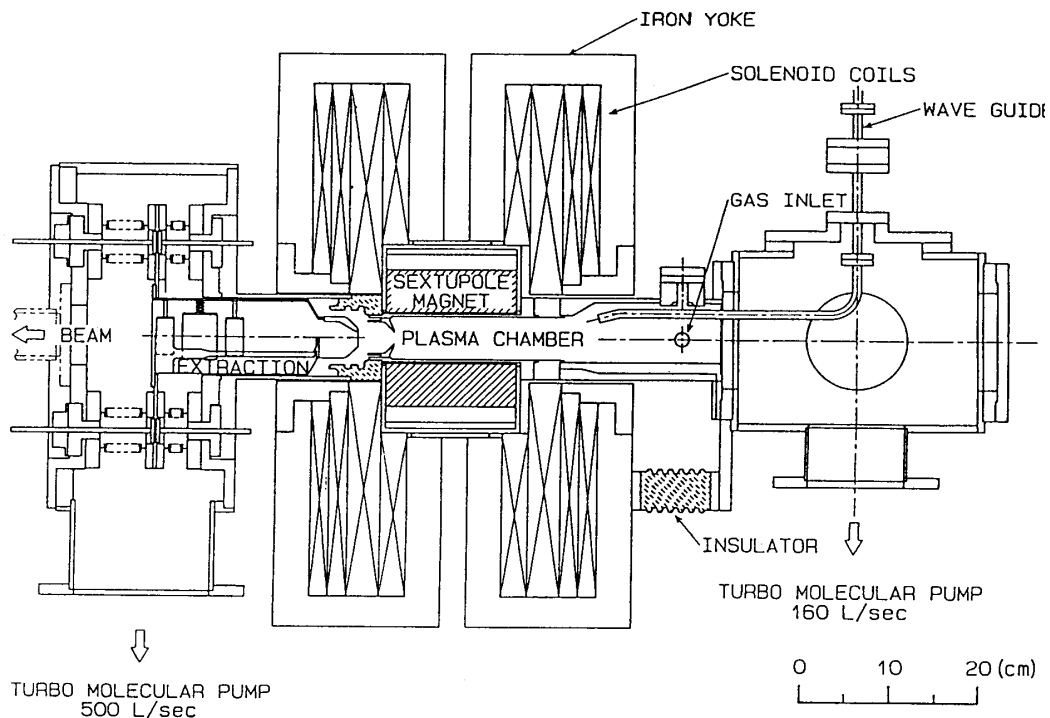


Figure 2.2: Ion intensities vs charge states of Xe extracted from ECRIS and EBIS [63].

shows a cross section of the Hyper ECRIS (the Caprice ECRIS has a similar structure as the Hyper ECRIS). Table 2.1 gives the parameters of both ECRISs. The HCIs in the plasma chamber are extracted through the electrodes located at left side of the plasma chamber in Fig. 2.3. The plasma chamber was biased from several kV to 20 kV and a micro-capillary target described below were at the ground potential, hence kinetic energies of the extracted ions are determined by the potential of the plasma

*Table 2.1: Parameters of Hyper ECRIS and Caprice ECRIS.*

	Hyper ECR	Caprice ECR
Microwave		
Frequency	14.25 GHz	14.5 GHz
Power	2.0 kW	1.3 kW
Multi-pole magnet		
Multi-polarity	Sextupole	Sextupole
Field strength on the surface	10.6 kG	10.04 kG
Material	Nd-Fe-B	Nd-Fe-B
Mirror field	12 kG	13 kG
Extraction voltage	20 kV	20 kV



*Figure 2.3: Schematic [60] of the Hyper ECRIS at Center for Nuclear Study (CNS), University of Tokyo.*

chamber (actually plasma potential relative to the plasma chamber should be considered, however it is of the negligible order of 100 V). The maximum Ne and Ar beam currents for various charge states extractable from Hyper ECRIS are summarized in Table 2.2.

Table 2.2: Maximum beam currents ( $e\mu A$ ) extractable from Hyper ECRIS for Ne and Ar ions with 20 kV extraction.

Ion	Charge	6	7	8	9	10	11	12	13	14
	Ne		115	65	32	1.5				
Ar				480	220	-	43	13	11	2.2

## 2.2 Beam Line

Figure 2.4 shows the beam-line at CNS. The extracted beam was first focused on the entrance slit by the einzel lens which was installed at the place referred by EXTRACTION in Fig. 2.3, charge-state selected by the double focusing charge state analyzer, re-focused on the exit slit and then transported to each chamber by the switching magnet. Figure 2.5 shows the beam-line at RIKEN, where we ought to adjust many magnetic and electrostatic lenses and deflectors to transport the HCIs because of the longer beam-line. Both beam-lines were pumped to  $\sim 1 \times 10^{-8}$  Torr after final charge state selection by the switching magnets.

During transportation of the ion beam to the vacuum chamber, a fraction of the ions lower their charge states through electron capture process with residual gas. The density,  $n$ , of the residual gas was  $\sim 3.2 \times 10^8 / \text{cm}^3$  assuming that the beam line is filled with  $1 \times 10^{-8}$  Torr =  $133 \times 10^{-8}$  N/m<sup>2</sup> hydrogen molecule gas at 300 K. The absolute cross-section,  $\sigma$ , for one electron capture is  $6 \times 10^{-15}$  cm<sup>2</sup> [66] for 2.5 keV/amu Ar<sup>8+</sup> on H<sub>2</sub>. Hence the mean free path ( $d = 1/(n\sigma)$ ) for one electron capture is  $\sim 5 \times 10^5$  cm. Since the last straight section of our beam line was  $\lesssim 200$  cm, 99.96 % of ions kept their initial charges, *i.e.*, 0.04 % of the beam was charge-contaminated.

A part of the extracted ions from the ion source are in meta-stable states (typically 1 – 10 % depending on the operating conditions of the ECRIS). For example, meta-stable states of Ar<sup>8+</sup> are  $2p^5 3s \ ^3P_{0,2}$  or  $2p^5 3d$  whose lifetimes were calculated to be milli second order [67]. It takes  $\sim 3 \times 10^{-5}$  sec to transport the ions from the ECRIS to our experimental chamber, hence it should be kept in mind that observed spectra can contain lines emitted from the meta-stable ions.

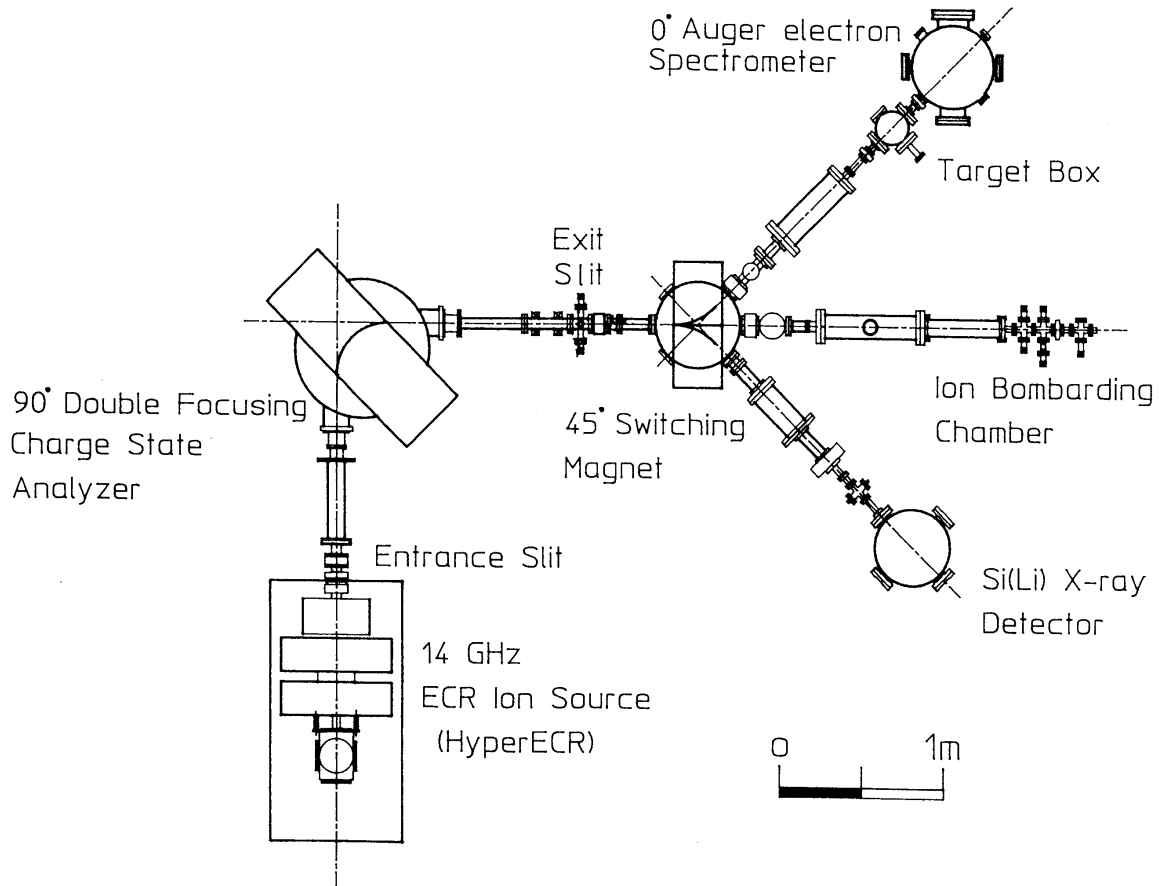


Figure 2.4: Schematic [60] of the beam-line at Center for Nuclear Study (CNS), University of Tokyo.

## 2.3 Experimental Set-up

As was stated in Section 2.1, two kinds of experimental set-ups, *i.e.*, preliminary and improved set-ups, were used with two ion sources. The preliminary one was for feasibility study to confirm whether visible lights from ions transmitted through a micro-capillary foil are actually detectable. The improved one was for measurement of quantities (wavelengths and intensities) with higher accuracies.

### 2.3.1 Preliminary Set-up

During the feasibility study, the experimental set-up illustrated in Fig. 2.6(A) was used. The vacuum chamber was first evacuated slowly down to  $1 \times 10^{-3}$  Torr with a sorption pump to avoid breaking a thin micro-capillary foil. After the rough evacuation, the chamber was pumped by a 250 l/sec turbo-molecular pump followed by a rotary pump. A reason why the sorption pump was used at the beginning of evacuation was to pump the chamber without back flow of the oils. The chamber was baked

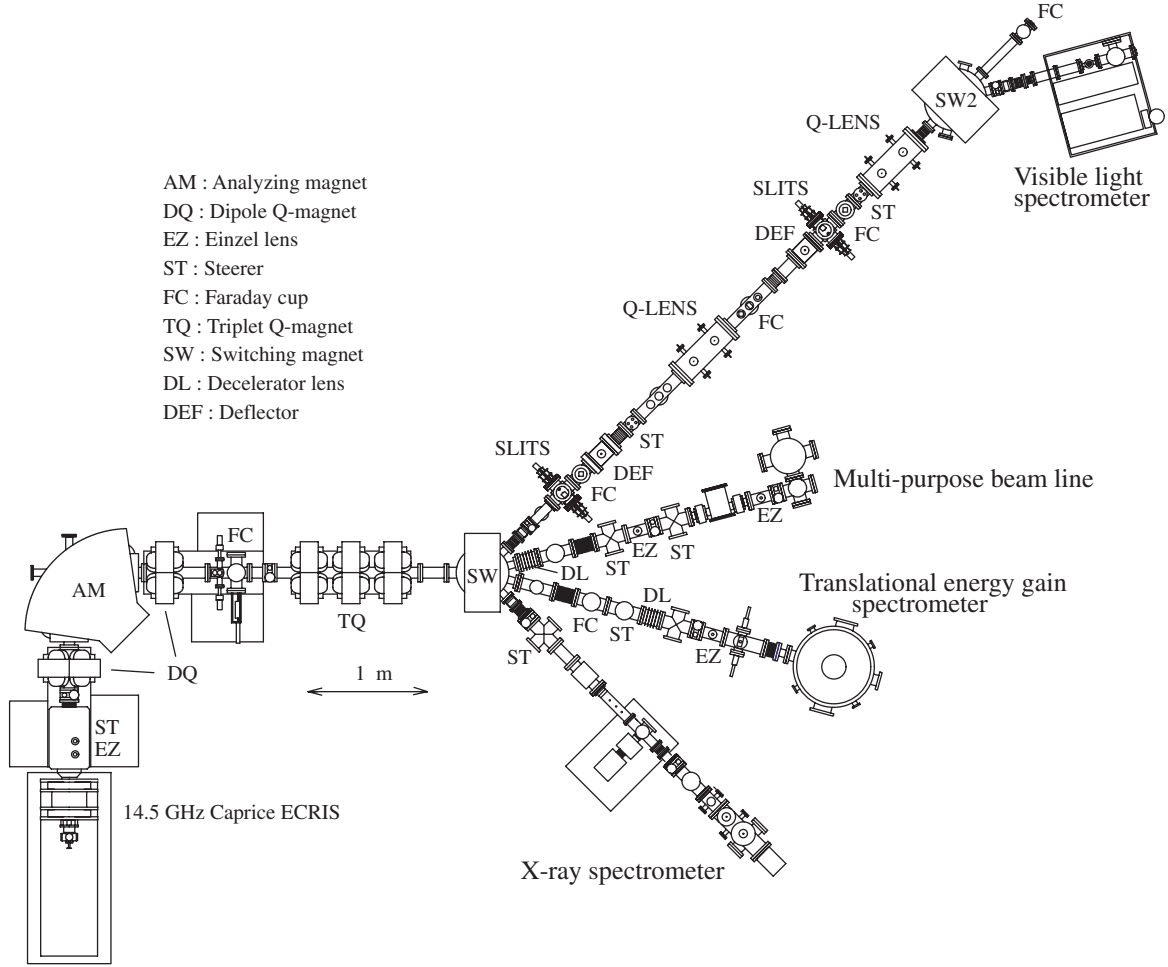


Figure 2.5: Schematic of the beam-line at atomic physics laboratory, RIKEN [64, 65].

up to  $\sim 150$  °C for a day (temperature was controlled by a solid state relay and a thermocouple) and the vacuum got better than  $5 \times 10^{-9}$  Torr within 2 – 3 days.

The ion beam supplied from the Hyper ECRIS was collimated by a four-jaw slit system and an aperture in front of the micro-capillary foil, both of which had an opening area of  $\sim 1 \times 1$  mm<sup>2</sup> and were placed  $\sim 400$  mm apart from each other, hence divergence of the beam was  $\sim 0.3^\circ$ . The beam was then incident onto the randomly distributed micro-capillary foil (see the SEM images in Fig. 1.11) with a hole diameter of 250 nm and a thickness of 1.5  $\mu$ m. As is shown in Fig. 2.6(B), the foil was mounted on a manipulator with three linear motions ( $x$ ,  $y$  and  $z$  axes), and two angular motions, *i.e.*, tilt in the  $\phi$  direction and rotation in the  $\theta$  direction. The transmitted beam was collected by the Faraday cup with a guard ring at the entrance which was biased to  $-100$  V to suppress slow secondary electrons emitted from the surface of the Faraday cup. The transmitted current was typically several nA, and the transmission efficiency was 1 – 3 %.

Photons emitted downstream of the capillary in the  $x$  direction were collected by

the optical lens (so called BK-7 lens) which was partially hidden by the slit, and focused on the entrance of the optical fiber. The entrance of the fiber has a circular cross section of 2 mm in diameter, and the exit has a rectangular cross section of  $\sim 0.8(\text{horizontal}) \times 4(\text{vertical}) \text{ mm}^2$ . The exit of the fiber was fixed to the entrance slit of the spectrometer. The slit width is variable from  $10 \mu\text{m}$  to 3 mm with a micrometer. The spectrometer used was of a Czerny-Turner type with its focal length of 500 mm (SP-500, Acton Research Corporation). It has two gratings of 1200 grooves/mm with the blaze wavelengths of 300 nm and 500 nm. The dispersion of the gratings is 1.5 nm/mm at 400 nm. Photons dispersed by the grating were collected and focused on the exit slit of the spectrometer by the spherical concave mirror. The exit slit width is also variable from  $10 \mu\text{m}$  to 3 mm with a micrometer. Then the photons were detected by the photo multiplier tube (PMT), R2757, Hamamatsu Photonics Corporation. Background noise of the PMT was around 5 cps in a stable operation (typically 2, 3 hours after power-on). Resolution of an observed line is determined by the entrance and exit slit widths of the spectrometer. Hence, it is necessary to scan wavelengths to obtain a spectrum (scanning mode).

With the set-up mentioned above, we have actually observed visible lights from the ions transmitted through the micro-capillary [68]. Figure 2.7 shows observed spectra for  $10 \times Q_{in} \text{ keV Ar}^{Q_{in}+}$  ( $8 \leq Q_{in} \leq 11$ ) ions incident on the Ni micro-capillary foil. The spectral resolutions were 1.0 nm, 2.0 nm and 4.0 nm for  $\text{Ar}^{8+}$ ,  $\text{Ar}^{9+}$  and  $\text{Ar}^{10+,11+}$  ions,

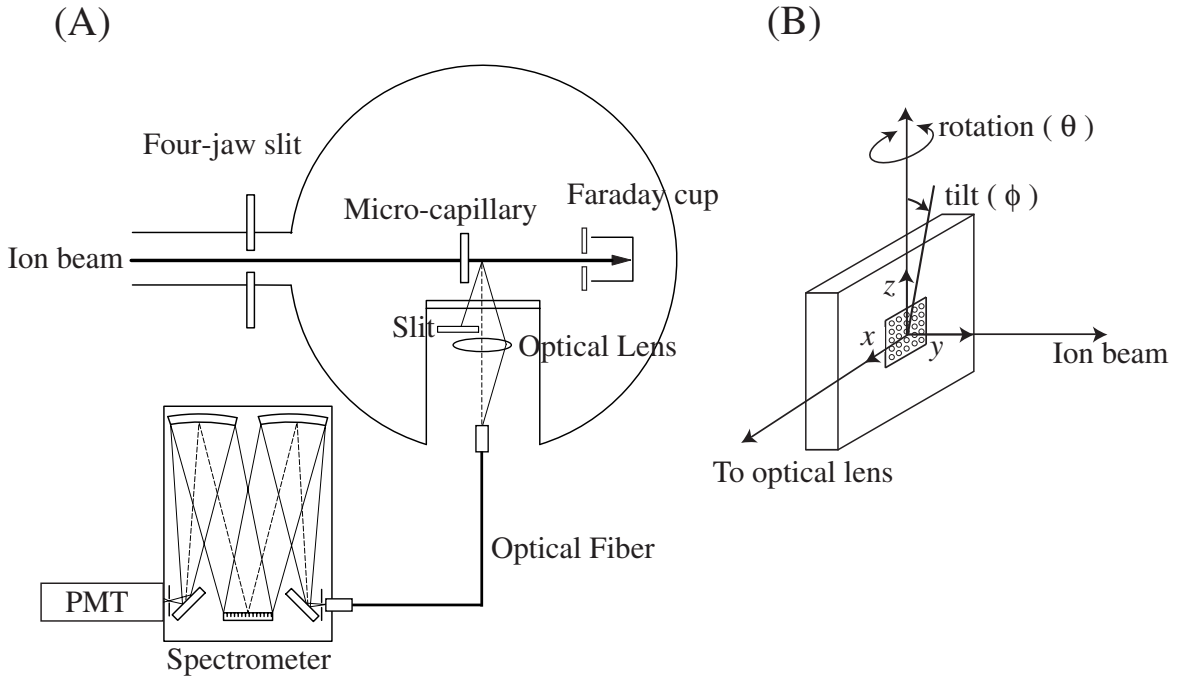


Figure 2.6: (A) An illustration of the experimental set-up used in the feasibility study. (B) A schematic around the micro-capillary.

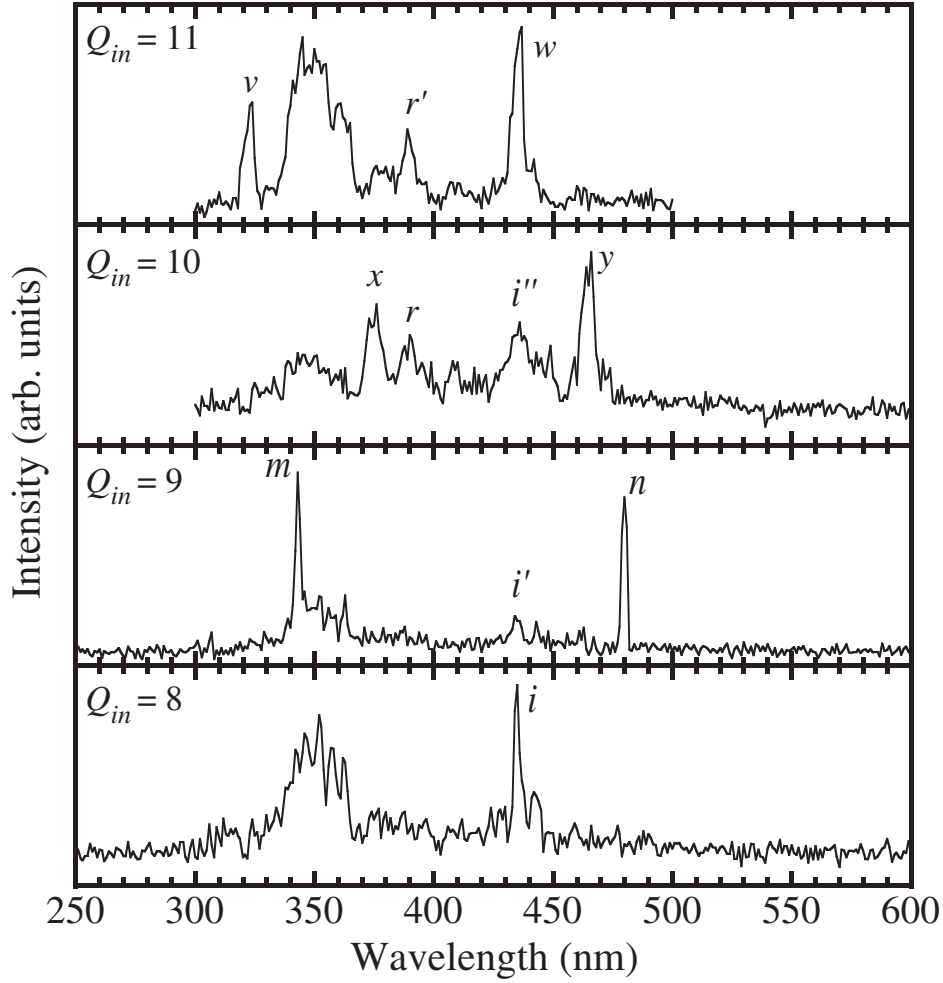


Figure 2.7: Spectra obtained for the first time in the feasibility study. The incident ions were  $10 \times Q_{in}$  keV  $Ar^{Q_{in}+}$  ( $8 \leq Q_{in} \leq 11$ ) ions.

respectively. As can be seen, there are several lines (denoted by alphabets) attributed to  $\Delta n = 1$  transitions of  $Ar^{(Q_{in}-1)+}$  ions with their principal quantum numbers of the upper states,  $n_u$ , around  $Q_{in}$  (see Section 3.1). After the observations, some questions were left, *e.g.*, whether the line  $i$  in Fig. 2.7 was composed by several transitions, or whether there were any line except the  $i$  line in the  $Q_{in} = 8$  spectrum because electron cascade should result in emission of shorter wavelength photons as shown by  $m$  and  $n$  lines in Fig. 2.7. To answer the above questions, it should be necessary to realize (1) higher resolution, (2) higher efficiency and (3) wider observed wavelength region. In the next section, a new set-up to fulfill the requirements is described (explanations common to both set-ups are not repeated).

### 2.3.2 Improved Set-up

Figures 2.8(A) and (B) show a schematic and a photograph of the improved experimental set-up. The chamber was evacuated to better than  $5 \times 10^{-9}$  Torr even when the HCI beam was supplied from the Caprice ECRIS. The beam was collimated by two apertures with 2 mm diameters which were  $\sim 300$  mm apart, hence the beam divergence was less than  $0.8^\circ$ . A Ni micro-capillary foil used was 100 nm in hole diameter and 700 nm in thickness. The foil was mounted on an  $x - y - z - \theta$  manipulator.

Several optical elements to focus the emitted photons were investigated. Figure 2.9(A) shows reflectivities of Al, Al over-coated by  $\text{MgF}_2$  and Au mirrors. Figure 2.9(B) shows transmittivities of fused and synthetic silica and BK-7 optical lenses [69]. As is seen, the BK-7 lens which was used in the feasibility study has a very small transmittivity below 300 nm. Both silica lenses and the Al mirrors are suitable for the observation in a wider wavelength region with higher efficiency. However, it is noted that optical lenses have chromatic aberration, *i.e.*, the focal length depends upon the wavelength. For example, the focal length of a synthetic silica lens varies from 270 mm to 305 mm when wavelengths are varied from 250 nm to 800 nm. This means that when a lens is used, an observed region downstream of the capillary varies according to the wavelength, which makes the analysis of the observed line intensities complex. The chromatic aberration can be compensated using an achromatic lens, however it is not perfect and practically at least two types of achromatic lenses are necessary to cover 200 – 900 nm. We selected Al mirrors over-coated by  $\text{MgF}_2$ , which cover the wide range of wavelength (200 – 1000 nm) with a small intensity loss ( $\sim 10\%$ ) without chromatic aberration. The  $\text{MgF}_2$  coat is made to prevent oxidation of the Al surface, which results in lower reflectivity especially below 300 nm. As is shown in Fig. 2.8, two flat mirrors and a spherical concave mirror were prepared and arranged so that the object on the HCI beam trajectory was imaged directly onto the entrance slit of the spectrometer with one to one imaging (see Fig. 2.8). The spherical concave mirror is 70 mm in diameter and its curvature 600 mm. The half-conical angle of the mirror system is  $2.9^\circ$ , and hence the target was rotated in the  $\theta$  direction by  $3^\circ$  so that the effective solid angle is constant even when a point very close to the capillary is observed.

Figures 2.10(A), (B) and (C) show typical quantum efficiencies of PMTs, front illuminated type CCD (charge coupled device) and back illuminated type CCD [70], respectively. Both PMT and front illuminated CCD have lower quantum efficiencies ( $\lesssim 30\%$ ) than back illuminated CCD over the wavelength region from 200 to 1000 nm. The present experiments were performed with one of the back illuminated CCD, LN/CCD - 1100PB, Princeton Instruments, with a UV/AR coating (ultraviolet anti-reflection) whose quantum efficiency is shown by the dotted line in Fig. 2.10(C)). The CCD was placed on the focal plane of the spectrometer by minimizing observed line width. The CCD consists of 1100 (Horizontal)  $\times$  330 (Vertical) pixels with the pixel

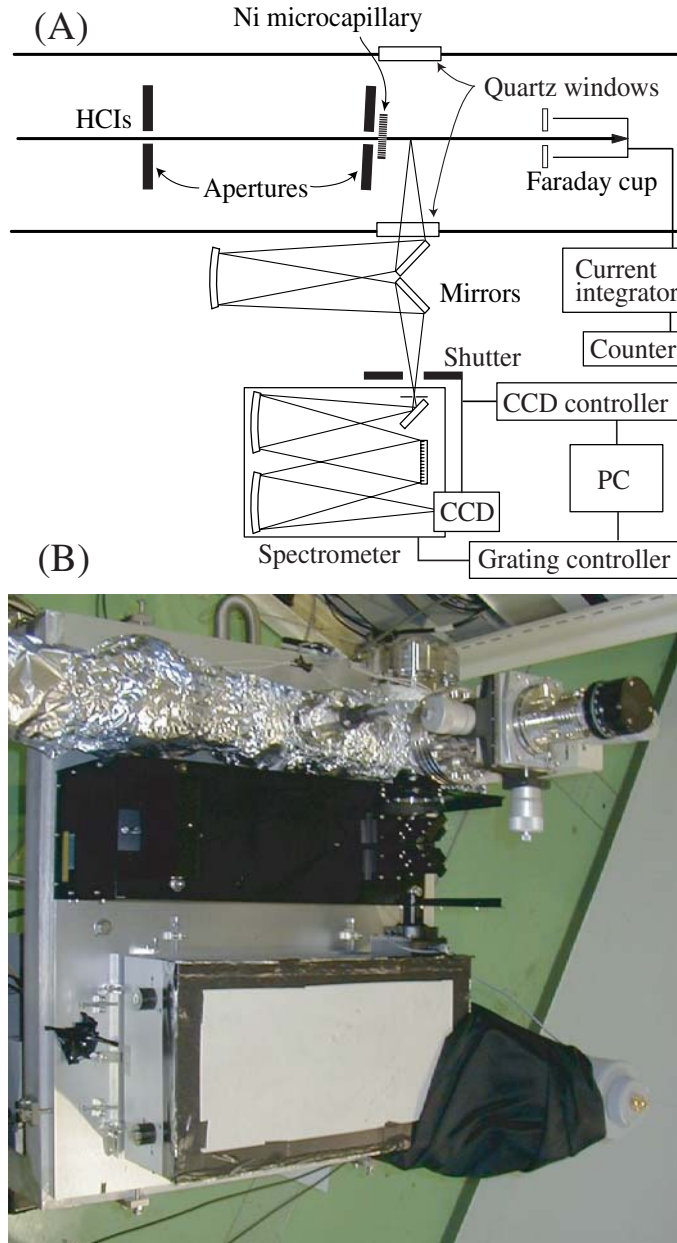


Figure 2.8: (A) A schematic of the improved set-up. (B) A photograph of it. Each apparatus is placed in the same direction for both figures.

size of  $24 \times 24 \mu\text{m}^2$ . The ultimate wavelength resolution determined by the dispersions of the gratings and the pixel size is  $\sim 0.032 \text{ nm}$  at  $400 \text{ nm}$ . The CCD covers the wavelength range of  $\sim 40 \text{ nm}$ , *i.e.*, crudely 400 times more efficient than the “scanning mode” in the feasibility study considering a typical high resolution of  $0.1 \text{ nm}$ .

The personal computer in Fig. 2.8 is connected to the CCD controller which digitizes analog signals from the CCD, controls the accumulation time by opening and closing of the shutter and maintains temperature of the CCD at  $-120 \text{ }^\circ\text{C}$  with a heater. The

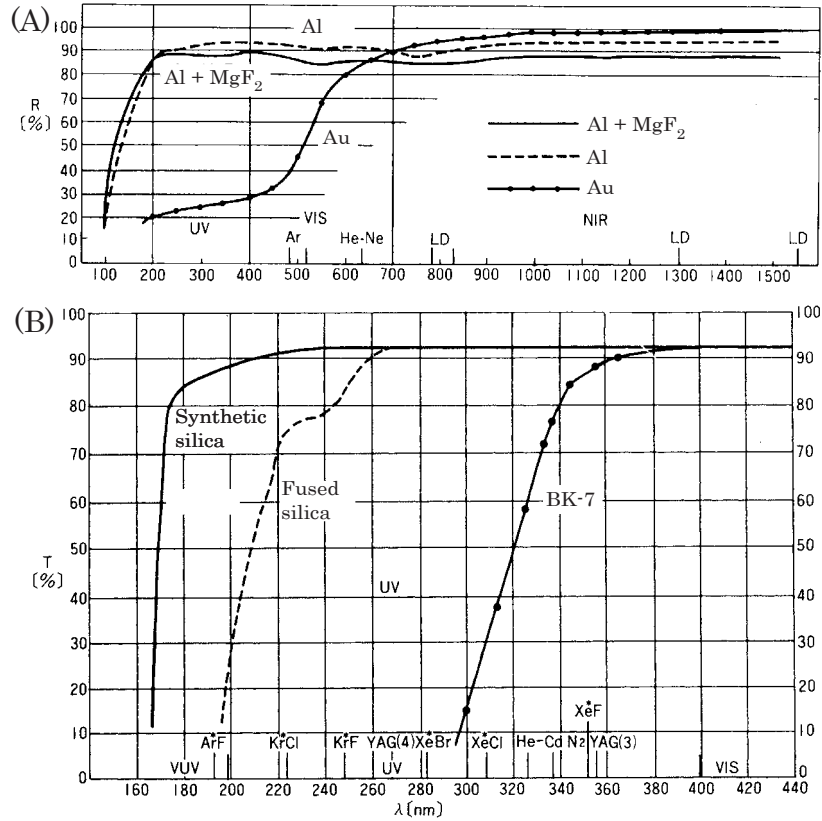


Figure 2.9: (A) Reflectivity of mirrors and (B) transmittivity of the optical lens.

computer is also connected to the grating controller which changes from one grating to the other and scans wavelengths. The gratings were selected so that the detection efficiency of the total system is optimized, *i.e.*, the 300-nm grating for  $\lambda \lesssim 430$  nm and the 500-nm grating for  $\lambda \gtrsim 430$  nm (see Section 2.3.5). The reproducibility of the wavelength position was better than 0.05 nm after change of the gratings and wavelength scan.

### 2.3.3 Wavelength and Resolution

As is shown in Fig. 2.8, the spectrometer again focuses the image on its entrance slit upon the CCD with the two spherical concave mirrors. Hence the image on the CCD is a convolution of the spectral line shape (wavelength distribution) and the distribution of the emission points downstream of the target. Figure 2.11 shows a CCD image of a reticle with 0.1 mm/div placed at the object point along the HCI beam trajectory with the entrance slit width of 3.0 mm. As was designed, the image on the CCD has the same size as the object. It is also seen that the vertical lines on the reticle are recognized more clearly than the numbers above the vertical lines (which are 40, 50

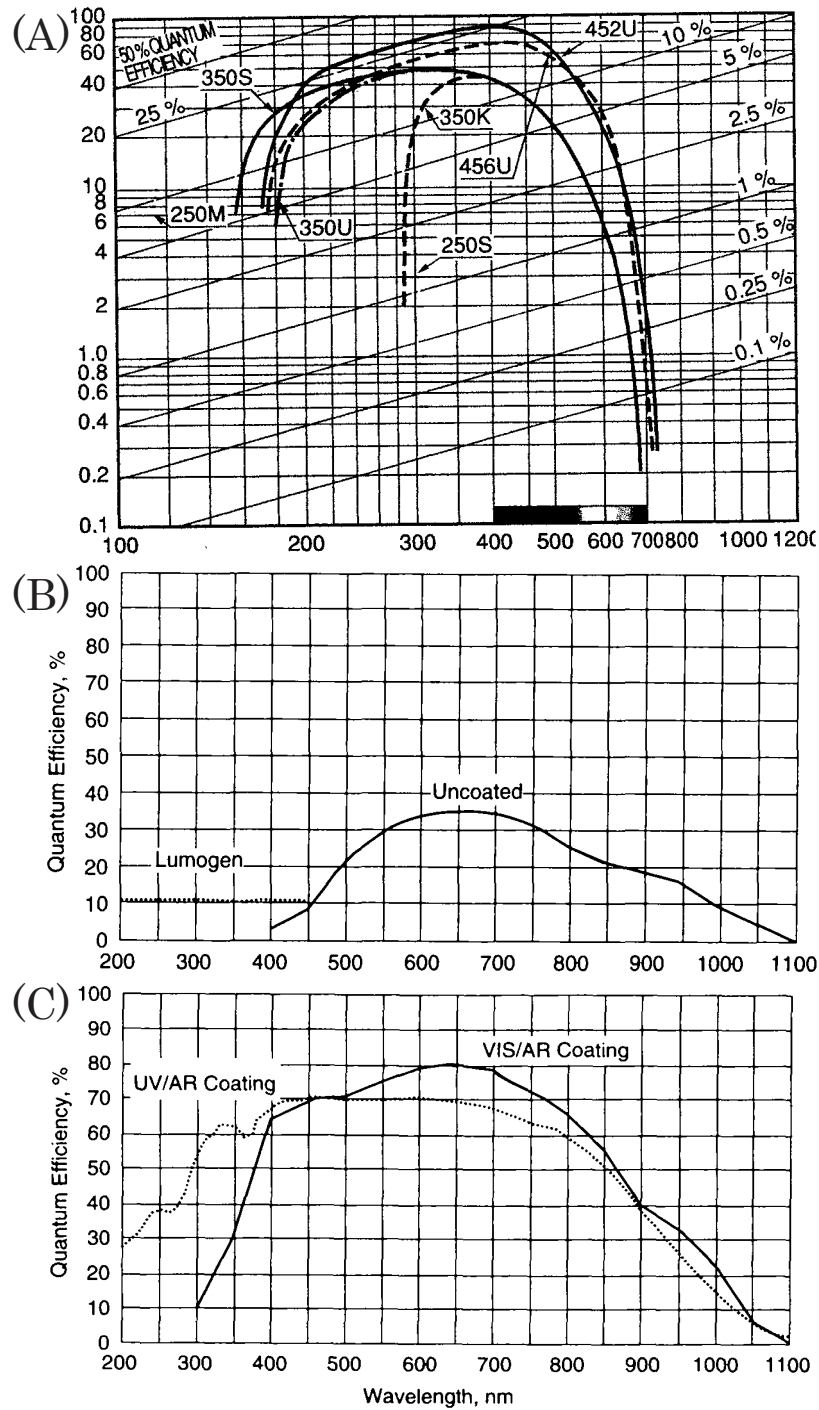


Figure 2.10: Quantum efficiencies of (A) PMTs, (B) front illuminated CCD and (C) back illuminated CCD.

and 60 from left to right in Fig. 2.11). This is because astigmatism of the spectrometer makes the image obscure along the vertical direction.

It is noted that the resolution of the observed line depends not only upon the slit width but also upon the Doppler broadening. When a photon with wavelength  $\lambda_0$  from

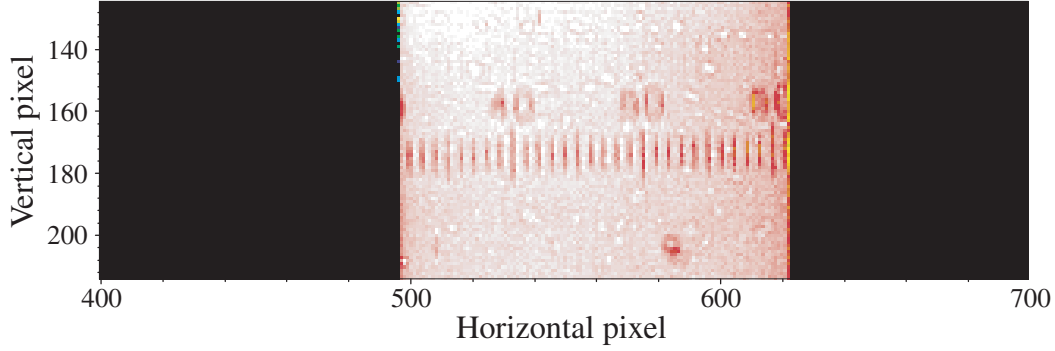


Figure 2.11: A CCD image of the reticle on the beam trajectory.

an ion moving with a velocity  $v$  is detected at an angle  $\theta$  with its half acceptance angle  $\alpha$  (see Fig. 2.12), the wavelength of the observed photon ( $\lambda_{obs}$ ) is Doppler shifted and has a line width of  $\delta\lambda \approx |\lambda_1 - \lambda_2|$  due to the Doppler broadening, *i.e.*,

$$\begin{aligned}\lambda_{obs} &= \lambda_0 \gamma (1 - \beta \cos \theta), \\ \delta\lambda &\approx 2\lambda_0 \gamma \beta \sin \theta \sin \alpha \quad (\theta \geq \alpha), \\ \beta &= \frac{v}{c}, \quad \gamma = \frac{1}{\sqrt{1 - \beta^2}}.\end{aligned}\tag{2.2}$$

In the case of  $\alpha = 3.0^\circ$ ,  $\theta = 90^\circ$ ,  $\lambda_0 = 500$  nm and the ion kinetic energy of 2.0 keV/amu,  $\delta\lambda$  is estimated to be  $\sim 0.1$  nm.

Horizontal pixel positions on the CCD were converted to wavelengths using several line positions of a low-pressure mercury lamp and a cadmium/neon hollow cathode lamp whose wavelengths are given as those in the standard air, *i.e.*, dry air at 760 Torr and 15 °C. A linear interpolation was used for the conversion between wavelengths and pixel positions. It was found that wavelengths of the other lines which were not used in the calibration were reproduced by the interpolation within  $\sim 0.05$  nm. The observed wavelengths in air,  $\lambda_{air}$ , were converted to those in vacuum,  $\lambda_{vac}$ , using a so-called Edlén formula [71] for the refractive index,  $n$ , of the standard air given by

$$\begin{aligned}n &= 1 + \left( 8342.13 + \frac{2406030}{130 - \sigma^2} + \frac{15997}{38.9 - \sigma^2} \right) \times 10^{-8}, \\ \sigma &= \frac{1}{\lambda_{air}}, \quad \lambda_{vac} = n\lambda_{air},\end{aligned}\tag{2.3}$$

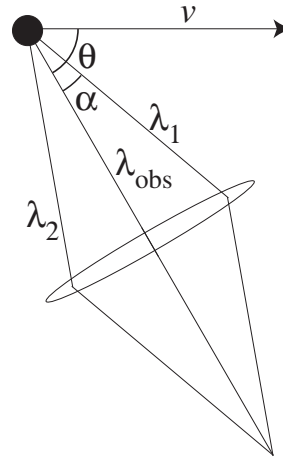


Figure 2.12: Doppler shift and broadening.

where  $\lambda_{air}$  is in unit of  $\mu\text{m}$ .  $\lambda_{air} - \lambda_{vac}$  amounts to  $\sim +0.1$  nm in the wavelength range considered here.

### 2.3.4 Data Acquisition

The CCD has three types of noises, *i.e.*, a thermal noise, readout noise, and spike noise. Thermal noise comes from electron-hole pair creations by thermal agitation, and is expected to be proportional to the accumulation time of the CCD. Figures 2.13(A) and (B) show the spectra obtained when the accumulation time is 0.1 sec and 300 sec, respectively. As is seen, background levels in both figures are almost the same, *i.e.*, thermal noise is of minor importance in the present case.

The readout noise (fluctuation of the background level) makes a major contribution to the total noise and unavoidably appears during amplification. The CCD readout system used here has two modes of readout, *i.e.*, one-dimensional (1D) and two-dimensional (2D) readouts. In the 2D readout mode, electrons in each pixel are transferred pixel by pixel to a pre-amplifier, *i.e.*, the total number of readout operations is  $1100 \times 330$ . On the other hand in the 1D readout mode, electrons in the same column are first summed up, and transferred to the pre-amplifier, *i.e.*, the total number of the readout operations is 1100. Figure 2.14(A) shows spectra of a mercury lamp taken for the same accumulation time with the 1D (below) and the 2D (above) readouts, where the intensities for the 2D spectrum are summed up along the column after the A/D conversion. Two spectra clearly show that the photon intensities are the same level with each other but the fluctuation of the background in the 2D readout is  $\sim 20$  times larger than that in the 1D readout.

Although the 1D readout is very effective to suppress the readout noise, it is very weak against spike noises. Figure 2.14(B) shows a typical one-dimensional spectrum for accumulation time of 500 sec. Many sharp and intense lines observed are so-called spike noises which randomly distribute over the whole active area of the CCD. A typical count rate of them is  $\sim 2.8 \times 10^{-7}$  /sec/pixel, which corresponds to  $\sim 0.1$  /sec over

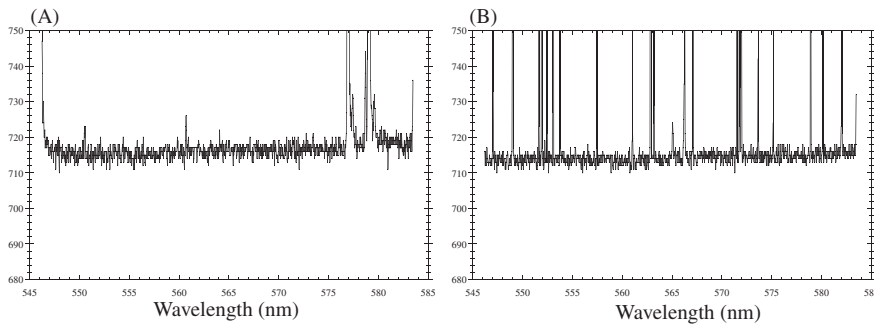


Figure 2.13: Spectra for (A) 0.1 sec and (B) 300 sec exposure time.

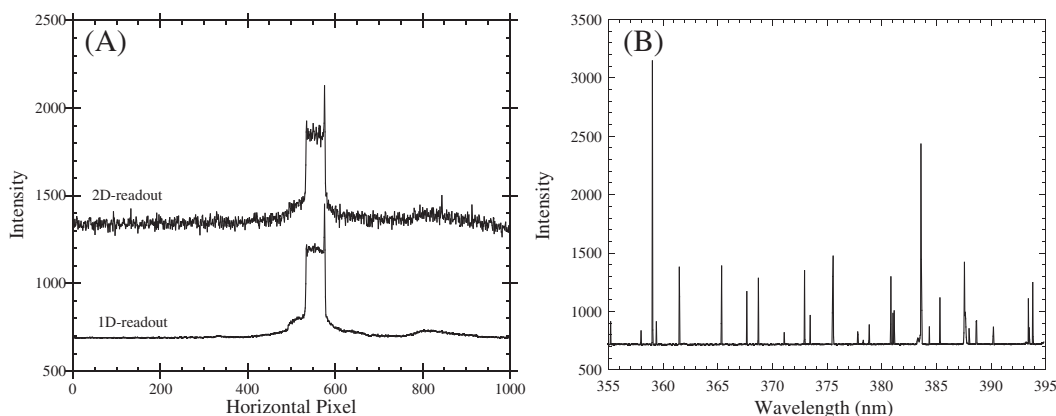


Figure 2.14: (A): Spectra for 1D (below) and 2D (above) readout with the same exposure time. (B): 1D spectrum under a 500 sec exposure.

the active area of the CCD. Because only a couple of neighboring pixels (dead pixels) are charged strongly by a spike noise, it is rather easy to remove them in the case of the 2D readout even after several hours accumulation. However because of summing up along the column, it is very serious even for  $\sim 5$  minutes accumulation in the 1D readout. For example, while the number of dead pixels for 2 hours exposure with the 2D readout is about 720 pixels out of  $1100 \times 330$  pixels, those for 5 minute exposure with the 1D readout is about 30 columns out of 1100 columns. By limiting the number of rows within 150 pixels by a CCD driver in the 1D readout (This means that the image of the beam are within 150 pixels along the column), the number of the spike noises was half reduced resulting in about twice longer accumulation time. A typical accumulation time in 1D readout was  $\sim 500$  sec in which  $\sim 90\%$  of the total columns was useful. Actually in experiments, the total accumulation time to obtain a spectrum in a wavelength range is  $\sim 2$  hours, *i.e.*, one accumulation in the 2D readout or twenty accumulations in the 1D readout were necessary. Accounting also for the strong readout noise reduction for the 1D readout, the 1D readout was used in the experiment.

We have used two different ways to get rid of the spike noises and make a summed spectrum from a number of 1D spectra. In Chapter 3 which is devoted to identify individual transitions, the intensity of each line was not critically important. When a spike noise was found in a column, intensities in the column and the neighboring two columns were ignored in the summation. After summing up the spectra, the intensity in each column was normalized so that the number of the spectra is the same for all of the columns, *i.e.*, the resultant spectral intensity was not normalized to the transmitted current strictly. When an intensity for each line has an important meaning (in Chapter 4), the line which was suffered from the spike noise was completely ignored in the summation, and then line intensities were evaluated taking into account the

transmitted currents.

There are two different types of broken pixels along the column in the CCD, “hot” and “cold” pixels. In the hot pixels, dark currents always flow through, which results in large counts after A/D conversion. On the other hand, the cold pixel does not respond to photons and always yields no count. As is shown in Fig. 2.15, the present CCD has two hot columns at 1100th and 1099th columns, which are close to the edge of the active area. The cold columns are at the 151st, 536th, 702nd, 714th and 1025th columns. During the experiments, particular attention was paid so that no cold column overlaps with the observed line positions, else the line is observed as if it consists of two components.

### 2.3.5 Intensity Calibration

In Chapter 4, line intensities were converted to relative photon numbers taking into account the wavelength-dependent efficiency of the imaging mirror system, the spectrometer and the CCD. A standard deuterium lamp and a standard tungsten lamp were used to calibrate from 200 nm to 400 nm and from 350 nm to 800 nm, respectively. For both lamps, spectral irradiance ( $\mu\text{W}/\text{cm}^2\text{nm}$ ) is given as a function of wavelength (10 nm and 50 nm intervals for the deuterium and tungsten lamps, respectively), which was converted to the photon flux ( $\text{photon}/\text{cm}^2\text{sec}$ ) dividing the irradiance by the corresponding photon energy. The ratio between observed intensities per nm and the photon flux gives the detection efficiency curve of the whole experimental set-up. For a wavelength region with  $\lambda \geq 400$  nm, photons with  $\lambda$  in the first order diffraction are contaminated by those with  $2\lambda$  in the second order diffraction. Optical filters were used to eliminate second order photons. As is shown in Figs. 2.16 (A) and (B), transmission efficiencies of the filters become constant for the wavelength region longer than the

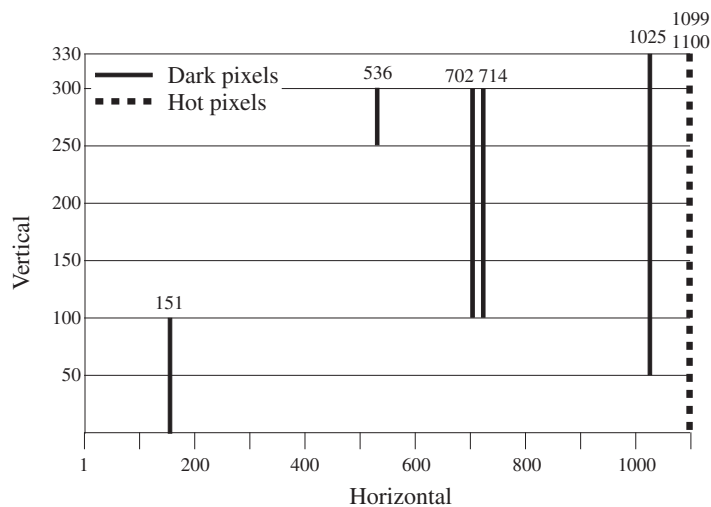


Figure 2.15: Distribution of the dark and hot pixels in the present CCD.

cut-off wavelengths by  $\sim 50$  nm. The optical filters with 300 nm and 500 nm cut-off wavelengths were used for calibrations in 350 – 600 nm and 550 – 800 nm wavelength ranges, respectively (referred 30 and 50 in Figs. 2.16(A) and (B)). In 200 – 400 nm range, calibration was done without filters because photons below 200 nm can hardly transmit through the experimental apparatus (see Fig. 2.17). The resultant calibration data in three different wavelength ranges were connected with each other using data common to each wavelength range. A relative detection efficiency thus obtained for each grating is shown in Fig. 2.17.

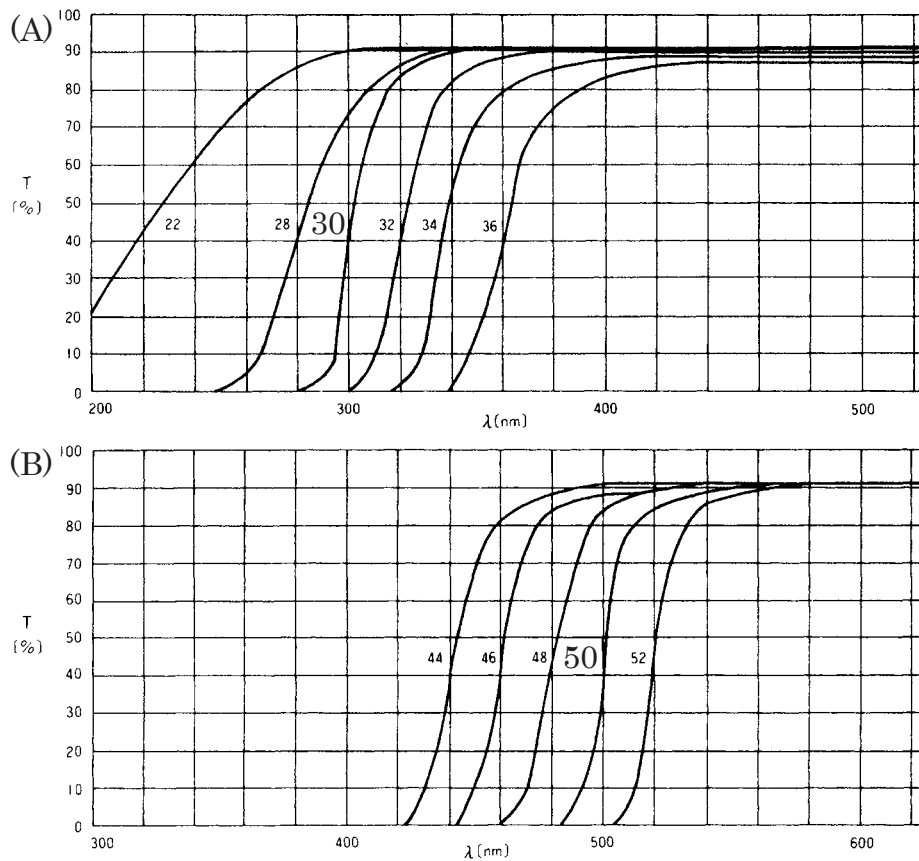


Figure 2.16: Transmission efficiencies of the cut-off filters for (A) 300 nm and (B) 500 nm

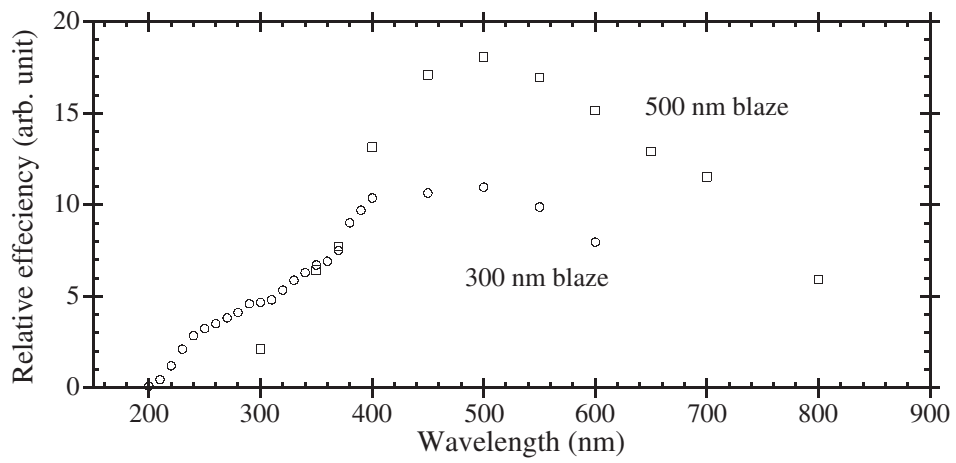


Figure 2.17: Relative detection efficiencies for gratings of 300-nm blaze ( $\circ$ ) and 500-nm blaze ( $\square$ ).

# Chapter 3

## Spectroscopic Study

The following chapters show and discuss the experimental results. Detailed transitions of the observed lines will be identified in this chapter, which is essential to analyze the observed line intensities in the next chapter because transition rates depend upon  $n$  and  $\ell$ .

### 3.1 Overall spectra

Figure 3.1 shows spectra for 2.0 keV/amu  $\text{Ar}^{Q_{in}^+}$  ions ( $6 \leq Q_{in} \leq 10$ ) incident on a Ni micro-capillary foil of 700 nm in thickness and 100 nm in hole-diameter. The ordinate in each spectrum is corrected against the detection efficiency of the whole detection system, *i.e.*, the ordinate is proportional to the number of photons emitted. The width of the entrance slit of the spectrometer was set to 3.0 mm, which corresponds to the intrinsic resolution of the spectrometer of  $\sim 4.5$  nm at 400 nm. Because the exit surface of the capillary was placed within the time window of the apparatus, the effective resolution of each spectrum was  $\delta\lambda \approx 4.0$  nm and the time window was 4.3 ns, *i.e.*, photons emitted between  $t = 0$  ns and  $t = 4.3$  ns were collected (see Section 2.3.3).

There seems to be, at first glance, two types of lines in Fig. 3.1, *i.e.*, lines observed for all incident charges (*e.g.*, broad peak at 350 nm) and those specific to the charge states of the incident ions. The former type of lines are attributed to Ar or Ni atom/ions with low charge states, which will be discussed in detail in Section 3.2. The latter type of lines can be attributed to transitions of transmitted ions, which are labeled by italic alphabetical letters. Lines originated from the second order diffraction are referred to as “2” in Fig. 3.1. The lines were easily identified assuming energy levels to be hydrogen-like, *i.e.*,

$$E_n = -\frac{Q_{in}^2}{2n^2}. \quad (3.1)$$

Table 3.1 (page 51) compares the wavelengths of the observed lines with those of  $\Delta n = n_u - n_l = 1$  transitions calculated for different core charges,  $Q_{in}$ , and principal quantum

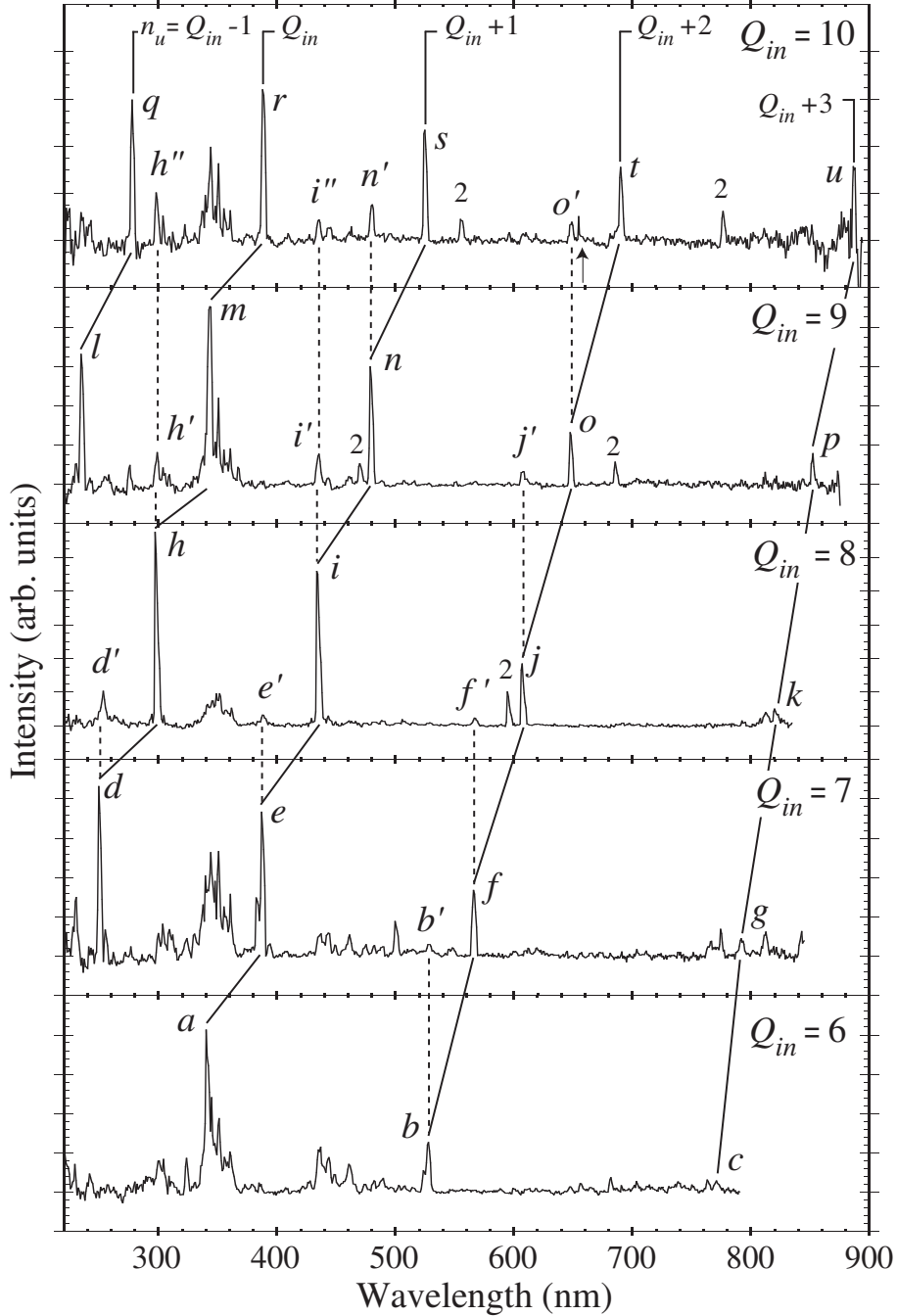


Figure 3.1: Spectra observed with 2.0 keV/amu  $Ar^{Q_{in}^+}$  ions ( $6 \leq Q_{in} \leq 10$ ). The ordinate of each spectrum is proportional to the number of the emitted photons. Lines labeled by alphabetical letters are identified as  $\Delta n = 1$  transitions, and transitions represented as  $n_u = Q_{in} + s$  ( $-1 \leq s \leq 3$ ) are connected with the solid lines. Lines labeled by dashed letters indicates transitions after multiple electron capture, which are connected by dashed lines. Lines labeled by 2 represent the second order diffraction.

numbers for upper states,  $n_u$ . The calculated and observed wavelengths agree with each other within the experimental wavelength accuracies. In Fig. 3.1,  $n_u$  is given using  $Q_{in}$  as a parameter. The solid lines connect transitions with  $n_u = Q_{in} + s$  among different  $Q_{in}$  for a fixed  $s$  ranging from  $-1$  to  $3$ . For example, the line labeled by “ $i$ ” in Fig. 3.1 corresponds to the  $\Delta n = 1$  transition with  $n_u = 9$  ( $n_u = Q_{in} + 1$  for  $Q_{in} = 8$ ). It is seen that the line intensities corresponding to  $n_u = Q_{in}$  are the strongest and become weaker monotonously toward those with  $n_u = Q_{in} + 3$ .

Although the present detection system has no sensitivity to  $\Delta n = 1$  transitions with  $n_u = Q_{in} + 4$  ( $\lambda \approx 1100$  nm), populations of these states (if populated) can be confirmed observing  $\Delta n = 2$  transitions whose wavelengths are shown in Fig. 3.2. Such transitions, however, were hardly recognized in Fig. 3.1. These facts are partially consistent with the prediction of the COB model that the first electron transfer takes place to  $n_u \approx Q_{in} + 1$  states (see Eq. 1.11).

It is commonly seen in Fig. 3.1 that strong lines attributed to one electron capture in  $\text{Ar}^{Q_{in}+}$  spectrum are also observed in  $\text{Ar}^{(Q_{in}+1)+}$  and  $\text{Ar}^{(Q_{in}+2)+}$  spectra. The dashed lines connect such transitions. This indicates that the incident  $\text{Ar}^{(Q_{in}+1)+}$  ion has captured two or more electrons in its high-lying Rydberg states, and one or more electron(s) cascade down and fill the core hole(s) through radiative or Auger transitions with one electron still remained in the high-lying Rydberg states. As was discussed in Section 2.2, a small fraction ( $\sim 0.04$  %) of ions capture electrons from residual gas during transportation through the beam line. Such ions also yield similar lines in higher charge-state spectra. However the observed intensity ratios are  $\gtrsim 5$  %, *e.g.*, ratio between lines  $i'$  and  $i$  is  $\sim 20$  %, which is much larger than  $0.04$  %.

Finally, we comment on the line pointed at with the arrow in the  $Q_{in} = 10$  spectrum in Fig. 3.1 (at right hand side of the  $o'$ ). Although we can not determine even its charge-state, this line can also be attributed to transitions of transmitted Ar ions because the line is specific to the incident charge. It is noted that all the observed lines except this line have a line width determined by the entrance slit of the spectrometer ( $\sim 4$  nm). This line has a much narrower width of  $\sim 0.3$  nm, *i.e.*, the lifetime of the initial state is much shorter than the transmission time of the ion to pass the slit width ( $\sim 4.3$  ns). One possibility to explain such a short lifetime is a multiply excited state which decays primarily via auto-ionization.

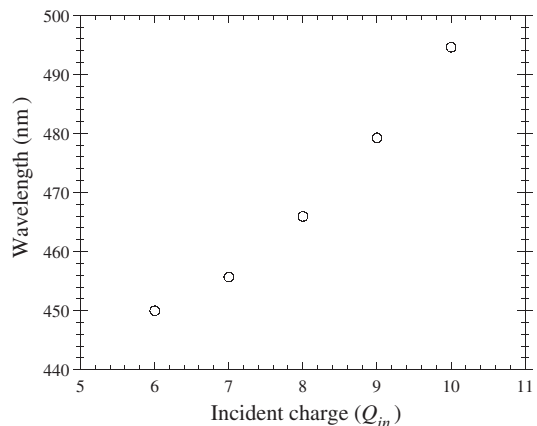


Figure 3.2: Wavelengths for  $\Delta n = 2$  transitions with  $n_u = Q_{in} + 4$ .

Table 3.1:  $\Delta n = 1$  transition wavelengths calculated assuming energy levels as hydrogen-like and observed wavelengths. The last column shows the letters in Fig. 2.7 and Fig. 3.1.

$Q_{in}$	$n_u$	$E_{n_u} - E_{n_u-1}$ (nm)	Observed wavelength (nm)	
11	11	434	$436.0 \pm 2.0$	<i>w</i>
	10	321	$323.8 \pm 2.0$	<i>v</i>
10	13	887	$887.0 \pm 2.0$	<i>u</i>
	12	690	$690.5 \pm 2.0$	<i>t</i>
	11	525	$525.0 \pm 2.0$	<i>s</i>
	10	388	$389.0 \pm 2.0$	<i>r</i>
	9	278	$278.0 \pm 2.0$	<i>q</i>
9	12	852	$852.0 \pm 2.0$	<i>p</i>
	11	648	$648.0 \pm 2.0$	<i>o</i>
	10	480	$479.5 \pm 2.0$	<i>n</i>
	9	343	$343.0 \pm 2.0$	<i>m</i>
	8	235	$235.0 \pm 2.0$	<i>l</i>
8	11	820	$821.0 \pm 2.0$	<i>k</i>
	10	607	$607.5 \pm 2.0$	<i>j</i>
	9	434	$435.5 \pm 2.0$	<i>i</i>
	8	298	$299.0 \pm 2.0$	<i>h</i>
7	10	793	$792.0 \pm 2.0$	<i>g</i>
	9	567	$566.0 \pm 2.0$	<i>f</i>
	8	389	$388.0 \pm 2.0$	<i>e</i>
	7	252	$250.0 \pm 2.0$	<i>d</i>
6	9	772	$771.0 \pm 2.5$	<i>c</i>
	8	529	$528.0 \pm 2.0$	<i>b</i>
	7	343	$341.5 \pm 2.0$	<i>a</i>

## 3.2 High Resolution Spectrum

In the overall spectra, the principal quantum numbers involved in the transitions were identified with the simple assumption of hydrogen-like energy levels. However,  $\text{Ar}^{Q_{in}+}$  ions used in the experiments have ionic cores of finite sizes and their electronic potentials are more or less different from Coulombic, *i.e.*, transition wavelengths should depend also upon angular momentum quantum numbers of upper states,  $\ell_u$ . To resolve

lines with the same  $n_u$  but with different  $\ell_u$ , experiments with much higher resolution were performed (entrance slit width of the spectrometer was set to 0.07 mm corresponding to the intrinsic resolution of 0.11 nm). Because  $\text{Ar}^{Q_{in}^+}$  ions with  $Q_{in} \geq 9$  have  $L$ -shell holes, which makes the atomic structure very complex, we investigated  $\text{Ar}^{5+}$  ( $1s^2 2s^2 2p^6 3s^2 n\ell^1$ ),  $\text{Ar}^{6+}$  ( $1s^2 2s^2 2p^6 3s^1 n\ell^1$ ) and  $\text{Ar}^{7+}$  ( $1s^2 2s^2 2p^6 n\ell^1$ ) ions.

### 3.2.1 Light from Sputtered Particles

Here we discuss in more detail about the lines observed for all incident charges with approximately the same intensities in Fig. 3.1. To identify these lines makes it experimentally possible to recognize lines emitted from Ar ions which have been transferred one electron in the capillary. The middle two spectra in Figs. 3.3(A) and (B) show examples of high-resolution spectra of such lines when 2.0 keV/amu  $\text{Ar}^{7+}$  (red spectrum) and  $\text{Ar}^{6+}$  (blue spectrum) ions impinged. The observed region was  $\sim 0.8$  ns downstream of the exit surface of the capillary with the time window of 0.1 ns. We looked up compiled transition wavelengths,  $\lambda_{n_u, J_u}^{n_l, J_l}$ , and the corresponding transition rates,  $A_{n_u, J_u}^{n_l, J_l}$ , of Ni [72] and Ar [73, 74] atoms/ions with lower charge states to identify these lines. Synthetic spectra were then generated convoluting the compiled lines with a resolution  $\Delta\lambda$ , *i.e.*,

$$I(\lambda) = \sum_{n_u, J_u} g A_{n_u, J_u}^{n_l, J_l} \frac{1}{\Delta\lambda\sqrt{2\pi}} \exp\left(-\frac{1}{2} \left(\frac{\lambda - \lambda_{n_u, J_u}^{n_l, J_l}}{\Delta\lambda}\right)^2\right), \quad (3.2)$$

where  $I(\lambda)$  is the intensity at wavelength  $\lambda$  and  $g = 2J_u + 1$  is the statistical weight for the upper state in the transition. One of the reasons why the  $gA$ -proportional spectrum is generated will be shown in Section 4.1. There are many lines in the compiled data which have not been identified except charge states. In such a case,  $gA$  values were assumed to be  $0.1 \times 10^8 \text{ sec}^{-1}$ . A full width at half maximum (FWHM) of the Gaussian function,

$$\delta\lambda = 2\sqrt{2\log 2}\Delta\lambda, \quad (3.3)$$

is set to 0.2 nm. In Figs. 3.3(A) and (B), green and black spectra at the top show the resultant synthetic spectra for Ni I and II transitions and green, black and blue spectra at the bottom show those for Ar I, II and III transitions, respectively. The dotted lines connect between the lines observed for both incident ions and the lines in the synthetic spectra. It is found that lines in the wavelength region 328 – 335 nm and 335 – 355 nm in Fig. 3.3(A) are attributed to transitions of  $\text{Ar}^{2+}$  ions (Ar III, blue spectrum at the bottom) and Ni atoms (Ni I, green spectrum at the top), respectively, and lines in the wavelength region 430 – 470 nm to those of  $\text{Ar}^+$  ions (Ar II, black spectrum at the bottom). As can be seen in the spectra given in Appendix C (page 99), most of the lines observed for both  $\text{Ar}^{6+}$  and  $\text{Ar}^{7+}$  incident ions with similar intensities were attributed to

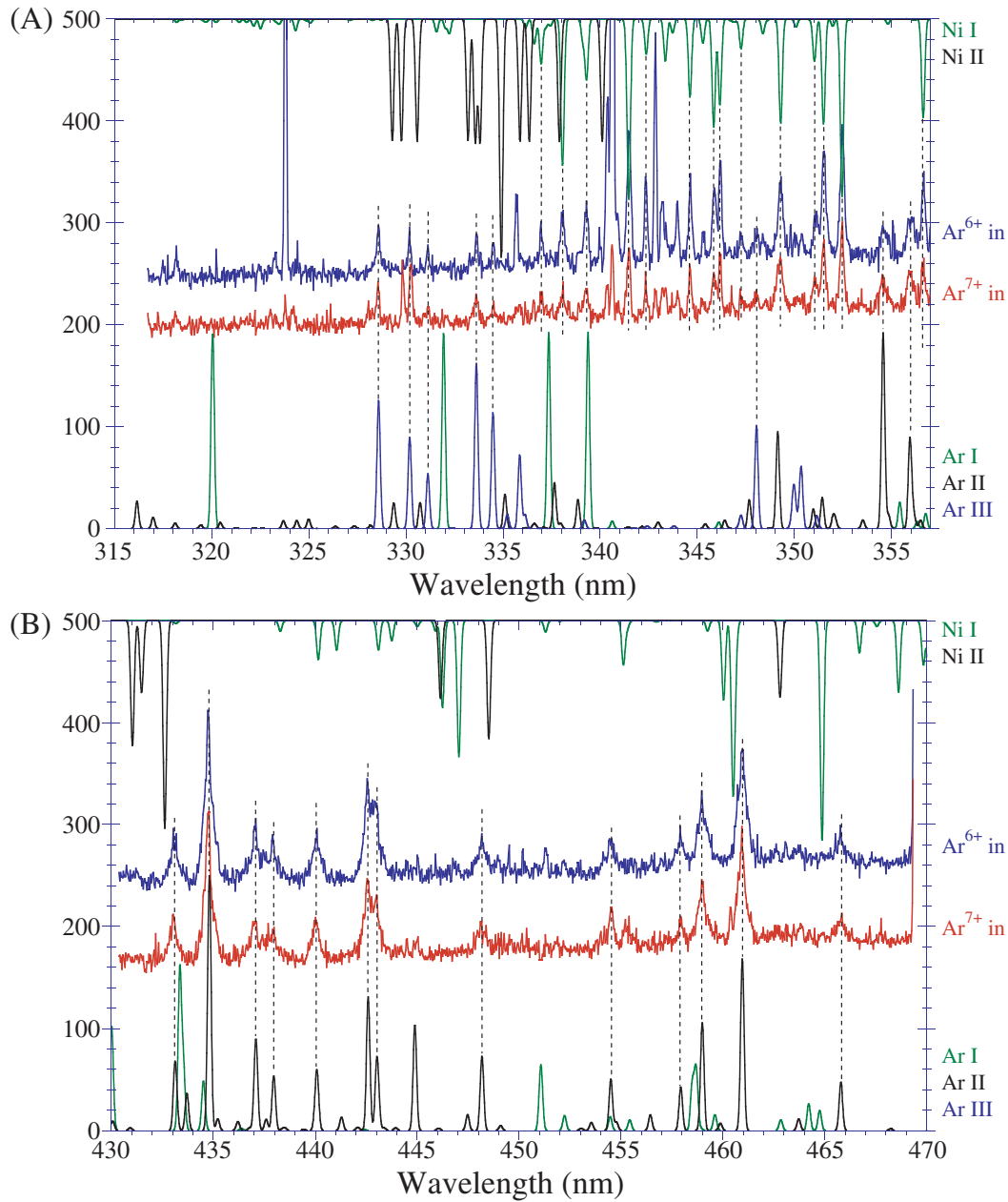


Figure 3.3: Two spectra in the middle show observed spectra when 2.0 keV/amu  $Ar^{6+}$  (blue) and  $Ar^{7+}$  (red) ions impinged onto the capillary. Top and bottom spectra are synthetic spectra generated using tabulated data. Lines around 335 nm were attributed to transitions from Ni I (green) and the lines around 450 nm to transitions from Ar II (black). A fact that observed lines have the same intensities for  $Ar^{6+}$  and  $Ar^{7+}$  incidences, shows that these atoms/ions are formed in the kinetic sputtering process.

transitions of Ni atoms or Ar<sup>+</sup> ions, *i.e.*, lines from Ni<sup>+</sup> or Ar<sup>0+,2+</sup> are hardly recognized (only a few Ar<sup>2+</sup> lines are observed with very weak intensities). Most of the Ar II lines result from  $1s^2 2s^2 2p^6 3s^2 3p^4 4p^1 - 1s^2 2s^2 2p^6 3s^2 3p^4 4s^1$  transitions. On the other hand, most of the Ni I lines result from  $1s^2 2s^2 2p^6 3s^2 3p^6 3d^9 4p^1 - 1s^2 2s^2 2p^6 3s^2 3p^6 3d^9 4s^1$  transitions around 330 – 350 nm, and  $1s^2 2s^2 2p^6 3s^2 3p^6 3d^8 4s^1 4p^1 - 1s^2 2s^2 2p^6 3s^2 3p^6 3d^9 4s^1$  transitions around 300 – 315 nm in Appendix C (the ground state of the Ni atom is  $1s^2 2s^2 2p^6 3s^2 3p^6 3d^8 4s^2 \ ^3F_4$ ). It is not known why only singly charged Ar ions and neutral Ni atoms emit photons in the observed wavelength range. However, the formation processes of such atoms/ions can be understood reasonably as follows. As was explained in Fig. 1.12, an ion entering very close to the capillary wall makes a violent collision with the capillary wall. As a result, target atoms are kicked out from the surface by the ion or recoiled target atoms (kinetic sputtering). In kinetic sputtering of the metal surface, mass, velocity and incident angle of the incident ions are important parameters to determine the sputtering process [75], and the charge state of the incident ions is expected to be a less important parameter because the ions are quickly neutralized before touching the surface atoms in this velocity range. The fact that most of the lines in Figs. 3.3 have a similar intensity for both Ar<sup>7+</sup> and Ar<sup>6+</sup> incidences supports the above consideration (note that both ions have the same mass, velocity and incident angle, but different charges).

As is clearly seen in Figs. 3.3(A) and (B), the Ar II lines have broader line widths than the Ni I lines ( $\sim 0.5$  nm and  $\sim 0.2$  nm for Ar II and Ni I lines, respectively). Here the intrinsic resolution (without the Doppler effect) of the spectrometer is  $\sim 0.11$  nm. In general, kinetically sputtered particles have average energies around 10 eV [76]. Assuming that the Ni atoms are emitted in the random directions with 10 eV kinetic energy, the Doppler broadening is estimated to be 0.02 nm, which is too small to explain the observed Ni line widths. To reproduce the observed line width, the kinetic energy of the Ni atom has to be  $\sim 200$  eV, which is rather energetic than the average energy in the sputtering. This indicates that due to the finite distance (0.65 mm) between a sputtered region and the observed region, Ni atoms with faster velocity can reach the observed region keeping one electron in the excited states (Ni atoms with 200 eV kinetic energy take  $2.5 \times 10^{-8}$  sec to move 0.65 mm). On the other hand, lines from Ar<sup>+</sup> have broad line widths of  $\sim 0.5$  nm (including the intrinsic resolution of the spectrometer, 0.11 nm). Assuming that the observed broadening results from scattering of the incident ions holding their initial incident energy, the scattering angle,  $\delta$ , can be estimated from,

$$\delta\lambda_{Ar^+} \approx 2\lambda_0\gamma\beta \sin(\alpha + \delta) \approx 0.4,$$

where  $\alpha$  is the half-conical angle of the detection system. The resultant deflection angle is  $\sim 8^\circ$ . According to the estimation in Section 1.3.4, the incident ions change their initial direction by  $1^\circ$  through image interaction, which is smaller than the above

estimation. This indicate that the specular reflection is not a dominant process, but a considerable fraction of the incident ions penetrate into the solid, collide with the atoms violently and then change their initial direction considerably.

### 3.2.2 Light from HCI with multiple electrons transferred

As is seen at wavelengths 324 nm, 340 nm and 343 nm in Fig. 3.3(A), the line intensities for  $Q_{in} = 6$  spectrum are about twenty times as large as those for  $Q_{in} = 7$  spectrum. As was discussed in Section 3.1, these lines in  $Q_{in} = 7$  spectrum shows that incident  $\text{Ar}^{7+}$  ions capture multiple electrons and de-excite keeping one electron in  $n_u = 7$  states. The fact that wavelengths of these lines in  $Q_{in} = 6$  and 7 spectra are the same as each other within the experimental resolution shows that one of the captured electrons fills the lowest core hole of the  $\text{Ar}^{7+}$  core at the moment of the subsequent Rydberg transitions. This is also confirmed by  $\Delta n = 1$  transitions with  $n_u = 8$  in  $Q_{in} = 7$  spectrum (see spectral lines around 524 nm and 528 nm in Appendix C).

### 3.2.3 Light from HCI with a High Rydberg Electron

Lines other than those mentioned in Sections 3.2.1 and 3.2.2 are found to result from transitions of Ar ions which have been transferred one electron in the capillary. Figures 3.4(A-C) show  $Q_{in} = 8$  spectra around  $\Delta n = 1$  transitions with  $n_u = 8, 9$  and 10, respectively. Figures 3.5(A-D) show  $Q_{in} = 7$  spectra around  $\Delta n = 1$  transitions with  $n_u = 7, 8, 9$  and 10, respectively. Wavelength regions in Figs. 3.4 and Figs. 3.5 are so selected as to include the whole lines from the transmitted argon ions taking into account of the discussion in the previous sections. In the figures, spectroscopic notations like *VII* are used to specify the lines attributable to transitions from argon ions. Observed wavelengths for  $\text{Ar}^{8+}$  and  $\text{Ar}^{7+}$  incident ions are listed in the first column in Table 3.2 (page 59) and in Table 3.3 (page 72), respectively. The wavelengths were determined by fitting each peak with a Gaussian function. The Ar VIII (sodium-like) lines with  $n_u = 8, 9, 10$  in Figs. 3.4 have similar structures to each other, *i.e.*, three lines are observed and intensities decrease with decreasing wavelength. On the other hand, the Ar VII (magnesium-like) lines in Figs. 3.5 have more complex structures, *i.e.*, (1) lines with  $n_u = 10$  (D) seem to be similar to the Ar VIII lines, (2) lines with  $n_u = 9$  (C) also distribute in a similar manner (*i.e.*, line intensities decrease with decreasing wavelength), although eight separable lines are observed, (3) some weaker lines with  $n_u = 8, 7$  (B,A) have longer wavelengths than the strongest line.



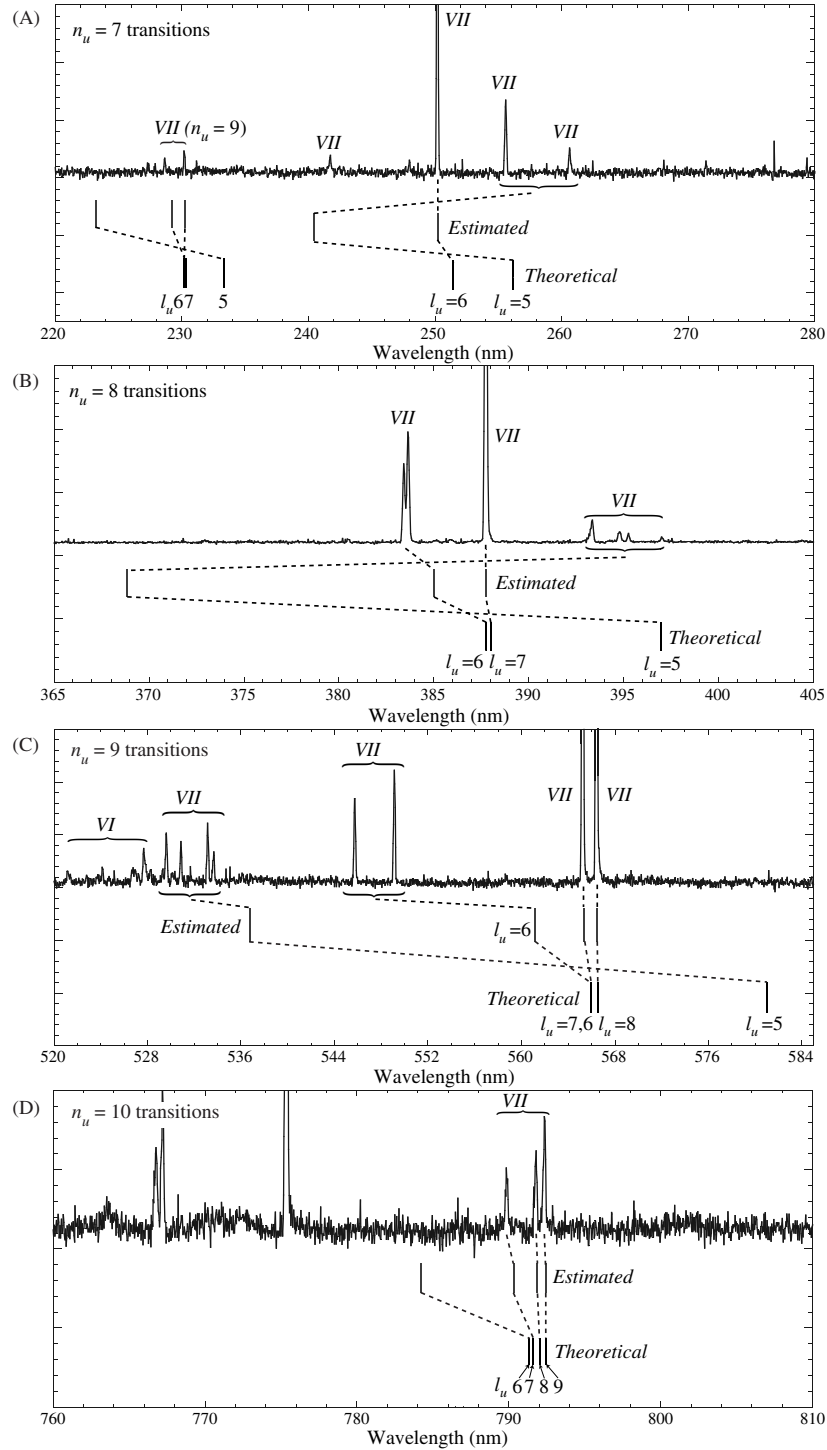


Figure 3.5:  $Q_{in} = 7$  spectra for  $n_u = 7$  (A), 8 (B), 9 (C) and 10 (D) transitions. Bars marked by *Theoretical* and *Estimated* show wavelengths calculated by the polarization formula with theoretical parameters and those evaluated experimentally, respectively.

### 3.2.4 Core Polarization Method

The spectral structures shown in Figs. 3.4 and 3.5 indicate that the upper states involved in the  $\Delta n = 1$  transitions have different angular momentum quantum numbers,  $\ell_u$ . Two effects were expected to change the hydrogen-like energy levels into  $\ell_u$ -dependent energy levels. One is the penetration of the Rydberg electron into the electron cloud of the core, which increases an effective charge felt by the Rydberg electron. The penetration effect is large for small  $\ell_u$  orbitals, and becomes smaller as  $\ell_u$  is larger because of the higher centrifugal barrier,  $\ell_u(\ell_u + 1)/2r^2$ . The quantum defect method [77] treats the penetration effect. The other effect is the core polarization [78, 77, 79]. The core electrons are redistributed due to electrostatic interaction between the Rydberg electron and the electron cloud in the core, which makes the effective potential produced by the core different from the hydrogen-like potential. The core polarization effect is important even for large  $\ell_u$  orbitals because distance between the Rydberg electron and the core is finite.

As was seen in Section 3.1, observed wavelengths agree with those calculated by the hydrogen-like formula within 1 %. Further it is known that  $\Delta\ell = \ell_u - \ell_l = 1$  transition with  $n_u = 9$ ,  $\ell_u = 1$  and  $Q_{in} = 8$  has a wavelength of  $\sim 316$  nm [80] which deviates from the hydrogen-like wavelength (434 nm) by  $\sim 27$  %. This indicates that the involved  $\ell_u$  in Figs. 3.4 and 3.5 are large. Hence we adopted a formula to estimate transition wavelengths taking into account of the core polarization effect, *i.e.*,

$$E_{n,\ell}^{pol} = -\frac{Ry Q_{in}^2}{n^2} - \alpha_d Ry \langle n, \ell | \frac{1}{r^4} | n, \ell \rangle - (\alpha_q - 6\beta) Ry \langle n, \ell | \frac{1}{r^6} | n, \ell \rangle, \quad (3.4)$$

$$= -\frac{Ry Q_{in}^2}{n^2} - A(Q_{in}) p(n, \ell) (1 + k(Q_{in}) q(n, \ell)), \quad (3.5)$$

where quantities with brackets represent expectation values calculated with hydrogen-like wave functions [81],  $\alpha_d$  and  $\alpha_q$  are the dipole and quadrupole polarizabilities, respectively and  $\beta$  is the non-adiabatic correction to the dipole polarizability (detailed description and definitions of the quantities in the formulae are given in Appendix A).

### Ar VIII Lines

The values of  $\alpha_d$  and  $\alpha_q$  for Ne-like cores have been evaluated from observed transition wavelengths of the Na-like ions ranging from vacuum-ultraviolet to visible light. Using polarizability values evaluated from Na I [82, 83], Mg II [84], Al III [85], Si IV [86] and P V [87] spectra, and the dipole polarizability of the neon atom [78], Edlén proposed extrapolation formulae for  $A(Q_{in})$  and  $k(Q_{in})$  in Eq. 3.5 which are adoptable for any Ne-like cores [88], *i.e.*,

$$A(Q_{in})(Z - 10)^{-4} = 9(Z - 0.4)^{-4} + 324(Z - 2.4)^{-4} + 566(Z - s)^{-4},$$

$$\begin{aligned}
s &= 5.6806 + 1.798(Z - s)^{-1}, \\
\frac{k(Q_{in})}{\sqrt{A(Q_{in})}} &= 0.3568(Z - 10) + 3.8359 - 10.5(Z - 8)^{-1}, \quad (3.6)
\end{aligned}$$

where  $Z$  represents the nuclear charge under study ( $Q_{in} + 10 = Z$ ). It is known that observed wavelengths of  $4f(\ell = 3) - 5g(\ell = 4)$  transitions for Na-like ions with  $Z = 26 - 35$ , *i.e.*, Fe XVI, Ni XVIII ..., and Br XXV, can be predicted within  $\lesssim 0.05\%$  with polarizabilities calculated by the extrapolation formulae [89]. We adopted polarizabilities of the  $\text{Ar}^{8+}$  core estimated from Eqs. 3.6, *i.e.*,  $\alpha_d = 0.0314$  a.u. (unit in  $a_0^3$ ,  $a_0$ : Bohr radius) and  $\alpha_q = 0.0313$  a.u. ( $a_0^5$ ) (relations between  $\alpha_d$ ,  $\alpha_q$  and  $A(Q_{in})$ ,  $k(Q_{in})$  are given in Appendix A). It is noted that  $\beta$  parameter was neglected to evaluate the extrapolation formulae from the experimental values. Hence we also neglected it.

The transition wavelengths for the Ar VIII lines were estimated using these polarizability values. The bars marked by *Polarization* in Figs 3.4 show the calculated wavelength positions. The observed and calculated wavelengths are summarized in the first and second columns in Table 3.2, respectively. The calculated wavelengths show good agreement with observed ones, *i.e.*, within the error of 0.02 %. The identified spectral lines are connected with the calculated lines by the dotted lines in Figs. 3.4.

*Table 3.2: Wavelengths observed in the high-resolution experiment with 2.0 keV/amu  $\text{Ar}^{8+}$  incidence. The first and second columns show wavelengths observed and calculated by the polarization formula, respectively. The last column shows the identified  $(n_u, \ell_u)$  in the  $\Delta n = \Delta \ell = 1$  transition.*

Wavelength(nm)	<i>Polarization</i>	$(n_u, \ell_u)$
294.78	294.83	(8,4)
297.34	297.35	(8,5)
297.63	297.61	(8,6)
297.63	297.66	(8,7)
429.90	429.97	(9,4)
433.65	433.70	(9,5)
434.12	434.08	(9,6)
434.12	434.16	(9,7)
434.12	434.18	(9,8)
600.92	601.07	(10,4)
606.23	606.32	(10,5)
606.93	606.85	(10,6)
606.93	606.96	(10,7)
606.93	607.00	(10,8)
606.93	607.01	(10,9)

The results show that (1) upper angular momentum quantum numbers,  $\ell_u$ , involved in the transitions are  $4 \leq \ell_u \leq n_u - 1$  for  $8 \leq n_u \leq 10$ , (2) higher  $\ell_u$  states are almost degenerated due to small polarizabilities of the  $\text{Ar}^{8+}$  core and, as a result, lines from such states appear as one peak with the present spectrometer resolution, *i.e.*, the strongest line in each spectrum in Figs. 3.4 includes several transitions with different  $\ell_u$  ( $\ell_u = 6, 7$  for  $n_u = 8$ ,  $\ell_u = 6 - 8$  for  $n_u = 9$  and  $\ell_u = 6 - 9$  for  $n_u = 10$ ) and (3) line intensity decreases with decreasing  $\ell_u$  for the same  $n_u$  transitions, which is primarily due to smaller branching ratios of  $\Delta n = 1$  transitions from smaller  $\ell_u$  states where  $\Delta n > 1$  transitions are dominant.

## Ar VII Lines

The polarizabilities for Na-like core ions have not been studied so much experimentally, and only theoretical values calculated by Curtis [90, 91] are available, *i.e.*,  $\alpha_d = 1.38$ ,  $\alpha_q = 0.648$  and  $\beta = 1.05$ . In addition to the theoretical values, we estimated polarization parameters from the observed wavelengths in Figs. 3.5. Two wavelengths are enough to determine the values (see Eq. 3.5). As was seen in Ar VIII lines, the strongest line in each  $n_u$  transition can be identified as from  $\ell_u = n_u - 1$  states, and smaller  $n_u$  transitions are expected to largely reflect the polarization effect because of the shorter distance from the core. Hence we selected  $\ell_u = n_u - 1$  transition wavelengths with  $n_u = 7$  and 8 ( $\lambda = 250.19$  nm and 387.74 nm) to determine the polarizabilities. The resultant polarizabilities are  $\alpha_d = 1.2$  and  $\alpha_q - 6\beta = 4.3$ . The dipole polarizability agrees well with the theoretical value of 1.38, however  $\alpha_q - 6\beta$  parameter is quite different from the theoretical value of  $-5.7$ .

Using the theoretical and estimated polarization parameters, the transition wavelengths of Ar VII lines were evaluated. The bars marked by *Theoretical* and *Estimated* in Figs. 3.5 show the results calculated with the theoretically predicted parameters and those estimated from observed wavelengths, respectively. The dotted lines in Figs. 3.5 connect the observed spectral lines and corresponding predicted lines calculated by two ways described above (observed lines will be identified in Section 3.2.5). For  $n_u = 7$  and 8 transitions, as is seen in Figs. 3.5(A) and (B), the ‘‘Theoretical’’ line positions agree with those observed within  $\sim 1$  % and further reproduce the relative line positions with respect to  $\ell_u$  correctly. The ‘‘Estimated’’ and observed line positions with  $\ell_u = 5$  relative to those with  $\ell_u = n_u - 1$  are on the opposite side to each other. Only the line position with  $n_u = 8$  and  $\ell_u = 6$  is reproduced (except transitions with  $\ell_u = n_u - 1$  for  $n_u = 7, 8$  which were used in the evaluation of the polarization parameters). On the other hand for  $n_u = 9$  and 10 transitions, as is seen in Figs. 3.5(C) and (D), the ‘‘Estimated’’ line positions reproduce the observed positions within  $\sim 2.5$  % and the relative line position with respect to  $\ell_u$ . The ‘‘Theoretical’’ line positions also agree with observed line positions for  $n_u = 10$  transitions within 0.1 %, however the relative

line position for  $n_u = 9$  and  $\ell_u = 5$  transition is incorrect.

As far as the Ar VII lines were analyzed with two polarization parameters ( $\alpha_d$  and  $\alpha_q - 6\beta$ ), we could not explain all of the observed spectral lines consistently. However it is noted that, unlike the Ar VIII lines where  $\ell_u \geq 6$  transitions were not resolved, it was expected that each  $\ell_u$  transition in the Ar VII lines can be resolved with our spectrometer, which is essentially important to discuss the initial population on each  $\ell$  state in Chapter 4. In the following sections, the Ar VII lines will be analyzed in more detail.

### 3.2.5 Multi-Configuration Hartree-Fock Method

#### Configuration Interaction

As was seen above, the polarization formula predicts transition wavelengths very precisely ( $\lesssim 0.02\%$ ) for Ar VIII lines. That is not true for Ar VII lines and the identifications of  $\ell_u$  can not be made with confidence. The difference between Ar<sup>8+</sup> and Ar<sup>7+</sup> cores is that Ar<sup>8+</sup> core is much less polarized by the Rydberg electron than Ar<sup>7+</sup> core is, which is attributed to the fact that the energy difference between the ground state and the first excited state of the Ar<sup>8+</sup> core ( $1s^2 2s^2 2p^6 - 1s^2 2s^2 2p^5 3s^1$ , 252.1 eV [92]) is much larger than that of Ar<sup>7+</sup> core ( $1s^2 2s^2 2p^6 3s^1 - 1s^2 2s^2 2p^6 3p^1$ , 17.4 eV [92]). Such a small energy difference for Ar<sup>7+</sup> core makes the atomic system ( $3s^1 n\ell^1$ ) of the Ar<sup>6+</sup> ion more complex by the following reason.

According to  $Z$ -dependent perturbation theory [93, 94], the unperturbed wave function, which is a linear combination of the wave functions for degenerate configurations (see Appendix B),

$$\psi_0 = \sum_{j', \gamma'} c_{j', \gamma'} |(nj')\gamma'J\rangle \quad (3.7)$$

is mixed up with wave functions for other configurations,  $|\gamma_v J\rangle$ , due to electron-electron interactions  $\mathcal{V}$  where  $|\gamma_v J\rangle$  have the same  $J$  but different energy from  $E_0$ . The first order correction to  $|\psi_0\rangle$  can be written as,

$$\psi_1 = \sum_{j', \gamma'} c_{j', \gamma'} \sum_v \frac{|\gamma_v J\rangle \langle \gamma_v J | \mathcal{V} | (nj')\gamma'J \rangle}{E_0 - E_{\gamma_v J}}, \quad (3.8)$$

where  $E_{\gamma_v J} = \langle \gamma_v J | \mathcal{H}_0 | \gamma_v J \rangle$  is the unperturbed energy. Equation 3.8 shows that  $|\psi_0\rangle$  is mixed up with  $|\gamma_v J\rangle$  more strongly as the energy difference between  $E_0$  and  $E_{\gamma_v J}$  is smaller.

Figure 3.6(A) shows the energy diagram for  $3sn\ell$ ,  $3pn'\ell'$  and  $3dn''\ell''$  configurations of Ar<sup>6+</sup> ion. The hatched area corresponds to the energy levels of  $3sn\ell$  configurations involved in the observed transitions. It is seen that the energy level for doubly excited  $3p5\ell$  configuration locates between those for  $3s9\ell$  and  $3s8\ell$  configurations. The maximum total angular momentum resulting from  $3p5\ell$  configuration is  $J = 6$ , *i.e.*,  $3sn\ell$

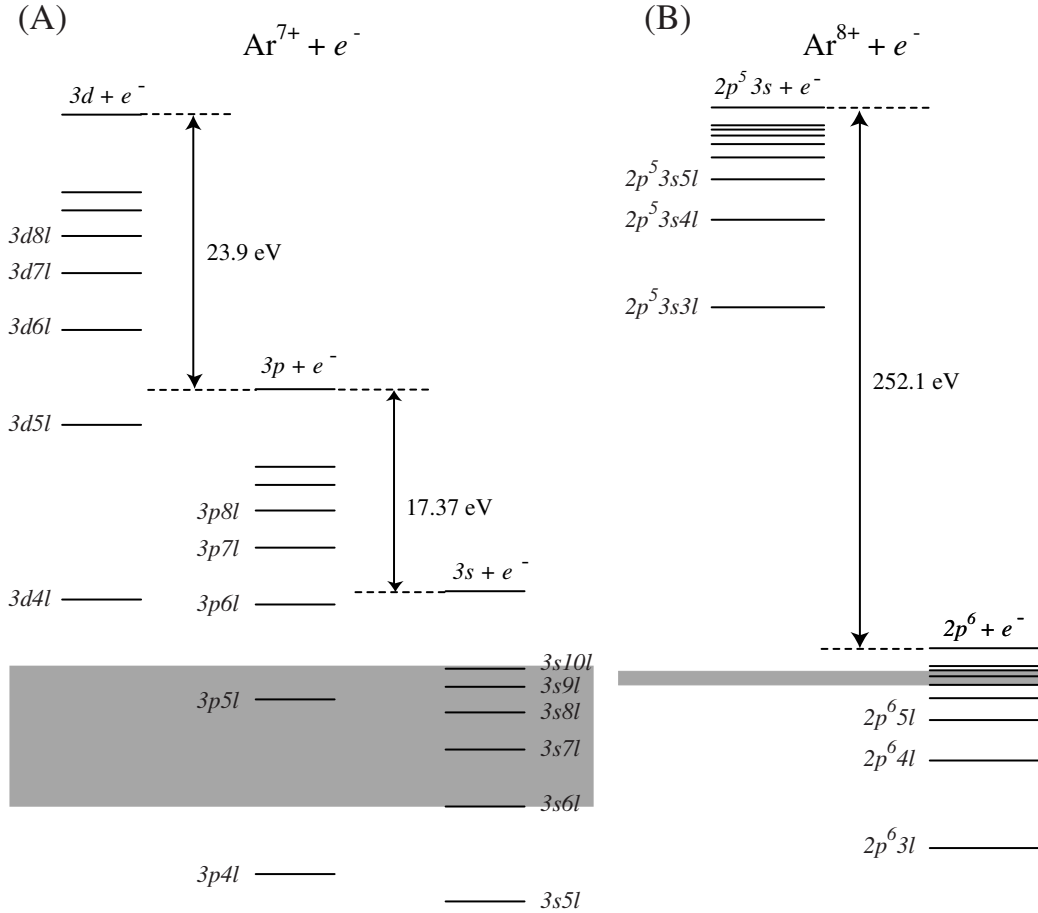


Figure 3.6: Comparisons of energy levels between singly and doubly excited  $\text{Ar}^{6+}$  (A) and  $\text{Ar}^{7+}$  (B) ions. The hatched area in each figure corresponds to energy levels to be populated. It is expected from the figures that due to a large energy difference in the  $\text{Ar}^{8+}$  core (252.1 eV in (B)), singly excited states of  $\text{Ar}^{7+}$  ions can be described better with a hydrogen-like wave function, however levels involved in the observed transitions in  $\text{Ar}^{6+}$  ions are perturbed more strongly by doubly excited states of  $3p5l$  .. levels, which is expected to be a reason why polarization formula is unsuitable for the prediction of the observed line positions.

( $n = 8, 9$ ) configurations with  $J \leq 6$  are expected to be influenced most strongly.

The energy diagram for  $2p^6 n l$  and  $2p^5 3s^1 n' l'$  configurations of the  $\text{Ar}^{7+}$  ion is also shown in Fig. 3.6(B). Due to the larger energy difference between  $2p^6$  and  $2p^5 3s$  states of the  $\text{Ar}^{8+}$  core (252.1 eV [92]) than that between  $3s - 3p$  states of the  $\text{Ar}^{7+}$  core (17.37 eV), energy levels for doubly excited  $2p^5 3s n l$  configurations are far above those of any singly excited  $2p^6 n l$  configurations by more than about 100 eV. This is considered as the major reason why transition wavelengths in the Ar VIII lines are predicted better than those in the Ar VII lines by the polarization formula in Section 3.2.4, *i.e.*, wave

functions of singly excited states are not mixed up so strongly with those of doubly excited states.

The Ar<sup>6+</sup> core in the ground state has a simple structure of  $3s^2$  ( $^1S$ ), which is similar to the Ar<sup>8+</sup> core. However because the energy difference between  $3s^2$  and  $3s3p\dots$  states are very small (*e.g.*,  $3s^2 - 3s^13p^1$   $^3P$ ;  $\sim 14$  eV [92]) and two active electrons are involved in the core, the Ar VI lines should be fairly complex and was not analyzed systematically. The Ar VI lines will be analyzed in a near future.

### Multi-Configuration Hartree-Fock Method

As was discussed in the previous section, states involved in the transitions are perturbed by other states which locate close in energy and have the same  $J$ . Instead of calculating higher order corrections in the  $Z$ -dependent perturbation theory, an *ab-initio* calculation based on the Multi-Configuration Hartree-Fock (MCHF) formalism is often employed [95, 96]. The following results were calculated with a computational code which is so-called Cowan code.

Figures 3.7(A), (B), (C) and (D) show theoretically synthesized spectra around  $\Delta n = 1$  transitions with  $n_u = 7$  of Ar<sup>6+</sup> ions for different size of the configuration space, *i.e.*,

- (case  $\mathcal{A}$ ):  $3sn\ell$  ( $n = 6, 7$ ),
- (case  $\mathcal{B}$ ):  $3sn\ell$  ( $n = 3 - 10$ ) +  $3pn\ell$  ( $n = 4 - 6$ ),
- (case  $\mathcal{C}$ ): (case  $\mathcal{B}$ ) +  $3\ell 3\ell'$  ( $\ell, \ell' \neq 0$ ) +  $3dn\ell$  ( $n = 4 - 5$ ),
- (case  $\mathcal{D}$ ): (case  $\mathcal{C}$ ) +  $3sn\ell$  ( $n = 11$ ) +  $3pn\ell$  ( $n = 7 - 11$ ),

respectively. The Cowan code calculates all possible dipole transitions included in the configuration space, *i.e.*, not only  $3sn_1\ell - 3sn'_1(\ell \pm 1)$  but also  $3pn_2\ell - 3pn'_2(\ell \pm 1)$  (or  $3pn\ell - 3sn\ell$  or  $3sn\ell - 3pn\ell$ ) transitions. If a synthetic spectrum is generated using all of these transitions, the resultant spectrum becomes very complex because wavelengths for  $3sn\ell - 3sn'(\ell \pm 1)$  and  $3pn\ell - 3pn'(\ell \pm 1)$  transitions are close to each other. After the MCHF calculations, transitions from doubly excited states were removed from the results in advance because incident ions are expected to be in the ground state. Using transition wavelengths and their  $gA_{n,\ell}^{n',\ell'}$  values calculated with the MCHF code, synthetic spectra were generated in the same manner as shown in Section 3.2 with a resolution  $2\sqrt{2\log 2}\Delta\lambda = 0.15$  nm (FWHM).

In the case  $\mathcal{A}$ , although the calculated spectrum in Fig. 3.7(A) does not reproduce the observed spectrum shown in Fig. 3.7(E), it is noted that a spectral line with the same  $\ell_u$  splits into two fine-structure components due to  $\ell \cdot s$  interaction. For example, the line with  $\ell_u = 5(h)$  splits into  $^3H_J - ^3G_{J-1}$  ( $J = 4, 5, 6$ ;  $\lambda \approx 248$  nm) transitions

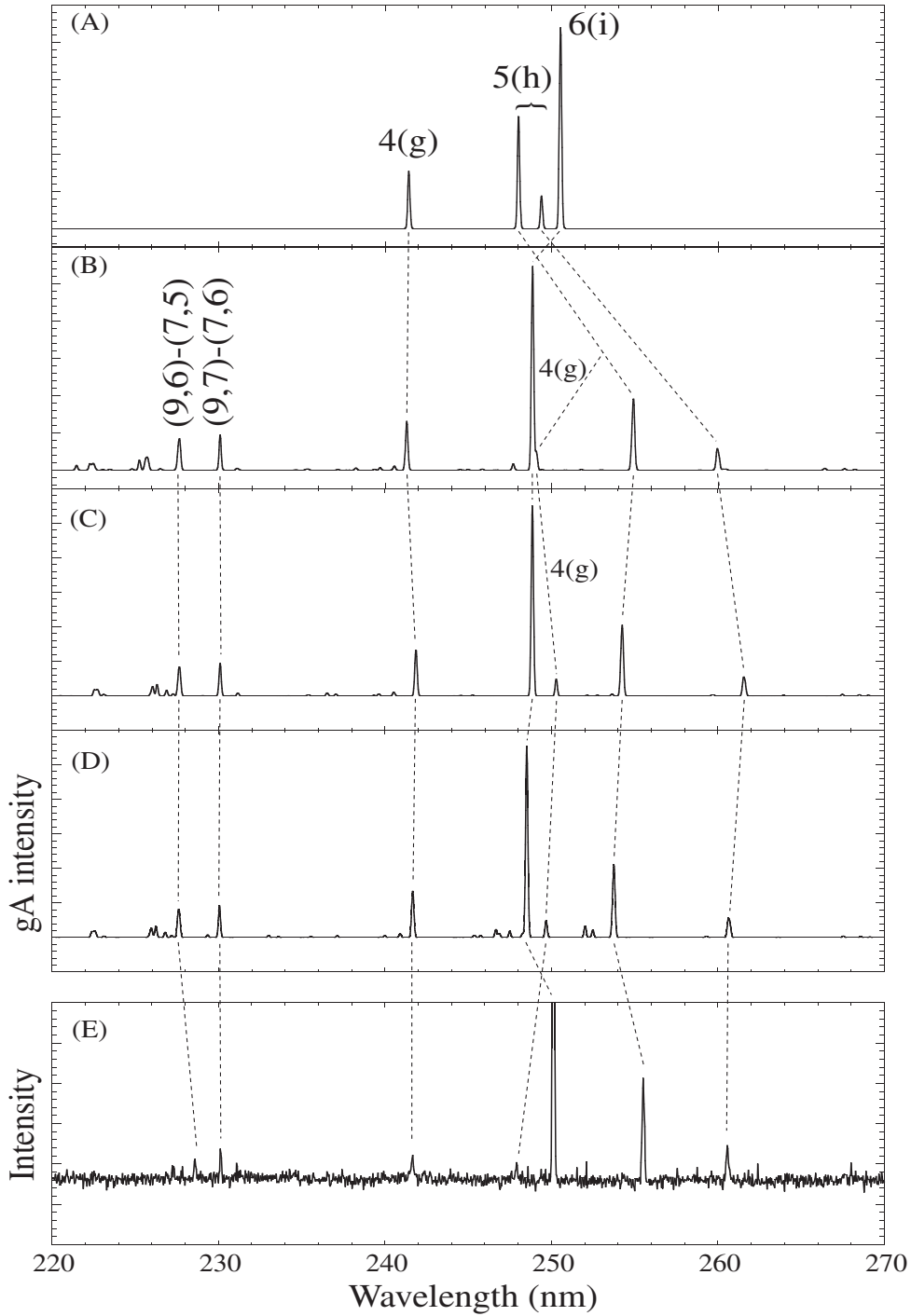


Figure 3.7: Results of the MCHF calculations around  $\Delta n = 1$  transitions with  $n_u = 7$  when included configuration spaces were varied. Numbers written at the side of lines show angular momentum quantum numbers,  $\ell_u$ , for upper states involved in transitions. Changes of line positions are chased by the dotted lines. As was expected in Fig. 3.6(A), the drastic change takes place when  $3pn\ell$  ( $n = 4 - 6$ ) configurations are taken into account in figure (B).

and  ${}^1H_5 - {}^1G_4$  ( $\lambda \approx 249.4$  nm) transition. Similarly, the line with  $\ell_u = 4(g)$  splits into  ${}^3G_J - {}^3F_{J-1}$  ( $J = 3, 4, 5; \lambda \approx 242$  nm) transitions and  ${}^1G_4 - {}^1F_3$  ( $\lambda \approx 248$  nm) transition which overlaps with the  ${}^3H_J - {}^3G_{J-1}$  transitions.

In the case  $\mathcal{B}$  where  $3pn\ell$  ( $n = 4 - 6$ ) configurations are taken into account, the resultant spectrum shown in Fig. 3.7(B) becomes very close to the observed one, *e.g.*,  $\ell_u = 5$  (*h*) transitions have longer wavelengths than  $\ell_u = 6$  transitions, and fine-structure splitting becomes larger than the case  $\mathcal{A}$ . Because  $3s9\ell$  configurations are taken into account,  $\Delta n = 2$  transitions with  $n_u = 9$  and  $\ell_u = 7, 6$  appear around 230 nm in Fig. 3.7(B) which are actually observed in Fig. 3.7(E).

In the case  $\mathcal{C}$ ,  $3dn\ell$  ( $n = 4 - 5$ ) and  $3\ell 3\ell'$  ( $\ell, \ell' \neq 0$ ) configurations were added to the case  $\mathcal{B}$ . Because energy levels for added configurations locate somewhat far away from the considered levels compared with  $3p5\ell$  configuration (see Fig. 3.6), only the transition with  $\ell_u = 4$   ${}^1G$  shifts slightly. The lines with very small intensities seen in the whole synthetic spectrum are due to  $3sn\ell - 3pn'\ell'$  transitions or  $\Delta n = 1$  and 2 transitions for smaller  $\ell_u$  with  $n_u = 7$  and 9, respectively.

In the case  $\mathcal{D}^*$ ,  $3pn\ell$  ( $n = 7 - 11$ ) configurations whose energy levels are  $\sim 20$  eV higher than the  $3s7\ell$  energy level, were added to the case  $\mathcal{C}$ . Line positions change very slightly ( $\lesssim 0.2$  %) from the case  $\mathcal{C}$ .

In the following, the MCHF result calculated for the configuration space within

$$3\ell 3\ell' + 3sn\ell \ (n = 4 - 11) + 3pn\ell \ (n = 4 - 6) + 3dn\ell \ (n = 4 - 5),$$

is used to compare with the observed wavelengths.

### Identification ( $\Delta n = 1$ )

The following four points are taken into account for identification of the observed lines; (1) not only predicted wavelengths, but also relative line position and intensity for each  $\ell_u$  transition are considered, (2) the number of fine-structure components changes depending upon  $\ell_u$ , (3) some lines are from sputtered Ni atoms and Ar ions, (4) lines from  $\text{Ar}^{5+}$  ions resulting from multiple electron transfer to  $\text{Ar}^{7+}$  ions, are also observed.

The middle spectra in Figs. 3.8, 3.9, 3.10 and 3.11 show  $Q_{in} = 7$  spectra around  $n_u = 10, 9, 8$  and 7 transitions, respectively, and the top spectra show  $Q_{in} = 6$  spectra to identify transitions corresponding to (3) and (4) stated above. The lines common to the  $Q_{in} = 6$  and  $Q_{in} = 7$  spectra are connected with the dotted lines. The bottom spectra show the synthetic spectra generated using the MCHF result. The lines in the synthetic spectrum and the identified lines in the  $Q_{in} = 7$  spectrum are connected by the solid lines. Wavelengths of the observed and calculated lines and their transitions are listed in Table 3.3.

---

\* To complete this calculation, it is necessary to change the limitation for the total number of the configurations in the original code.

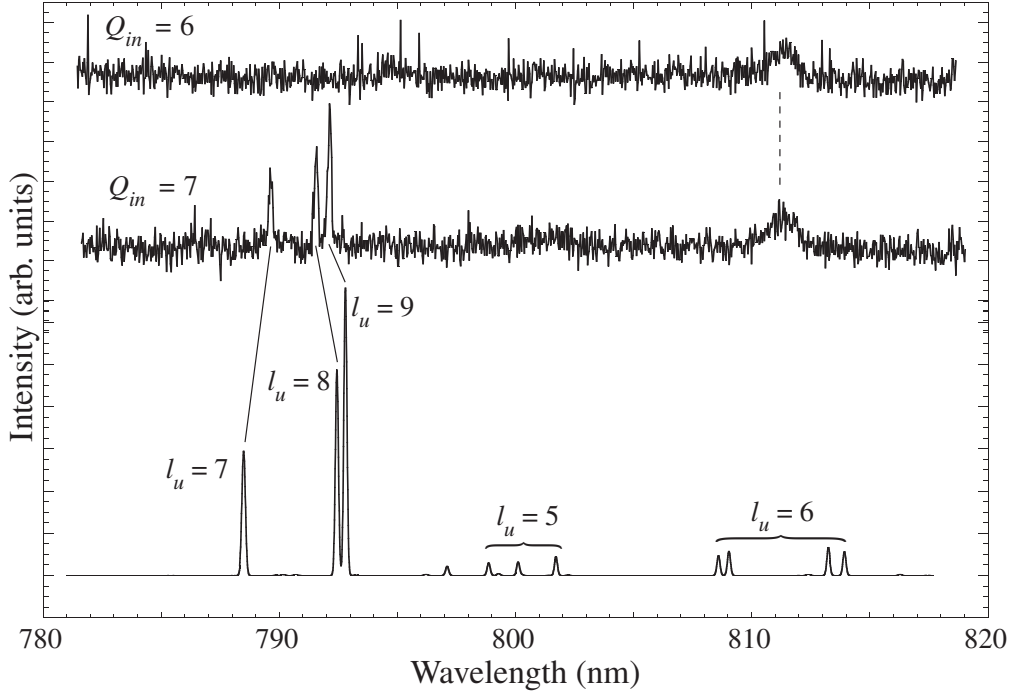


Figure 3.8:  $Q_{in} = 6$  (top),  $Q_{in} = 7$  (middle) and synthetic spectra (bottom) around  $\Delta n = 1$  transitions with  $n_u = 10$  of  $Ar^{6+}$  ions.

As an example, identification procedure for  $n_u = 9$  transitions in Fig. 3.9 is explained below. The line positions for  $\ell_u = 8$  and 7 transitions are well ( $\lesssim 0.2\%$ ) reproduced by the synthetic spectrum.  $\ell_u = 6$  transition splits into two fine-structure components, *i.e.*, the shorter wavelength component (538.6 nm) from  ${}^3I_7$  and  ${}^1I_6$  and the longer (542.6 nm) from  ${}^3I_{5,6}$  <sup>†</sup>. The predicted wavelengths agree with the observed wavelengths only with  $\sim 1.2\%$  precision, however the amount of splitting and its relative intensity are fairly well reproduced. Several weak lines around 530 nm seen in  $Q_{in} = 7$  spectrum were identified to originate from multiple electron transfer to  $Ar^{7+}$  ions (connected by the dotted lines), and four lines are left unidentified. Actually four lines for  $\ell_u = 5$  transitions are around 528 nm in the synthetic spectrum, which also reproduce the fine-structure splitting well.

### Identification ( $\Delta n = 2$ )

As was shown in Figs. 3.7(E) and 3.11, in addition to the  $\Delta n = 1$  transitions,  $\Delta n = 2$  transitions with  $n_u = 9$  were also observed. Figure 3.12(A) shows spectra around  $\Delta n = 2$  transitions with  $n_u = 10$ . The lines “a” and “b” were attributed to Ar III transition in Fig. 3.3(A) (page 53), however it is noted that wavelengths of these lines are slightly different from each other by  $\sim 0.1$  nm, which is shown in Fig. 3.12(B).

<sup>†</sup> The transition,  ${}^{2s+1}L_J - {}^{2s+1}L_{J-1}$ , is described as  ${}^{2s+1}L_J$  for simplicity.

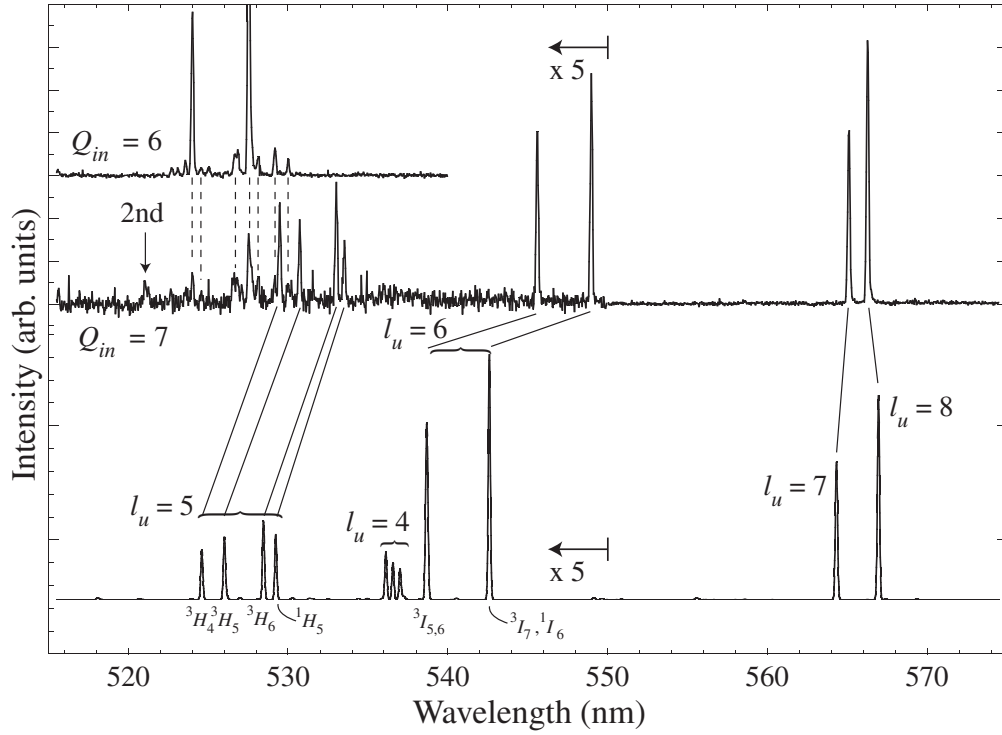


Figure 3.9:  $Q_{in} = 6$  (top),  $Q_{in} = 7$  (middle) and synthetic spectra (bottom) around  $\Delta n = 1$  transitions with  $n_u = 9$  of  $Ar^{6+}$  ions.

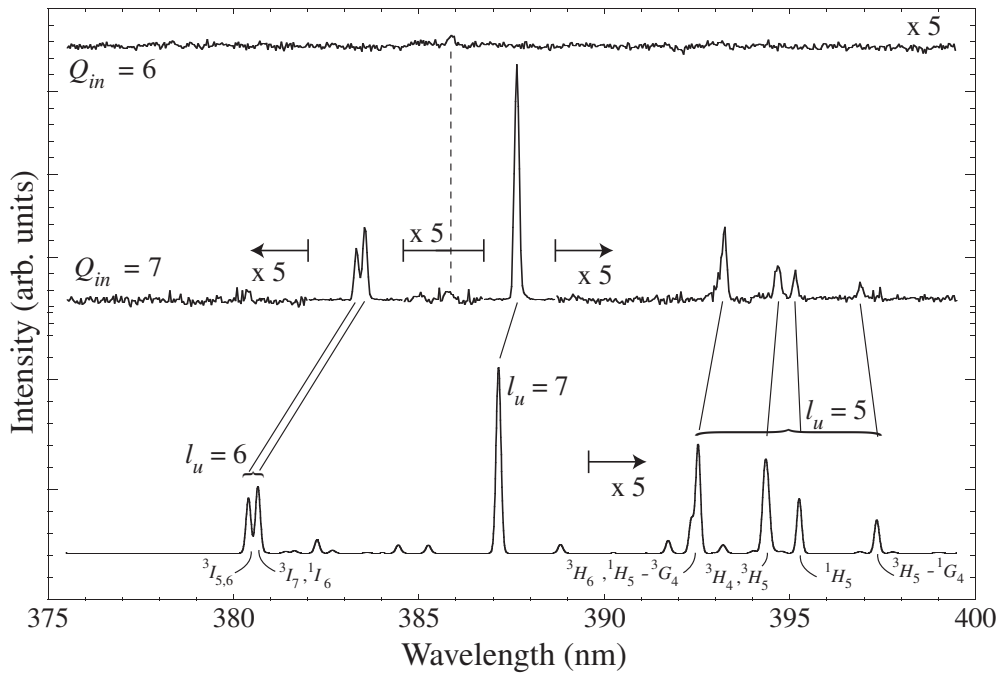


Figure 3.10:  $Q_{in} = 6$  (top),  $Q_{in} = 7$  (middle) and synthetic spectra (bottom) around  $\Delta n = 1$  transitions with  $n_u = 8$  of  $Ar^{6+}$  ions.

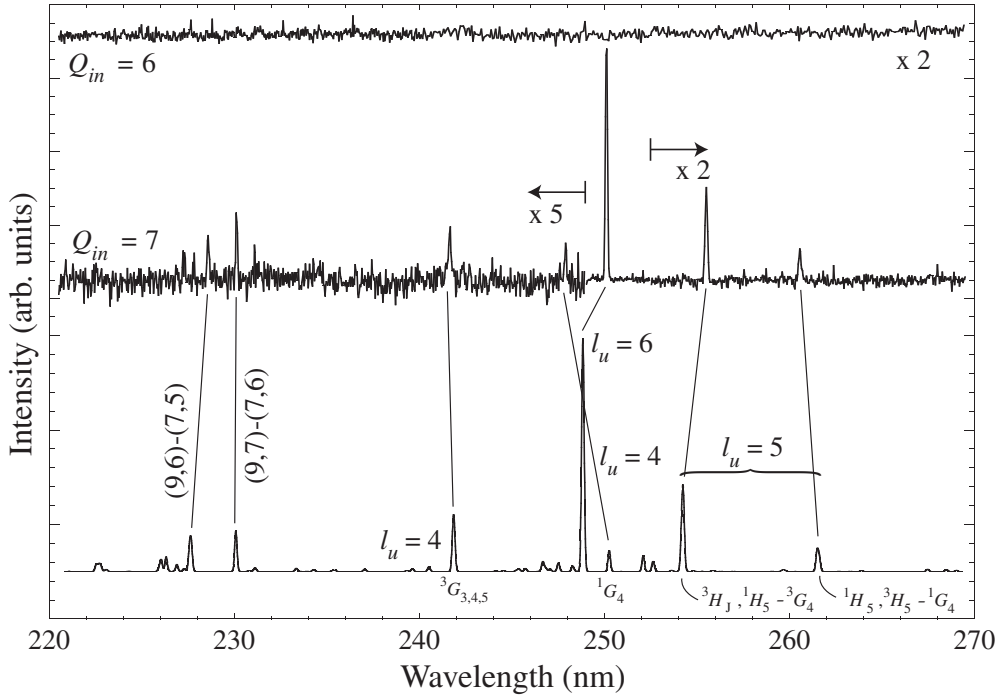


Figure 3.11:  $Q_{in} = 6$  (top),  $Q_{in} = 7$  (middle) and synthetic spectra (bottom) around  $\Delta n = 1$  transitions with  $n_u = 7$  of  $Ar^{6+}$  ions.

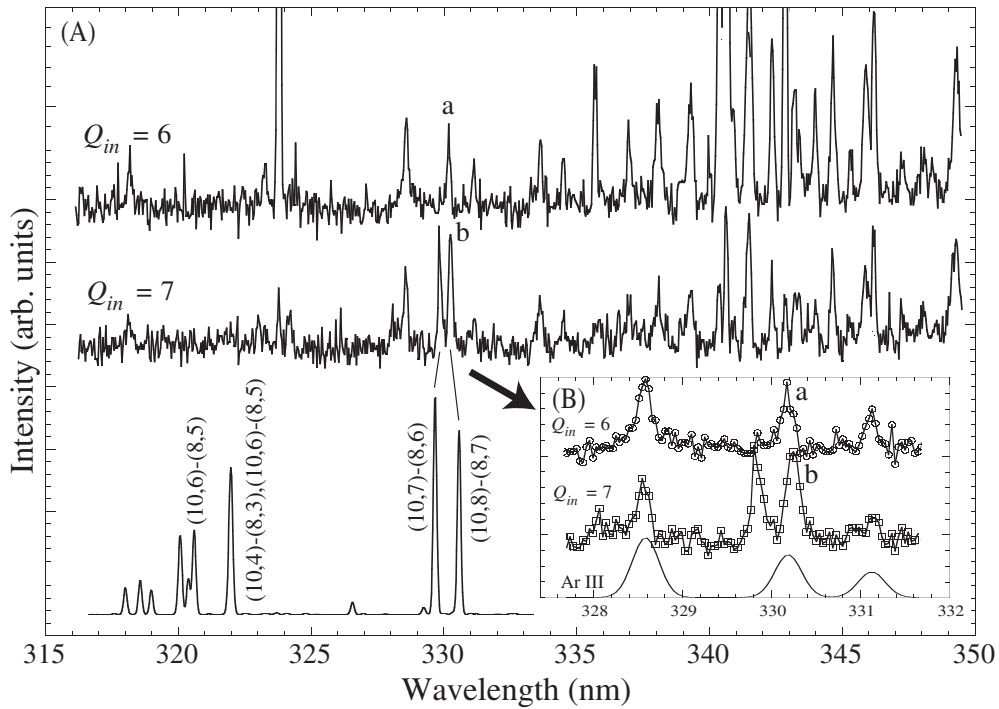


Figure 3.12:  $Q_{in} = 6$  (top),  $Q_{in} = 7$  (middle) and synthetic spectra (bottom) around  $\Delta n = 2$  transitions with  $n_u = 10$  of  $Ar^{6+}$  ions.

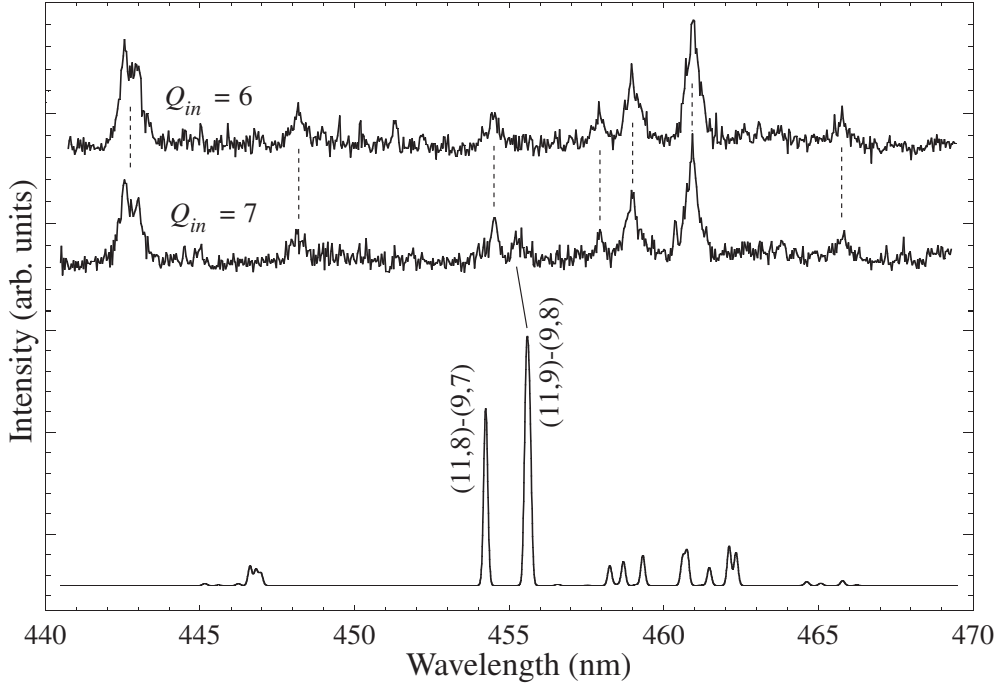


Figure 3.13:  $Q_{in} = 6$  (top),  $Q_{in} = 7$  (middle) and synthetic spectra (bottom) around  $\Delta n = 2$  transitions with  $n_u = 11$  of  $Ar^{6+}$  ions.

Hence the line “b” is identified as Ar III transition blended with  $\Delta n = 2$  transitions with  $n_u = 10$ .

Figure 3.13 shows spectra around  $\Delta n = 2$  transitions with  $n_u = 11$ . The line at 455 nm observed only in the  $Q_{in} = 7$  is identified as  $\ell_u = 9$  transition. The very low line intensity indicates that  $n_u = 11$  states are hardly populated.

### 3.3 Advantage of Capillary Technique

In production of the Rydberg ions, one of the most famous techniques to produce extensive charge states and excited states of the Rydberg ions is the beam-foil technique. The advantage of the capillary technique can be understood comparing with the beam-foil technique. Figure 3.14 shows a beam-foil spectrum [97] when 10 MeV  $Ne^{2+}$  ions were incident on a thin carbon foil. The wavelength range corresponds to  $\Delta n = 1$  transitions of  $Ne^{6+}$  ions with  $n_u = 7$  ( $\sim 2520 \text{ \AA}$ ). As is seen, the spectrum is much more complex than the capillary spectra discussed in the previous sections. The complex spectrum results from the fact that the high Rydberg ions were formed by the energetic collisions with the target atoms, *i.e.*,

(1) because there is only a loose selectivity for  $n$  of the Rydberg electron ( $\sim n^{-3}$  [98]), not only  $\Delta n = 1$  but also  $\Delta n = 2, 3, \dots$  transitions are observed in Fig. 3.14. This is in contrast to the sharp selectivity ( $n \approx Q_{in}$ ) in the capillary technique.

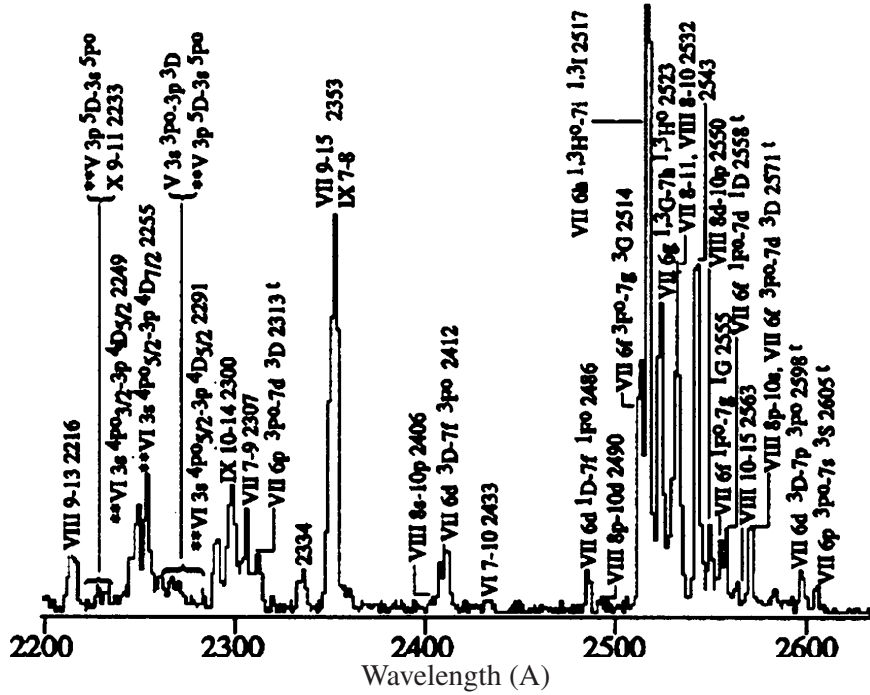


Figure 3.14: A Beam foil spectrum [97] observed with impinging 10 MeV  $\text{Ne}^{2+}$  ions to a thin carbon foil.

(2) because charge states of the exiting ions are distributed around the equilibrium charge determined by the incident energy, not only VII lines but also V, VI and VIII are observed in Fig. 3.14. In the capillary technique, observed lines always result from HCIs with lower charge states than the incident charge because Rydberg HCIs are formed through the electron transfer from the surface. Further charge states of the lines are easily identified comparing spectrum measured with two different incident charges (which is shown in Section 3.2.2).

(3) because of the multiple collisions with target atoms, not only singly but also multiply excited ions are formed (lines referred by asterisks in Fig. 3.14).

As was seen in Section 3.2.5, theoretical prediction by the *ab-initio* calculation is precise only with 1 %. Hence it is expected that simpler spectra contribute to more reliable identifications. In addition it is easy to perform a high-resolution measurement with the capillary technique due to slower velocity of the ions. For example, the Doppler broadening of 10 MeV neon ions is 0.9 nm at  $\lambda = 250$  nm, if the present set-up is used.

### 3.4 Summary of Spectroscopy

In summary, photons in the visible light range were observed for the first time by bombarding a Ni micro-capillary with 2.0 keV/amu  $\text{Ar}^{Q_{in}+}$  ( $6 \leq Q_{in} \leq 10$ ) ions. Intense lines from transmitted ions were identified as  $\Delta n = 1$  transitions whose principal quantum numbers for upper states are  $Q_{in} \lesssim n_u \leq Q_{in} + 3$  for all incident charges. Observations of lines common to different incident charges revealed that several electrons were actually transferred in the capillary.

High-resolution measurements revealed that the intense lines split into several components, which were attributed to  $\Delta n = 1$  transitions with different angular momentum quantum numbers  $\ell_u$  (or total angular momentum quantum numbers  $J_u$ ) for upper states.

In the case of the  $\text{Ar}^{8+}$  incident ions, the core is very "hard" and the wavelengths calculated with the polarization formula agree with those observed within 0.02 %. It was found that the observed Ar VIII lines consisted of  $\Delta \ell = 1$  transitions with  $4 \leq \ell_u \leq n_u - 1$ . However transitions with  $\ell_u \geq 6$  were not resolved with the present set-up due to small polarizabilities of the core.

In the case of  $\text{Ar}^{7+}$  incident ions, the polarization formula did not explain all of the observed Ar VII lines consistently, which was attributed to a very "soft"  $\text{Ar}^{7+}$  core. Instead, it was necessary to employ the *ab-initio* calculation based on the MCHF method in which  $3sn\ell$ ,  $3pn'l'$  and  $3dn''\ell''$  configurations were taken into account. It was found that the observed Ar VII lines consisted of  $\Delta \ell = 1$  transitions with  $4 \lesssim \ell_u \leq n_u - 1$ . Although the calculated and observed wavelengths agreed with each other only within 1 %, which was not so good as the  $\text{Ar}^{8+}$  case, the identification was made reasonably comparing the Ar VII and Ar VI lines, and taking into account of the fine-structure splitting. The fact that transitions with different  $\ell_u$  are easily resolved, is very important to extract the initial state distribution from cascade calculations to be discussed in the next chapter.

Table 3.3: Wavelengths observed in the high-resolution experiment with 2.0 keV/amu  $Ar^{7+}$  incidence. Precisions of the wavelengths are  $\sim 0.1$  nm. The first and second columns show wavelengths observed and those calculated with the MCHF code.  $3l3l' + 3snl (n = 4 - 11) + 3pnl (n = 4 - 6) + 3dnl (n = 4 - 5)$  configurations were taken into account in the calculation. The last column shows identified  $(n_u, \ell_u)$  in the  $\Delta n = \Delta \ell = 1$  transitions.

Wavelength (nm)	MCHF	$(n_u, \ell_u)$ transition
241.72	241.83-241.90	$(7, 4) {}^3G_{3,4,5} - {}^3F_{2,3,4}$
247.98	250.27	$(7, 4) {}^1G_4 - {}^1F_3$
250.19	248.82-248.87	$(7, 6) {}^{1,3}I_J - {}^{1,3}H_{J-1}$
255.59	254.17-254.30	$(7, 5) {}^3H_{4,5,6} - {}^3G_{3,4,5}, {}^1H_5 - {}^3G_4$
260.64	261.50-261.61	$(7, 5) {}^1H_5 - {}^1G_4, {}^3H_5 - {}^1G_4$
383.42	380.40-380.42	$(8, 6) {}^3I_{6,5} - {}^3H_{5,4}$
383.65	380.66-380.67	$(8, 6) {}^3I_7 - {}^3H_6, {}^1I_6 - {}^1H_5$
387.74	387.14-387.17	$(8, 7) {}^{1,3}K_J - {}^{1,3}I_{J-1}$
393.32	392.36-392.54	$(8, 5) {}^1H_5 - {}^3G_4, {}^3H_6 - {}^3G_5$
394.78	394.33-394.42	$(8, 5) {}^3H_{4,5} - {}^3G_{3,4}$
395.25	395.26	$(8, 5) {}^1H_5 - {}^1G_4$
397.02	397.36	$(8, 5) {}^3H_5 - {}^1G_4$
529.62	524.60	$(9, 5) {}^3H_4 - {}^3G_3$
530.87	526.01	$(9, 5) {}^3H_5 - {}^3G_4$
533.16	528.46	$(9, 5) {}^3H_6 - {}^3G_5$
533.66	529.23	$(9, 5) {}^1H_5 - {}^1G_4$
545.74	538.65-538.71	$(9, 6) {}^3I_{5,6} - {}^3H_{4,5}$
549.13	542.59-542.60	$(9, 6) {}^1I_6 - {}^1H_5, {}^3I_7 - {}^3H_6$
565.25	564.30-564.35	$(9, 7) {}^{1,3}K_J - {}^{1,3}I_{J-1}$
566.43	566.94-566.97	$(9, 8) {}^{1,3}L_J - {}^{1,3}K_{J-1}$
789.86	788.44-788.54	$(10, 7) {}^{1,3}K_J - {}^{1,3}I_{J-1}$
791.77	792.44	$(10, 8) {}^{1,3}L_J - {}^{1,3}K_{J-1}$
792.35	792.80	$(10, 9) {}^{1,3}M_J - {}^{1,3}L_{J-1}$

# Chapter 4

## Initial Population

In the previous chapter, we mainly focused on the spectroscopic aspects of the HCI-capillary interaction. Many lines were identified as transitions from ions which have captured one or several electron(s) in their high-Rydberg states. In this chapter, we will focus on the initial  $(n, \ell)$  distribution of the transferred electron, which will reveal the electron transfer mechanism in HCI-surface interaction.

### 4.1 Rate Equation

We first explain how to relate the observed line intensities with the initial populations under our experimental set-up. Figure 4.1 shows a simplified sketch of the experiment. An excited ion is produced at the exit of the capillary ( $x = 0$ ). Since the entrance slit of the spectrometer was located at  $x$  downstream of the capillary, it takes a finite time

$$t = \frac{x}{v_{ion}}, \quad (4.1)$$

for the ion to reach the observed region ( $v_{ion}$  is the ion velocity).  $x$  is varied by moving the capillary along the beam direction. Because the mirror system focuses the beam trajectory onto the slit with one to one imaging (see Section 2.3.3), the slit width,  $\Delta w$ , is related to the time window,  $\Delta t$ , as

$$\Delta w = \Delta x = v_{ion} \Delta t. \quad (4.2)$$

This means that the number of photons detected is proportional to the number of transitions in the time window between  $t$  and  $t + \Delta t$ . For example, the slit width of 0.1 mm corresponds to the time window of 0.16 ns for 2.0 keV/amu ( $v = 6.2 \times 10^5$  m/sec) ions.

The number of the transitions in the time window can be evaluated solving the rate

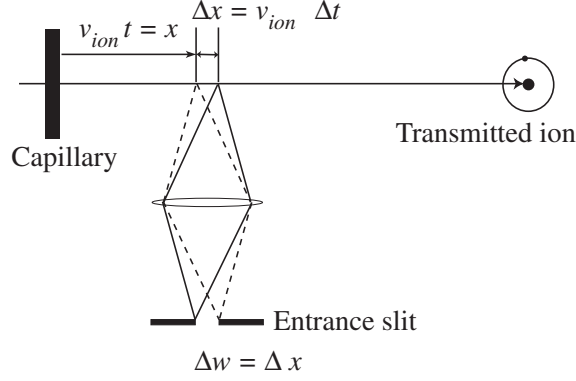


Figure 4.1: A simplified sketch of the experiment

equation for each  $(n, \ell)$  state,

$$\frac{dN_{n,\ell}(t)}{dt} = -\frac{1}{T_{n,\ell}}N_{n,\ell}(t) + f(t), \quad (4.3)$$

$$\frac{1}{T_{n,\ell}} = \sum_{n' < n} A_{n,\ell}^{n',\ell \pm 1}, \quad (4.4)$$

$$f(t) = \sum_{n' > n} A_{n',\ell \pm 1}^{n,\ell} N_{n',\ell \pm 1}(t), \quad (4.5)$$

where  $N_{n,\ell}(t)$  and  $A_{n,\ell}^{n',\ell'}$  are the population of the  $(n, \ell)$  state at a time  $t = x/v_{ion}$ , and the transition rate from  $(n, \ell)$  to  $(n', \ell')$  states, respectively. In Eq. 4.3, the first term in the right side shows de-population of the  $(n, \ell)$  state with its lifetime of  $T_{n,\ell}$ , and the second term shows cascade re-population of the  $(n, \ell)$  state from upper states. Integrating  $\exp(t'/T_{n,\ell}) f(t')$  from  $t' = 0$  to  $t' = t$ ,  $N_{n,\ell}(t)$  can be written using the initial population,  $N_{n,\ell}(0)$ , as

$$N_{n,\ell}(t) = N_{n,\ell}(0)e^{-\frac{t}{T_{n,\ell}}} + e^{-\frac{t}{T_{n,\ell}}} \int_0^t e^{\frac{t'}{T_{n,\ell}}} f(t') dt'. \quad (4.6)$$

The number of photons,  $I_{n,\ell}^{n_d,\ell_d}$ , corresponding to  $(n, \ell) - (n_d, \ell_d)$  transition is proportional to

$$I_{n,\ell}^{n_d,\ell_d} = \int_t^{t+\Delta t} A_{n,\ell}^{n_d,\ell_d} N_{n,\ell}(t') dt', \quad (4.7)$$

$$= T_{n,\ell} A_{n,\ell}^{n_d,\ell_d} N_{n,\ell}(0) e^{-\frac{t}{T_{n,\ell}}} \left( 1 - e^{-\frac{\Delta t}{T_{n,\ell}}} \right) + g(t, \Delta t), \quad (4.8)$$

where  $g(t, \Delta t)$  shows a contribution from cascade re-population. When  $t \ll T_{n,\ell}$ ,  $\Delta t \ll T_{n,\ell}$  and  $g(t, \Delta t) \approx 0$  are satisfied, Eq. 4.8 is reduced to a simple formula,

$$I_{n,\ell}^{n_d,\ell_d} \approx N_{n,\ell}(0) A_{n,\ell}^{n_d,\ell_d} \Delta t. \quad (4.9)$$

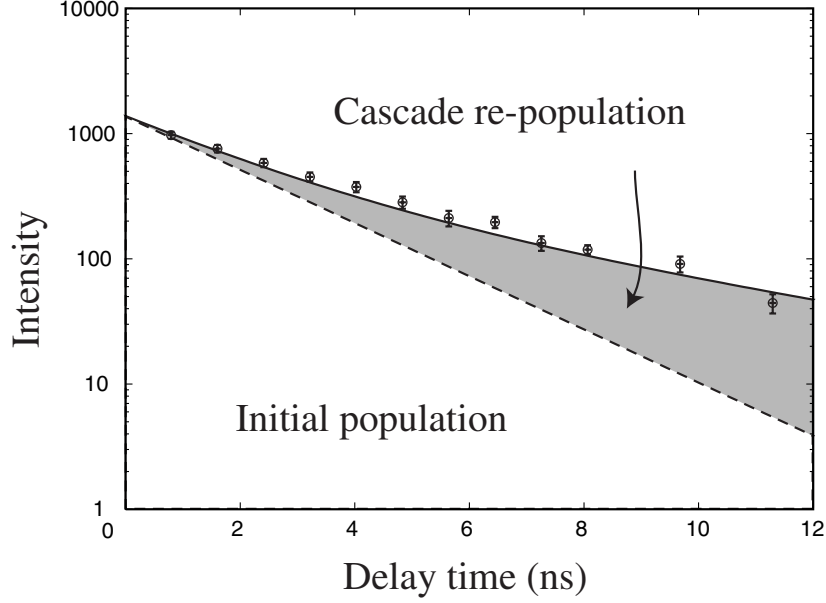


Figure 4.2: The observed line intensities (circles) for the transition with  $n_u = 9$  and  $\ell_u = 8$  of  $\text{Ar}^{6+}$  ions. The observed intensities are larger than those calculated assuming no cascading re-population.

If each  $(n, \ell)$  state is assumed to have a population proportional to its statistical weight,  $g = 2\ell + 1$ , (note that  $(n, \ell)$  state is  $2\ell + 1$  fold degenerate), the line intensity is proportional to  $gA_{n,\ell}^{n_d,\ell_d}$  ( $\Delta t$  is common to any transitions). This is one of the reasons why the synthetic  $gA$ -proportional spectra were used to compare with the observed spectra in Chapter 3. The measurements in Chapter 3 were performed at  $t \approx 0.8$  ns, and lifetimes of the states involved in the transitions is 1 – 5 ns, *i.e.*, the synthetic spectra do not necessarily reproduce the observed spectra.

Open circles in Fig. 4.2 show the measured line intensities for  $\Delta n = 1$  transition with  $n_u = 9$  and  $\ell_u = 8$  of the  $\text{Ar}^{6+}$  ion. The dashed line shows the calculated line intensities without cascade re-population. It is obvious that the observed intensities decrease slower than the calculated ones, which shows that the  $(n, \ell) = (9, 8)$  state is re-populated by cascading from upper states which have longer lifetimes than the  $(9, 8)$  state, *i.e.*, the grayed area in the figure corresponds to the effect of the cascade re-population.

#### 4.1.1 Transition Rates and Lifetimes

Transition rates and lifetimes of the states involved in the observed transitions are necessary for the evaluation of the initial populations from the observed line intensities using Eqs. 4.6 and 4.7. As was seen in Chapter 3,  $2p^6n\ell^1$  configurations of  $\text{Ar}^{7+}$  ions are barely influenced by the configuration interaction. Hence transition rates and lifetimes

of  $2p^6n\ell$  states were calculated by the computational Hartree-Fock code. Calculated transition rates for  $8 \leq n_u \leq 11$  and  $4 \leq \ell_u \leq n_u - 1$  are tabulated in Table 4.1, where transition rates with  $n_u = 8$  and 9 are compared with those of hydrogen-like ions [99]. It is noted that most of the transitions with  $\ell_u \geq 5$  agree with the hydrogen-like values within 1 %.

On the other hand, because of the configuration interaction between  $3sn\ell$  and  $3p(d)n'\ell'$  configurations of  $\text{Ar}^{6+}$  ions, transition rates and lifetimes calculated by the MCHF code should be used with care. Table 4.2 shows the transition rates of the  $\text{Ar}^{6+}$  ions, where the rates are also compared with the hydrogen-like values. As is seen, transition rates with  $\ell_u \geq 6$  which are not influenced by the configuration interaction, agree with those of the hydrogen-like ion ( $\lesssim 2\%$ ), which is also true for  $n_u = 10$  and 11 transitions with  $\ell_u \geq 5$  (hence the data for  $n_u = 10$  and 11 are not shown in the table). The MCHF rates and lifetimes were used for these transitions in the following analysis. On the other hand, lifetimes of  $\ell_u = 5$  ( $n_u = 8, 9$ ) states largely (20 – 50 %) deviate from the hydrogen-like values. Lifetimes for these states were evaluated from experiments which will be discussed in the following section.

Transitions with  $\Delta\ell = \ell_u - \ell_l = -1$  were neglected for both  $\text{Ar}^{7+}$  and  $\text{Ar}^{6+}$  ions, because the corresponding transition rates are typically two or three orders of magnitudes smaller than those for  $\Delta\ell = 1$ .

## 4.2 Decay-curve Measurements

Figure 4.3 shows the energy diagram for  $\text{Ar}^{6+}$  ions. The transitions discussed in Chapter 3 are represented by the solid lines with the numbers showing resolved fine-structure components. Two sets of data were obtained in the experiments, *i.e.*, decay-curves in the time range  $0 \leq t \leq 12$  ns for the transitions in the region I in Fig. 4.3, and intensities at  $t = 0.8$  or 1.3 ns for the transitions in the region II.

### Ar VII (Data Set I)

We first measured decay-curves of the transitions within the region I shown in Fig. 4.3. Here the incident ions were 2.0 keV/amu  $\text{Ar}^{7+}$  ions. The width of the entrance slit of the spectrometer was set to 0.2 mm for all transitions except 0.5 mm for  $n_u = 8$  transitions (the difference in the slit width can be handled changing the  $\Delta t$  parameter in Eq. 4.7). The open circles with error bars in Figs. 4.4 show measured decay-curves. Here the detection efficiency depending on wavelength was corrected and, hence, the ordinates show quantities proportional to the number of photons emitted between  $t$  and  $t + \Delta t$ . Left and right figures are for transitions with  $\ell_u = n_u - 1$  (so called yrast transition) and  $\ell_u = n_u - 2$ , respectively. Equations 4.3-4.5 were solved

Table 4.1: Transition rates (in  $10^8 \text{ sec}^{-1}$ ) and lifetimes of  $Ar^{7+}$  by the HF calculation. The rates and lifetimes for  $n_u = 8$  and 9 transitions are compared with those of hydrogen-like ions.

Upper	Lower	Rate	Upper	Lower	Rate	Upper	Lower	Rate	H-like	%
(11,10)	(10,9)	2.99	(10,9)	(9,8)	4.87	(9,8)	(8,7)	8.34	8.33	0.12
Total		2.99	Total		4.87	Total		8.34	8.33	0.12
(11,9)	(10,8)	2.45	(10,8)	(9,7)	3.90	(9,7)	(8,6)	6.51	6.50	0.15
(11,9)	(9,8)	1.21	(10,8)	(8,7)	2.19	(9,7)	(7,6)	4.24	4.24	0.00
Total		3.66	Total		6.10	Total		10.8	10.7	0.93
(11,8)	(10,7)	2.00	(10,7)	(9,6)	3.12	(9,6)	(8,5)	5.04	5.04	0.00
(11,8)	(9,7)	1.69	(10,7)	(8,6)	2.94	(9,6)	(7,5)	5.40	5.38	0.37
(11,8)	(8,7)	0.09	(10,7)	(7,6)	1.82	(9,6)	(6,5)	3.97	3.96	0.25
Total		4.60	Total		7.88	Total		14.4	14.4	0.00
(11,7)	(10,6)	1.63	(10,6)	(9,5)	2.47	(9,5)	(8,4)	3.86	3.86	0.00
(11,7)	(9,6)	1.76	(10,6)	(8,5)	2.94	(9,5)	(7,4)	5.11	5.08	0.59
(11,7)	(8,6)	1.58	(10,6)	(7,5)	2.98	(9,5)	(6,4)	6.02	5.96	1.00
(11,7)	(7,6)	0.96	(10,6)	(6,5)	2.17	(9,5)	(5,4)	5.42	5.33	1.66
Total		5.95	Total		10.6	Total		20.5	20.2	1.46
(11,6)	(10,5)	1.31	(10,5)	(9,4)	1.93	(9,4)	(8,3)	2.88	2.92	1.39
(11,6)	(9,5)	1.63	(10,5)	(8,4)	2.59	(9,4)	(7,3)	4.24	4.22	0.47
(11,6)	(8,5)	1.84	(10,5)	(7,4)	3.26	(9,4)	(6,3)	6.03	5.92	1.82
(11,6)	(7,5)	1.85	(10,5)	(6,4)	3.79	(9,4)	(5,3)	8.37	8.10	3.23
(11,6)	(6,5)	1.33	(10,5)	(5,4)	3.38	(9,4)	(4,3)	9.86	9.34	5.27
Total		8.00	Total		15.0	Total		31.6	30.5	3.48
(11,5)	(10,4)	1.05	(10,4)	(9,3)	1.47	(8,7)	(7,6)	15.3	15.2	0.65
(11,5)	(9,4)	1.39	(10,4)	(8,3)	2.10	Total		15.3	15.2	0.65
(11,5)	(8,4)	1.78	(10,4)	(7,3)	2.93	(8,6)	(7,5)	11.5	11.5	0.00
(11,5)	(7,4)	2.21	(10,4)	(6,3)	4.12	(8,6)	(6,5)	8.94	8.90	0.45
(11,5)	(6,4)	2.56	(10,4)	(5,3)	5.68	Total		20.4	20.4	0.00
(11,5)	(5,4)	2.28	(10,4)	(4,3)	6.67	(8,5)	(7,4)	8.57	8.56	0.12
Total		11.4	Total		23.2	(8,5)	(6,4)	10.6	10.5	0.94
(11,4)	(10,3)	0.81				(8,5)	(5,4)	9.71	9.57	1.44
(11,4)	(9,3)	1.13				Total		29.0	28.7	1.03
(11,4)	(8,3)	1.53				(8,4)	(7,3)	6.24	6.29	0.80
(11,4)	(7,3)	2.11				(8,4)	(6,3)	9.37	9.23	1.49
(11,4)	(6,3)	2.95				(8,4)	(5,3)	13.2	12.8	3.03
(11,4)	(5,3)	4.05				(8,4)	(4,3)	15.7	14.9	5.10
(11,4)	(4,3)	4.75				Total		44.7	43.3	3.13
Total		17.6								

Table 4.2: Transition rates and lifetimes of  $Ar^{6+}$  by the MCHF calculation (see text).

Upper	Lower	MCHF	H-like	%	Upper	Lower	MCHF	H-like	%
9l	8k	4.89	4.88		8k	7i	9.00	8.93	
Total		4.89	4.88	0.2	Total		9.00	8.93	0.8
9k	8i	3.83	3.81		8i	7h	6.77	6.7	
	7i	2.54	2.48			6h	5.31	5.2	
Total		6.36	6.29	1.1	Total		1.21	1.19	1.7
9i( $^3I_5$ )	8h	2.69	2.95		8h( $^3H_4$ )	7g	4.57	5.02	
	7h	3.31	3.15			6g	3.98	6.18	
	6h	2.31	2.32			5g	6.36	5.61	
	3p5g	0.195				3p4f	5.96		
Total		8.53	8.42	1.3	Total		20.9	16.81	19.6
9i( $^3I_6$ )	8h	2.7	2.95		8h( $^3H_5$ )	7g	4.53	5.02	
	7h	3.31	3.15			6g	3.57	6.18	
	6h	2.32	2.32			5g	5.19	5.61	
	3p5g	0.187				3d <sup>2</sup>	1.16		
Total		8.517	8.42	1.1	Total		3p4f	6.83	
9i( $^1I_6$ )	8h	2.77	2.95		Total		21.3	16.81	21.1
	7h	3.31	3.15		8h( $^1H_5$ )	7g	4.67	5.02	
	6h	2.32	2.32			6g	3.80	6.18	
	3p5g	0.121				5g	4.90	5.61	
Total		8.521	8.42	1.2		3d <sup>2</sup>	0.913		
9i( $^3I_7$ )	8h	2.77	2.95			3p4f	5.06		
	7h	3.31	3.15		Total		19.4	16.81	13.4
	6h	2.32	2.32		8h( $^3H_6$ )	7g	4.71	5.02	
	3p5g	0.116				6g	4.32	6.18	
Total		8.516	8.42	1.1		5g	5.92	5.61	
9h( $^3H_4$ )	8g	1.85	2.26			3p4f	4.06		
	7g	3.23	2.98		Total		19.1	16.81	12.0
	6g	4.13	3.49		7i	6h	17.9	17.8	
	5g	3.88	3.12		total		17.9	17.8	0.6
	3p4f	5.73			7h( $^3H_4$ )	6g	12.2	12.8	
	3p5f	0.257				5g	12.9	12.2	
Total		19.1	11.85	38.0	Total		25.3	25.0	1.2
9h( $^3H_5$ )	8g	1.89	2.26		7h( $^3H_5$ )	6g	11.9	12.8	
	7g	3.24	2.98			5g	13.0	12.2	
	6g	4.18	3.49			3p4f	0.289		
	5g	4.74	3.12		Total		25.2	25.0	0.8
	3p4f	4.54			7h( $^1H_5$ )	6g	11.8	12.8	
	3p5f	0.199				5g	13.0	12.2	
	3d <sup>2</sup>	0.964				3p4f	0.402		
Total		19.8	11.85	40.2	Total		25.2	25.0	0.8
9h( $^1H_5$ )	8g	1.94	2.26		7h( $^3H_6$ )	6g	12.3	12.8	
	7g	3.27	2.98			5g	13.0	12.2	
	6g	4.45	3.49		Total		25.2	25.0	0.8
	5g	6.03	3.12						
	3p4f	4.4							
	3d <sup>2</sup>	2.47							
Total		22.7	11.85	47.8					
9h( $^3H_6$ )	8g	1.92	2.26						
	7g	3.23	2.98						
	6g	4.3	3.49						
	5g	4.29	3.12						
	3p4f	7.12							
	3p5f	0.145							
Total		21.0	11.85	43.6					

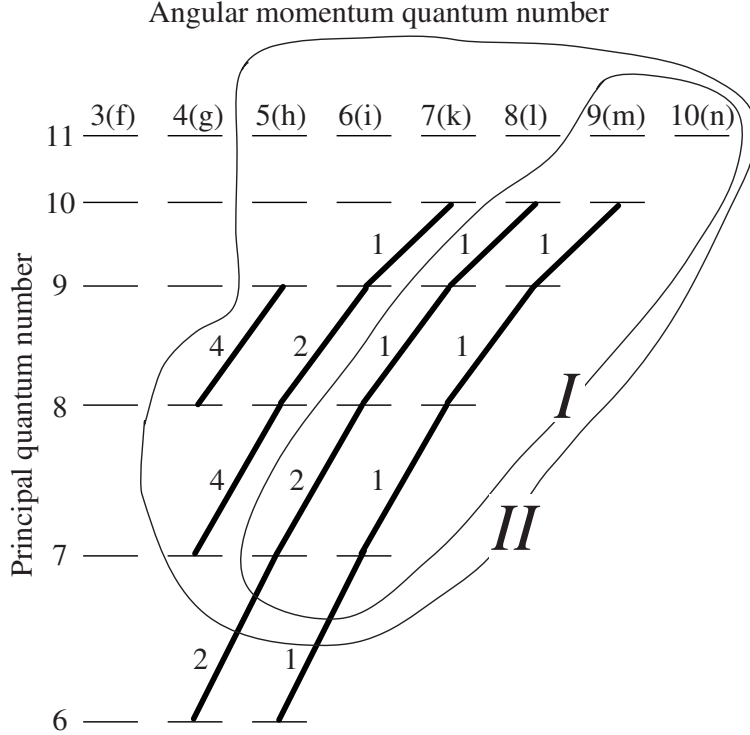


Figure 4.3: An energy diagram for  $\text{Ar}^{6+}$  ions. The solid lines correspond to the transitions observed in Chapter 3. The number shown along the lines shows the number of the resolvable fine-structure components. Region I and II show the group of lines observed in each measurement.

analytically to extract the initial population of each  $(n, \ell)$  state where  $N_{n,\ell}(0)$  with  $7 \leq n \leq 11$ , and  $n - 2 \leq \ell \leq n - 1$  were taken into account (i.e., ten  $N_{n,\ell}(0)$  are the free parameters to fit the eight decay curves) and then  $I_{n,\ell}^{n',\ell'}(t)$  were calculated analytically. Changing  $N_{n,\ell}(0)$ 's involved in  $I_{n,\ell}^{n',\ell'}(t)$ , analytic intensities were fitted to the corresponding observed intensities using the least squares method, where the sum of  $\chi^2$  over all data points was minimized ( $\chi$  shows the difference between analytical and observed line intensities which was divided by the statistical error). The resultant analytical decay-curves are shown by the solid lines in Fig. 4.4, which reproduce the observed decay-curves reasonably well. Figure 4.9 shows  $N_{n,\ell}(0)$  distribution obtained by the fitting, which has a peak around  $n \approx 8.5$  with its distribution width of  $\delta n \approx 2$ .

## Ar VII (Data Set II-1)

Next, the line intensities of the transitions in the region II in Fig. 4.3 were measured at the delay time of 0.8 ns. The slit width of the spectrometer was set to 0.07 mm and the incident energy of the  $\text{Ar}^{7+}$  ions was 2.0 keV/amu. Figures 4.5(A-D) show the resultant intensities for  $n_u = 10, 9, 8$  and  $7$ , respectively, where fine-structure components for transitions with the same  $\ell_u$  are summed up. In the analysis,  $N_{11,\ell}(0)$  populations

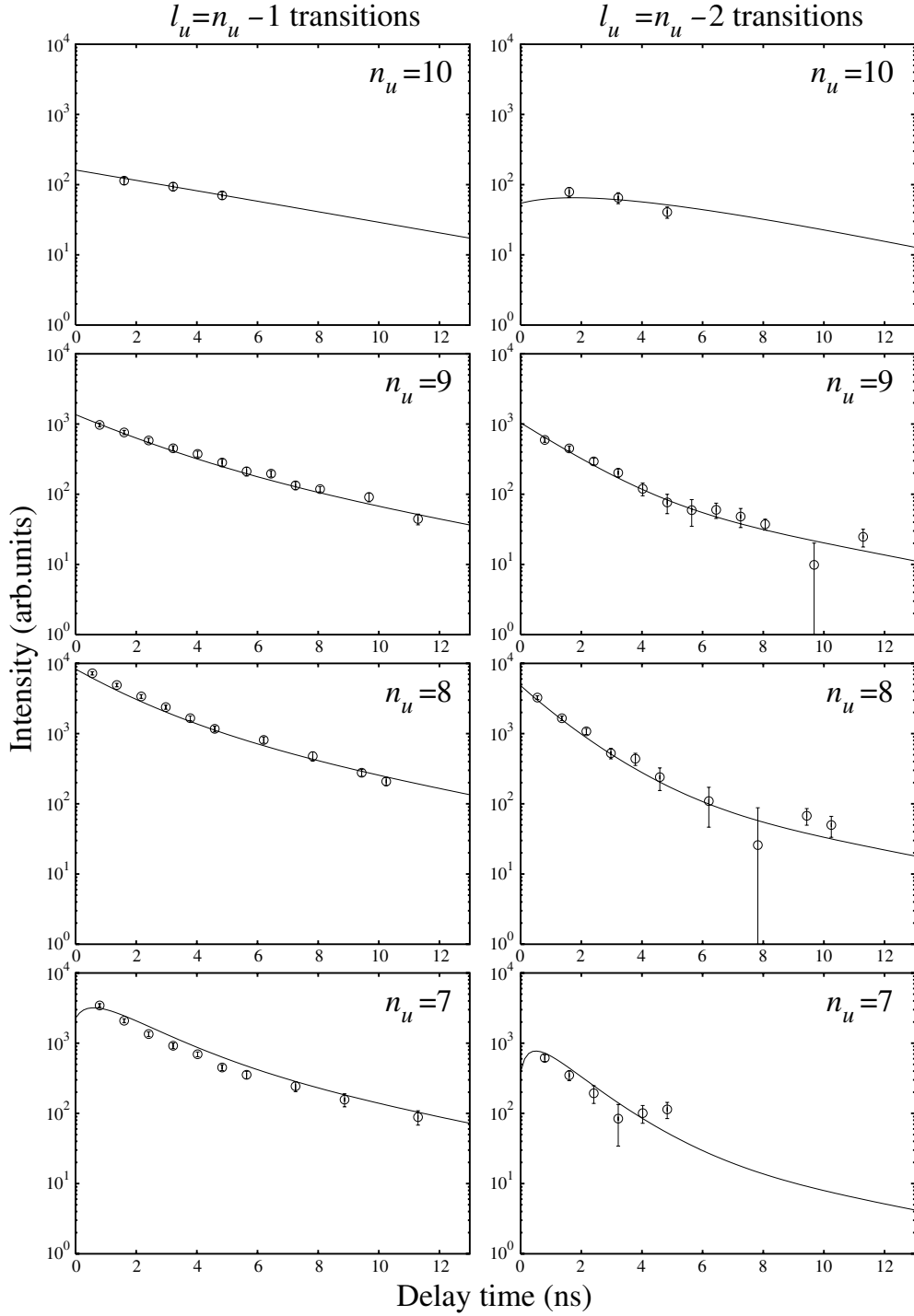


Figure 4.4: Decay-curves for  $\Delta n = 1$  transitions with  $7 \leq n_u \leq 10$  in the region I (Figure 4.3). Left and right side figures correspond to transitions with  $l_u = n_u - 1$  and  $n_u - 2$  states, respectively. Open circles with error bars show measured line intensities and solid lines show analytical decay-curves obtained using the least squares methods.

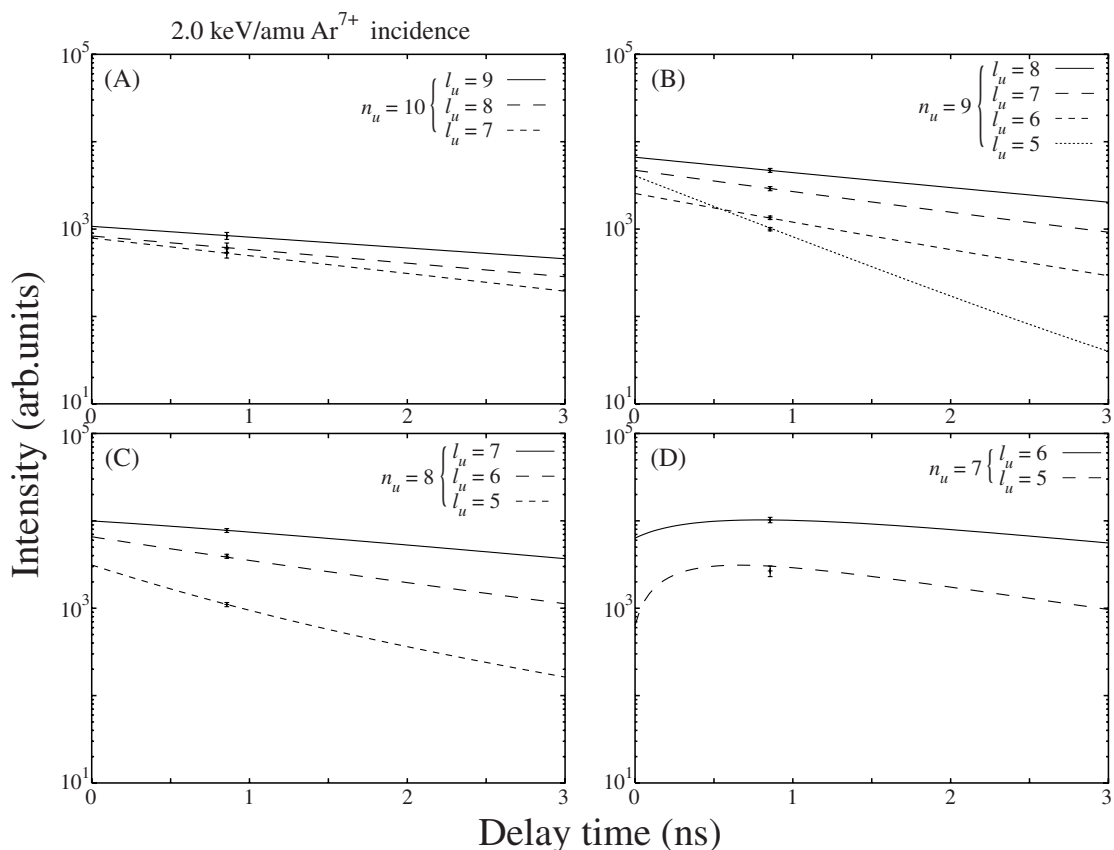


Figure 4.5: Line intensities of Ar VII spectra observed when 2.0 keV/amu Ar<sup>7+</sup> incident ions were used.

were not taken into account because our spectrometer was not sensitive to  $\Delta n = 1$  transitions with  $n_u = 11$  and line intensities for the lower  $n_u$  were measured at one delay time. Non-observed  $N_{10,6}(0)$  were assumed to be populated statistically against  $N_{10,9}(0)$ . The resultant analytical decay-curves are shown in Fig. 4.5, and  $N_{n,\ell}(0)$  distributions are shown in Fig. 4.10(A).

It is noted that, as was pointed out in Section 4.1.1, the lifetimes of MCHF calculation for (9,5) and (8,5) states in Table 4.2 are strongly influenced by the configuration interaction, and are shorter than those of hydrogen-like ions by 20 – 50 %. The dotted line in Fig. 4.6(A) shows the analytical decay-curve for  $n_u = 9$  and  $\ell_u = 5$  transition using the MCHF rates and lifetimes. It is shown that the line intensity for  $\ell_u = 5$  transition at the exit of the capillary should be the strongest among the  $n_u = 9$  transitions. According to Fig. 3.1 (page 49), the strongest line is around 567 nm (Table 3.1, page 51) around  $n_u = 9$  transitions in the  $Q_{in} = 7$  spectrum, which is close to  $\ell_u = 8$  and 7 transitions with wavelengths 566.4 nm and 565.3 nm in Table 3.3 (page 72), and sufficiently apart from the  $\ell_u = 5$  transition with wavelengths  $\sim 530$  nm. This indicates that the MCHF calculation for the lifetime of (9,5) state is incorrect. To estimate a

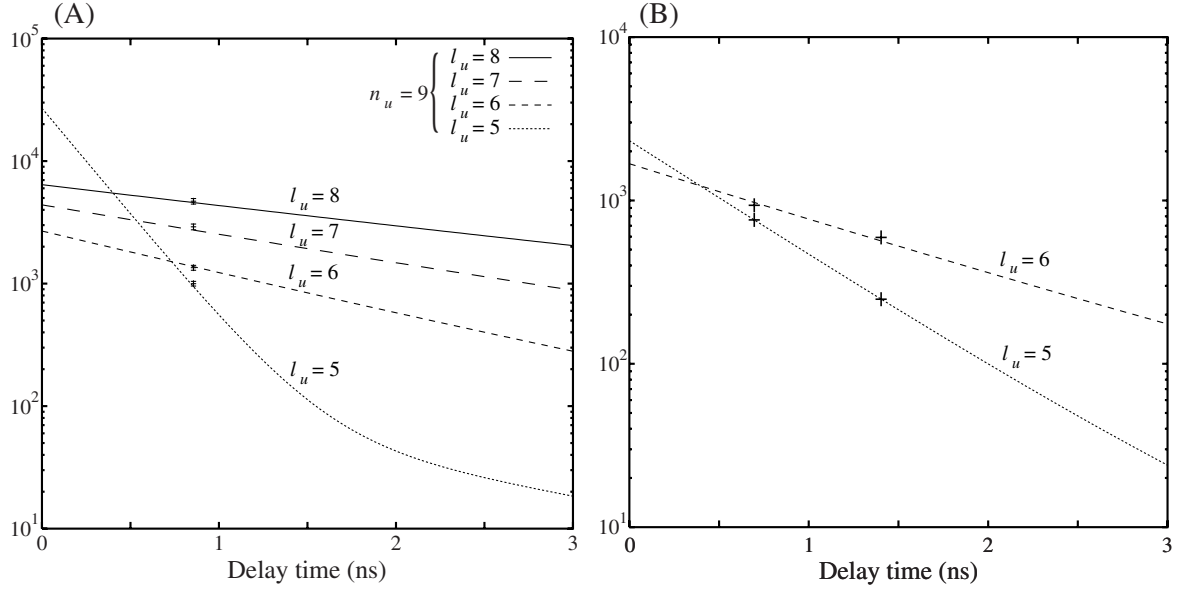


Figure 4.6: (A) Analytic decay curves of  $n_u = 9$  transitions when the MCHF lifetimes were used. (B) Intensity variations for  $l_u = 5$  and  $6$  transitions with  $n_u = 9$ .  $l_u = 5$  transition is reproduced with the evaluated lifetime of the  $(9, 5)$  state.

realistic lifetime for  $(9, 5)$  state experimentally, line intensities for  $\Delta n = 1$  transitions with  $n_u = 9$  and  $l_u = 6$  and  $5$  were measured at two different points downstream of the capillary. Fig. 4.6(B) shows the result in which the observed line intensities for  $l_u = 6$  transition (approximately hydrogen-like transitions) were reproduced well with the MCHF lifetime and initial populations of  $N_{10,7}(0)$  (which cascades into  $(9,6)$  state) and  $N_{9,6}(0)$  in Fig. 4.10(A). To reproduce  $l_u = 5$  line intensities, the analytic decay curve for  $l_u = 5$  was fitted to the observed line intensities with varying  $N_{9,5}(0)$  and the lifetime of the  $(9,5)$  states ( $N_{10,6}(0)$  in Fig. 4.10(A) were also taken into account). The resultant decay curve is shown by solid lines in Fig. 4.6(B) with its inverse lifetime of  $16.0 \times 10^8 \text{ sec}^{-1}$ . A similar analysis was also performed for  $l_u = 5$  and  $n_u = 8$  transition, and the inverse lifetime was  $17.6 \times 10^8 \text{ sec}^{-1}$ .

It is also noted that the transition rates for  $\Delta n = 1$  transitions with  $l_u = 5$  also deviate from the hydrogen-like values by  $\sim 20\%$  (see Table 4.2). According to Eq. 4.8, the analytical line intensities are proportional to  $N_{n,\ell}(0) \times A_{n,\ell}^{n',\ell'}$  which is a quantity determined from the observed line intensities. Hence initial populations extracted here are influenced by the precision of the calculated transition rates.

## Ar VII (Data set II-2)

For Ar VII lines, line intensities with different incident energy of  $0.88 \text{ keV/amu}$  (total energy  $35 \text{ keV}$ ) were also measured to study the dependence of the initial popu-

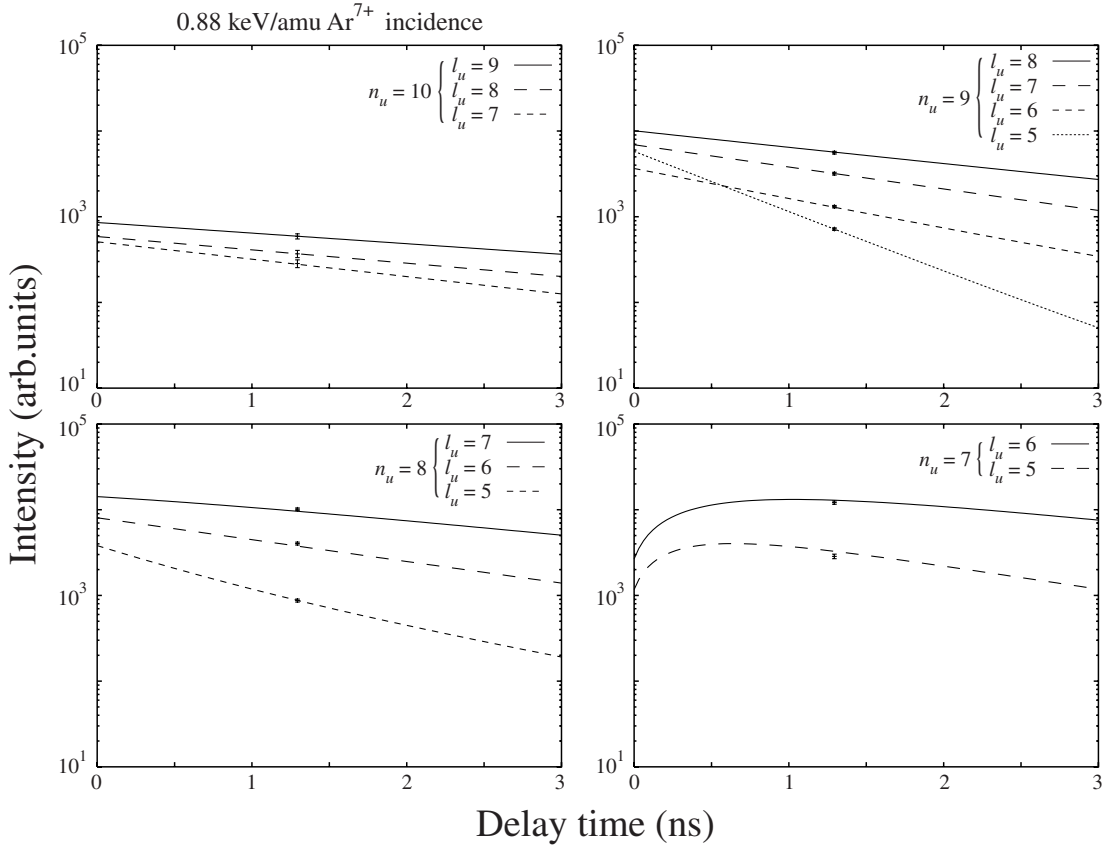


Figure 4.7: Line intensities of Ar VII spectra observed when 0.88 keV/amu  $\text{Ar}^{7+}$  ions impinged.

lations upon the incident velocity of the ion, which is shown in Fig. 4.7. The resultant initial populations are shown in Fig. 4.10(B). It is noted that because the observed line intensities were normalized to the same conditions (*i.e.*, transmitted current and detection efficiency) as in the Data Set II-1 (2.0 keV/amu), the resultant  $N_{n,\ell}(0)$  distributions in Figs. 4.10(A) and (B) can be compared with each other.

## Ar VIII

Line intensities of the Ar VIII spectra for 2.0 keV/amu  $\text{Ar}^{8+}$  incidence were also analyzed, which is shown in Fig. 4.8. The slit width of the spectrometer and intensity normalization were the same as the Data Set II of Ar VII, hence the result can be compared with those of Ar VII in Figs. 4.10(A) and (B). It is noted for the analysis of Ar VIII data that because transitions with  $\ell_u \geq 6$  were not resolved with our set-up due to very small polarizabilities of the core, it was assumed that states with  $6 \leq \ell \leq n-1$  are populated statistically. This assumption comes from the fact that  $\ell$  distributions for Ar VII in Fig. 4.10 are rather statistical than flat ( $\ell$ -independent). Non-observed  $N_{12,\ell}(0)$  populations were neglected by the same reason for the data set II in Ar VII.

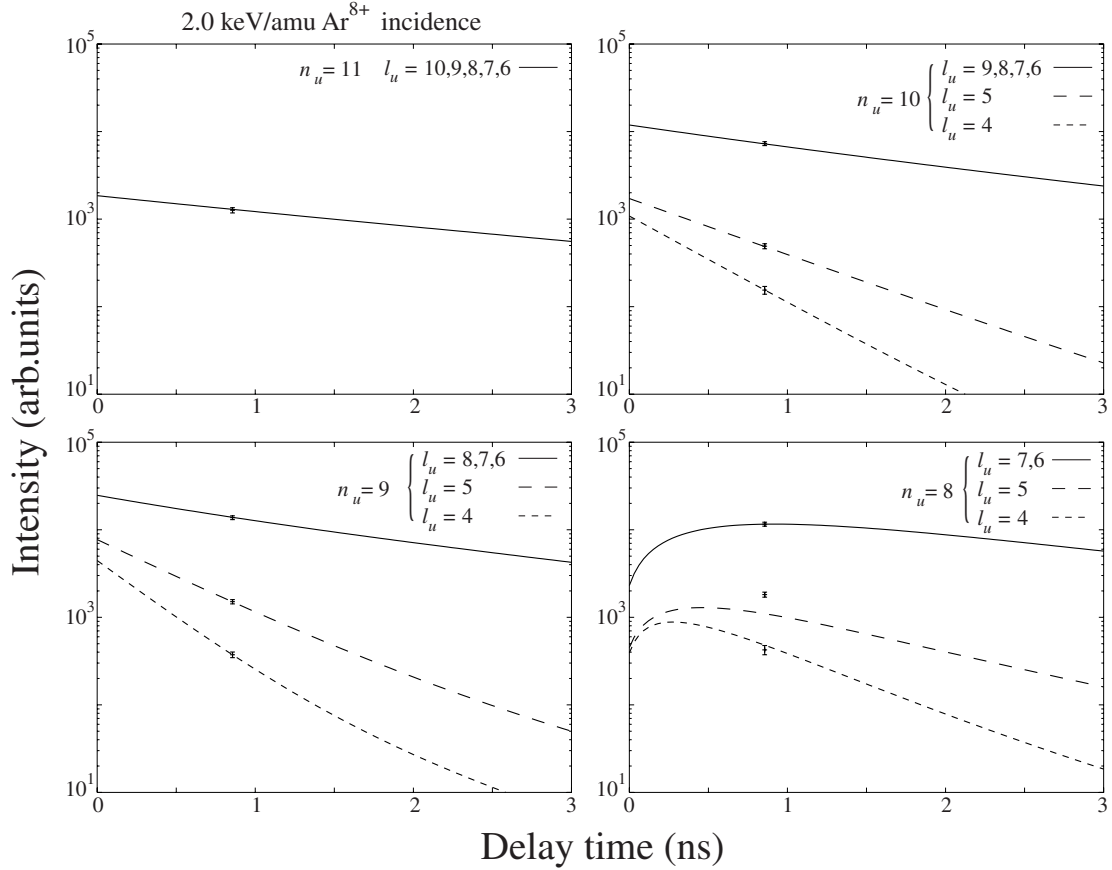


Figure 4.8: Line intensities of Ar VIII spectra observed when 2.0 keV/amu  $\text{Ar}^{8+}$  ions impinged. Because lines with  $\ell_u \geq 6$  were not resolved with the present setup, it is assumed in the analysis that these states are populated according to their statistical weights, and the solid line in each figure shows summed intensity over these states.

The resultant analytical decay-curves are shown with lines in Fig. 4.8, where the solid lines show the decay-curve summing over the unresolved lines ( $\ell_u \geq 6$ ). Fig. 4.11 shows the resultant initial populations.

### 4.3 Initial Population

Figure 4.9 and Figure 4.10(A) show the distributions of the initial population,  $N_{n,\ell}(0)$ , of the first electron transferred to 2.0 keV/amu  $\text{Ar}^{7+}$  ions. The difference of the average  $n$  values over  $\ell = n - 1$  distribution in Fig. 4.9 and 4.10(A) are very small  $\sim 0.1$ , *i.e.*, both distributions are more or less the same considering the experimental accuracies. The distributions have a peak at  $n \approx 8.5$  with a distribution width

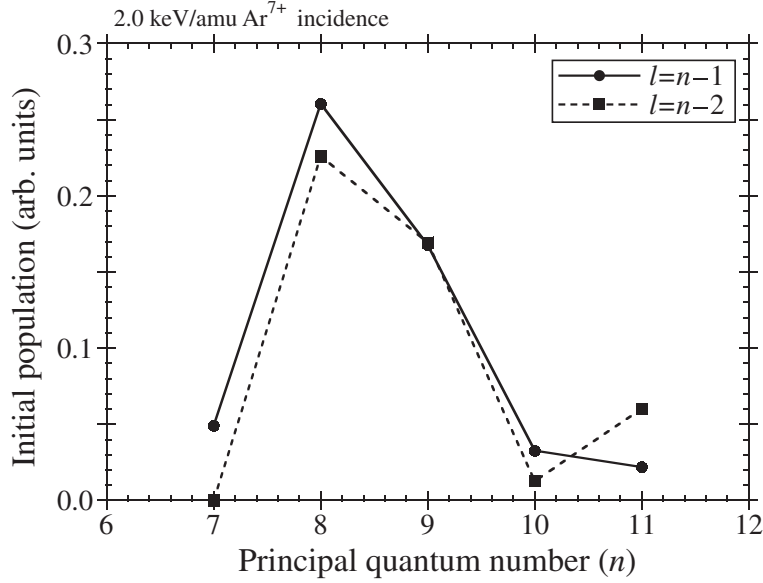


Figure 4.9: Initial state distributions of the first electron transfer obtained by fitting the decay-curves in Fig. 4.4. The closed circles and squares correspond to  $l = n - 1$  and  $n - 2$  states, respectively. Decay-curves from  $n \geq 11$  states were not measured and, hence,  $n = 11$  populations were included to reproduce the other decay-curves and to represent populations with  $n \geq 11$ .

of  $\delta n \approx 2$  (FWHM). For each  $n$  manifold, higher angular momentum states are preferred, *i.e.*,  $l$  distributions are rather statistical than flat ( $l$ -independent). The initial population of (9, 5) state ( $l = n - 4$  state denoted by  $\square$  in Fig. 4.10(A)) looks very high, although accurate estimation is quite difficult because fast decay channels with  $\Delta n \neq 1$  become more and more important for smaller  $l_u$  transitions.

Figure 4.10(B) shows the initial state distributions for 0.88 keV/amu  $\text{Ar}^{7+}$  ions, which is basically the same as those for 2.0 keV/amu  $\text{Ar}^{7+}$  ions shown in Fig. 4.10(A). The fact that  $l$  distributions do not depend upon the velocity of the incoming ions indicates that  $l$  distributions are not determined by a kinematic condition like  $l_k = m_e v_{ion} d_c$ , where  $m_e$  is the electron mass,  $v_{ion}$  the ion velocity and  $d_c(Q_{in}) = \sqrt{2Q_{in}}/W$  the critical distance for the first electron transfer (see Eq. 1.8). Actually, adopting  $Q_{in} = 7$  and  $W = 0.2$  a.u.,  $l_k$  for 2.0 keV/amu and 0.88 keV/amu are estimated to be 5.2 and 3.5, respectively.

Figure 4.11 shows the initial state distributions for 2.0 keV/amu  $\text{Ar}^{8+}$  incident ions. Because statistical populations for states with  $l \geq 6$  were assumed in the cascade analysis, only the initial populations for  $l = n - 1$  states are presented and connected with a solid line in the figure. Again the distribution width is  $\delta n \approx 2$  which is very similar to that for  $\text{Ar}^{7+}$  incident ions except for the fact that the peak position ( $n \approx 9.5$ ) shifts to higher  $n$  by 1.

From the distributions shown in Figs. 4.10 and 4.11, average values of initial prin-

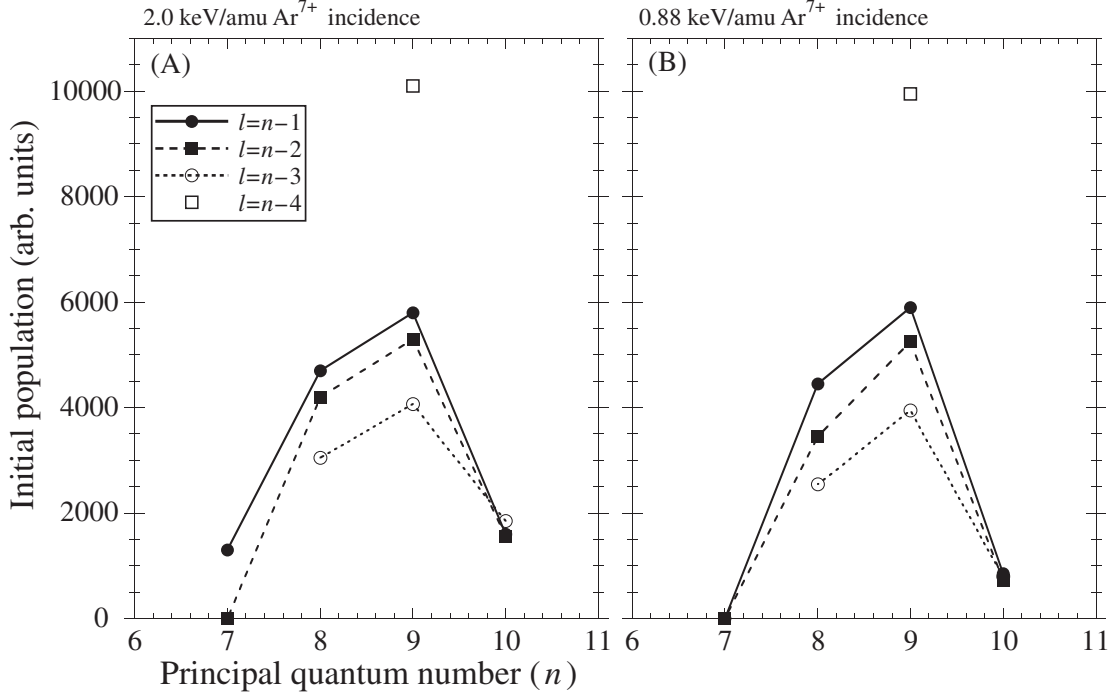


Figure 4.10: Initial state distributions obtained when 2.0 keV/amu (A) and 0.88 keV/amu (B)  $\text{Ar}^{7+}$  ions impinged (corresponding to decay-curves in Fig. 4.5 and 4.7, respectively). Although incident velocities are 1.5 times different, there is no remarkable change in the distributions. Both distributions have a peak around  $n \approx 8.5$  with the width of  $\delta n \approx 2$ .

principal quantum numbers  $\langle n_{av} \rangle$  over the distributions are calculated to be 8.6 and 9.5 for  $\text{Ar}^{7+}$  and  $\text{Ar}^{8+}$  incident ions, respectively. These results are plotted with closed squares (■) in Fig. 4.12. According to the classical over barrier model (COB model) [23], the first electron transfer takes place to a state with a critical principal quantum number,

$$n_c(Q_{in}) \approx \frac{Q_{in}}{\sqrt{2W}} \left( \frac{1}{1 + \frac{Q_{in}^{-\frac{1}{2}}}{\sqrt{8Q_{in}}}} \right)^{\frac{1}{2}}. \quad (4.10)$$

Adopting 0.191 a.u. (5.20 eV) for Ni work-function, which is an average value over those for different crystalline planes of Ni [100],  $n_c(Q_{in})$  is also plotted with open circles (○) in Fig. 4.12. The observed  $\langle n_{av} \rangle$  values agree with the COB prediction quite well. As is seen in Fig. 4.12,  $n_c(Q_{in})$  of Eq. 4.10 is approximately given by  $n_c(Q_{in}) \approx Q_{in} + 1.3$  for  $Q_{in}$  studied here. Memorizing that (1) the initial populations of  $n = Q_{in}$  states are almost zero for  $Q_{in} = 7$  and 8 in Figs. 4.10 and 4.11, and (2)  $n_u = Q_{in}$  transitions have the maximum line intensity and (3) line intensities for  $Q_{in} + s$  becomes weaker in the same manner increasing  $s$  from 1 to 3 in the low resolution spectra in Fig. 3.1, it is expected that  $n_c(Q_{in})$  in Eq. 4.10 is also a reliable measure for  $\langle n_{av} \rangle$  even for  $Q_{in} = 9$  and 10 incident ions.

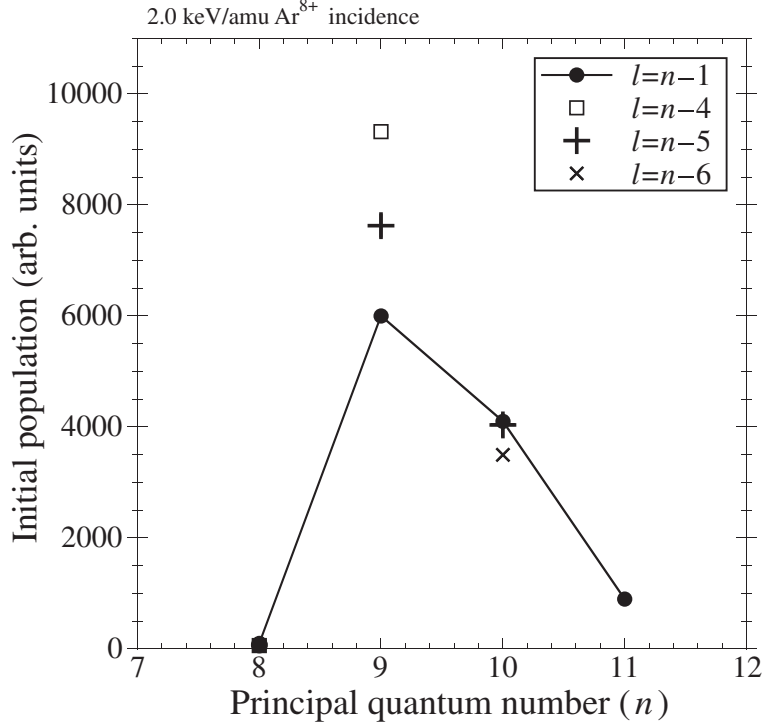


Figure 4.11: Initial state distributions when 2.0 keV/amu  $Ar^{8+}$  ions impinged (from decay-analysis in Fig. 4.8). The distributions have a peak around  $n \approx 9.5$  with the width of  $\delta n \approx 2$ .

### 4.3.1 Stark Effect

In the previous section, it is shown for the first time that the observed average principal quantum number  $\langle n_{av} \rangle$  of the first transferred electron is described quite well by the COB model ( $n_c$ ). In this section, we consider the  $\ell$  distributions and the widths ( $\delta n$ ) of the  $n$  distributions. When an ion approaches a metallic surface, an electric field is induced around the ion by its own image charge. The electric field at the moment of the first electron transfer is given in the frame of the COB model by

$$F(d_c(Q_{in})) = \frac{Q_{in}}{(2d_c(Q_{in}))^2} = \frac{W^2}{8}. \quad (4.11)$$

It is seen that  $F(d_c(Q_{in}))$  does not depend upon the incident charge,  $Q_{in}$ , but only upon the work-function of the surface,  $W$ . Adopting  $W = 0.191$  a.u. to Eq. 4.11,  $F(d_c)$  is estimated to be  $4.6 \times 10^{-3}$  a.u. ( $2.3 \times 10^9$  V/m). When the electric field is exerted on a hydrogen-like ion, energy levels of the ion are shifted due to the Stark effect. For a given  $n$  level, the energy shift from the non-perturbed energy level becomes the

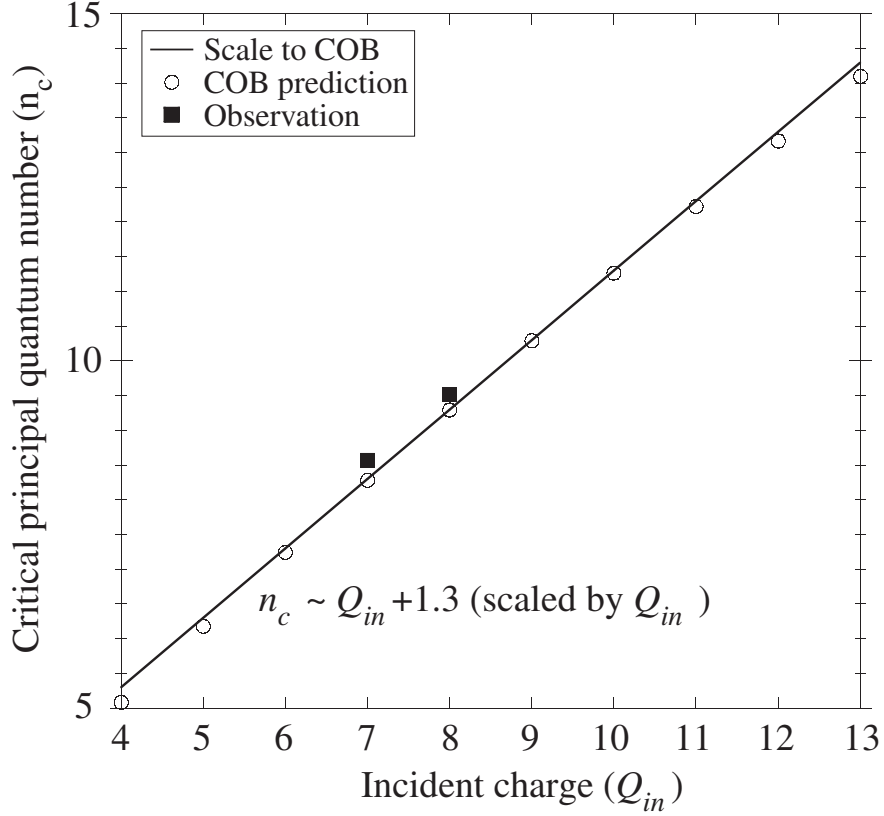


Figure 4.12: The critical principal quantum number,  $n_c(\circ)$ , predicted by the COB model as a function of the incident charge,  $Q_{in}$ . Observed average quantum numbers  $\langle n_{av} \rangle$  ( $\blacksquare$ ) are also shown. The  $\langle n_{av} \rangle$  values agree quite well with the COB model. The COB prediction is approximately given by  $n_c \approx Q_{in} + 1.3$  around  $Q_{in}$  studied, which suggests that the COB prediction holds even for  $Q_{in} = 9$  and 10 (see text).

largest for a state with its magnetic quantum number  $m = 0$ . The largest energy shift,  $\Delta E_{ss}^n$  [101], is given by

$$\Delta E_{ss}^n = \pm \frac{3F(d_c(Q_{in}))n(n-1)}{2Q_{in}} \quad (4.12)$$

Using Eqs. 4.11 and 4.12 and  $n \approx Q_{in} + 1$ ,  $\Delta E_{ss}^n$  is given by

$$\begin{aligned} \Delta E_{ss} &\approx \pm \frac{3W^2(Q_{in} + 1)}{16} \approx \pm 6.84 \times 10^{-3} \times (Q_{in} + 1) \quad (\text{a.u.}) \\ &\approx \pm 1.86 \times 10^{-1} \times (Q_{in} + 1) \quad (\text{eV}) \end{aligned} \quad (4.13)$$

For example, when  $Q_{in} = 8$  ( $n = 9$ ),  $\Delta E_{ss}$  is calculated to be  $\pm 6.2 \times 10^{-2}$  a.u. ( $\sim \pm 1.7$  eV). Although actual electronic states are not hydrogen-like, and the electronic field exerted on the ions in front of the capillary wall is not constant (Coulombic field),  $\Delta E_{ss}$  can be used as a measure of the Stark splitting, which is compared with

Table 4.3: Energy difference,  $\Delta E_\ell = E_{n-1} - E_\ell$ , between  $\ell = n - 1$  and  $\ell$  states (in a.u.) of the  $Ar^{7+}$  and  $Ar^{6+}$  ions calculated with the MCHF code. The last column shows Stark splitting for each  $n$ .  $a(b)$  shows  $a \times 10^{-b}$ .

Ion	$n$	$s$	$p$	$d$	$f$	$g$	$h$	$i$	$k$	$l$	$m$	$\Delta E_{ss}^n$
7+	10	3.6(2)	2.3(2)	6.3(3)	7.7(4)	2.4(4)	6.2(5)	1.2(5)	4.5(6)	3.5(6)	0	$\pm 7.7(2)$
	9	4.9(2)	3.2(2)	8.6(3)	1.1(3)	3.3(4)	8.3(5)	1.6(5)	4.6(6)	0		$\pm 6.2(2)$
	8	7.1(2)	4.6(2)	1.2(2)	1.5(3)	4.6(4)	1.0(4)	1.6(5)	0			$\pm 4.8(2)$
6+	9	4.9(2)	3.9(2)	1.1(2)	3.0(3)	7.3(3)	1.2(3)	3.5(4)	2.9(5)	0		$\pm 7.0(2)$
	8	7.1(2)	4.8(2)	1.7(2)	4.2(3)	5.6(3)	4.6(3)	4.1(4)	0			$\pm 5.5(2)$
	7	1.1(1)	7.3(2)	3.6(2)	6.2(3)	2.4(3)	2.5(3)	0				$\pm 4.1(2)$

the energy difference,  $\Delta E_\ell = E_{n-1} - E_\ell$ , between  $\ell = n - 1$  and  $\ell$  states for each  $n$ .

Table 4.3 shows  $\Delta E_\ell$  (in a.u.) of  $Ar^{7+}$  and  $Ar^{6+}$  ions calculated with the MCHF code. For  $\ell$  states with appreciable fine-structure splittings (especially  $Ar^{6+}$ ), the largest energy difference is presented. As is seen in Table 4.3, energy differences for states with  $\ell \geq 2(d)$  is smaller than  $\sim 10^{-2}$  a.u., and those for states with  $\ell = 0, 1$  is larger than  $\sim 10^{-2}$  a.u. due to deeper penetration into the electron cloud of the core. It is seen that  $\Delta E_\ell$  is much smaller than or at least comparable to  $\Delta E_{ss}^n$  in the last column in Table 4.3, which means in other words that different angular momentum states with the same magnetic quantum number are more or less mixed up with each other.

In addition to the  $\ell$  degeneracy, energy difference between each neighboring  $n$  levels involved in the observed transitions ( $\Delta E_n \approx 1/Q_{in} \approx 0.1$  a.u., see Eq. 1.23) is close to  $|\Delta E_{ss}^{n+1}| + |\Delta E_{ss}^{n+2}|$ . Figure 4.13 shows energy-level variations of Stark states with  $n$  from  $Q_{in}$  to  $Q_{in} + 4$  as a function of the incident charge  $Q_{in}$ , where, for example,  $E^\pm(Q_{in} + 1) = E_n \pm \Delta E_{ss}^{Q_{in}+1}$  shows energies with the largest deviations from the hydrogen-like energy for  $n = Q_{in} + 1$  states. The thin line denoted by “ $E_{COB}$ ” shows the energy of the first electron transfer predicted by the COB model, *i.e.*,  $E_{COB}(Q_{in}) \approx -(Q_{in})^2/2(Q_{in} + 1.3)^2$ . It is seen within the incident charge states studied that (1)  $E^-(Q_{in} + 2) \leq E_{COB} \leq E^+(Q_{in} + 1)$  is always fulfilled, (2)  $E^-(Q_{in} + 3)$  and  $E^-(Q_{in} + 4)$  are slightly higher than  $E_{COB}(Q_{in})$  ( $E^-(Q_{in} + 3)$  becomes comparable to  $E_{COB}(Q_{in})$  around  $Q_{in} = 9$ ), and (3)  $E^+(Q_{in})$  is much lower than  $E_{COB}(Q_{in})$ . A very close correspondence to this picture is found in the experimentally-estimated initial populations, *i.e.*, (1)  $n = Q_{in} + 1$  and  $n = Q_{in} + 2$  states are most likely populated and (2)  $n = Q_{in} + 3$  and  $n = Q_{in}$  states are populated only very weakly.

Figure 4.14 shows a calculated energy diagram of hydrogen-like  $Q_{in} = 8$  ions in front of the capillary wall, where each state is classified into  $|\mu, m\rangle$  by a magnetic quantum

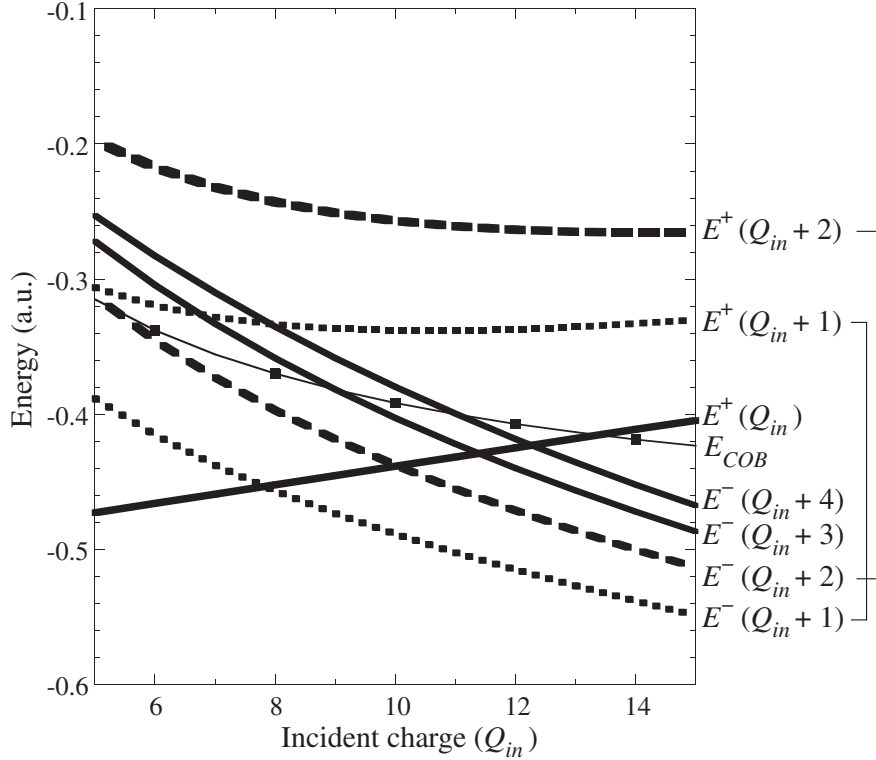


Figure 4.13: Energy variations of the two extreme Stark states with  $n$  from  $Q_{in}$  to  $Q_{in} + 4$  as a function of the incident charge  $Q_{in}$ . The thin line denoted by  $E_{COB}$  shows the energy for the first electron transfer.

number  $m$  ( $0 \leq |m| \leq n - 1$ ) and an additional quantum number  $\mu$  ( $1 \leq \mu \leq n - m$ ). The corresponding wave function is given by a linear combination of hydrogen-like wave functions  $|n, \ell, m\rangle$ , *i.e.*,

$$|\mu, m\rangle = \sum_{\ell=m}^{n-1} c_{\ell} |n, \ell, m\rangle.$$

$E_{COB}$  shows the COB prediction of the first electron transfer.

Assuming an “energy window” ( $\delta E$ ) around  $E_{COB}$ , the sum of the squared  $c_{\ell}^2$  for each  $|n, \ell, m\rangle$  state ( $n = 9, 10$ ) which is within  $E_{COB} \pm \delta E/2$  were calculated. Figures 4.15 shows the results when  $\delta E$  varies from 0.01 a.u. to 0.16 a.u.. Increasing  $\Delta E$  to  $\sim 0.9$  a.u., the distribution monotonically increases for larger  $\ell$ , which seems to give a close agreement with the observed distributions, which are nearly statistical.

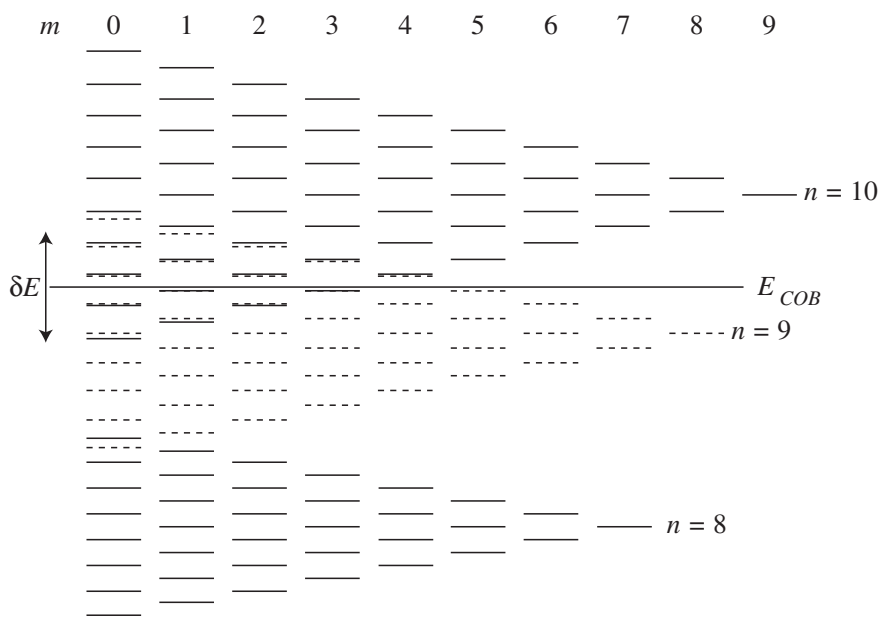


Figure 4.14: The energy diagram of the hydrogen-like  $Q_{in} = 8$  ion in the electronic field  $F = W^2/8$ . Numbers in the top show magnetic quantum numbers of the states.  $E_{COB}$  is for  $Q_{in} = 8$ .

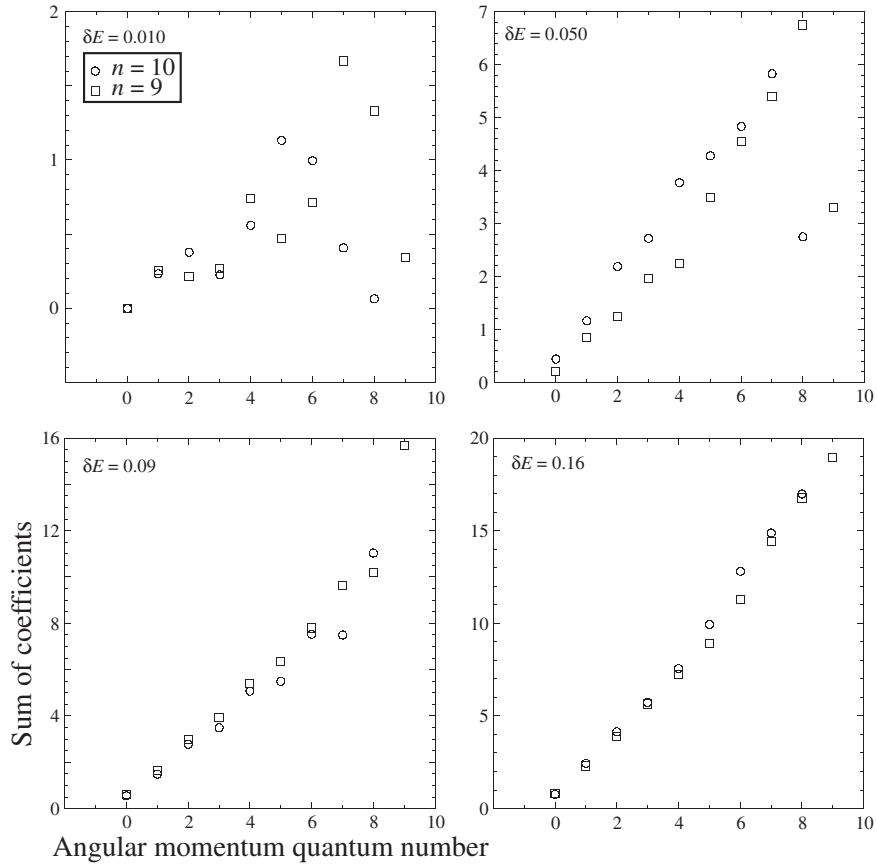


Figure 4.15: Sum of squared coefficients,  $c_l^2$ , for states involved in the energy  $E_{COB} - \delta E/2 \leq E \leq E_{COB} + \delta E/2$ . The open squares and open circles correspond to  $n_i = 9$  and 10 states, respectively.

# Chapter 5

## Summary

In summary, we have evaluated the initial populations on each  $(n, \ell)$  state of the first electron transferred to 2.0 keV/amu  $\text{Ar}^{Q_{in}+}$  ( $Q_{in} = 7, 8$ ) incident ions by fitting the analytical intensities to the observed line intensities. It is found for the first time that the  $(n, \ell)$  distributions have a peak around  $n \approx Q_{in} + 1.5$  with a distribution width of  $\delta n \approx 2$ , and  $\ell$  distributions are more or less statistical. The average values of  $n$  distributions agree quite well with the theoretical prediction by the classical over barrier model ( $n_c \approx Q_{in} + 1.3$ ). A fact that line intensities in Fig. 3.1 are scaled by  $Q_{in}$ , suggests that the prediction is also a reliable measure for  $Q_{in} = 9, 10$  incident ions although we did not analyze in detail.

Comparison with the result for 0.88 keV/amu  $\text{Ar}^{7+}$  incident ions reveals that the initial  $(n, \ell)$  distributions do not depend upon the incident velocity of the ion. This indicates that the  $\ell$  distribution is not determined by the kinematical condition but the Stark effect due to the electric field induced by the image charge. It is found that the electric field is strong enough to mix up with not only each  $\ell$  state with the same  $n$  but also  $n = Q_{in} + 1$  and  $n = Q_{in} + 2$  states, which is consistent with the fact that these states are populated most strongly.

# Appendix A

## Polarization Formula

When a Rydberg electron orbits far from the ionic core, which is well fulfilled for orbitals with higher  $n$  and  $\ell$ , two effects, *i.e.*, core polarization and core penetration, make energy levels of the ions deviate from hydrogen-like levels,

$$E_n^H = -\frac{Ry Q_{in}^2}{n^2}, \quad (\text{A.1})$$

where  $Ry$  is the Rydberg energy corrected for an ionic mass. When the Rydberg electron penetrates into the electron cloud of the core, it feels a larger charge than  $Q_{in}$ , which makes the energy level deeper than the hydrogen-like level. Such a core penetration effect is a short-range effect and well described by the quantum defect theory. The energy levels are given by

$$E_{n,\ell}^{Pen} = -\frac{Ry Q_{in}^2}{(n - \delta_\ell)^2} \approx E_n^H - \frac{2Ry \delta_\ell}{n^3}, \quad (\text{A.2})$$

where  $\delta_\ell$  is the quantum defect which depends on  $\ell$ . The second relation in Eq. A.2 is obtained assuming  $n \gg \delta_\ell$ . The quantum defect gets smaller as  $\ell$  gets larger because the penetration of the Rydberg electron into the core is prevented by stronger centrifugal potential,  $\ell(\ell + 1)/2r^2$ .

On the other hand, the electrostatic interaction between the Rydberg electron and the core electrons deforms the charge distribution of the core, which in turn modifies the energy level of the Rydberg electron. This is called the polarization effect which is important even for higher  $\ell$  orbitals. When the Rydberg electron can be regarded to orbit around the ionic core with its velocity small enough compared with the core-electron velocity, the energy levels accounted for the polarization energy is given by

$$E_{n,\ell}^{pol} = -\frac{Ry Q_{in}^2}{n^2} - \alpha_d Ry \langle r^{-4} \rangle - \alpha_q Ry \langle r^{-6} \rangle, \quad (\text{A.3})$$

where quantities shown with brackets represent expectation values calculated with hydrogenic wave functions, and  $\alpha_d$  and  $\alpha_q$  are dipole and quadrupole polarizabilities,

respectively. Analytic expressions for  $\langle r^{-4} \rangle$  and  $\langle r^{-6} \rangle$  are calculated and tabulated in many articles [81], which are given by

$$\langle r^{-4} \rangle = \frac{Q_{in}^4 (3n^2 - \ell(\ell + 1))}{2n^5 (\ell - \frac{1}{2}) \ell (\ell + \frac{1}{2}) (\ell + 1) (\ell + \frac{3}{2})}, \quad (\text{A.4})$$

$$\langle r^{-6} \rangle = \frac{Q_{in}^6 (35n^4 - n^2 [30\ell(\ell + 1) - 25] + 3(\ell - 1)\ell(\ell + 1)(\ell + 2))}{8n^7 (\ell - \frac{3}{2}) (\ell - 1) (\ell - \frac{1}{2}) \ell (\ell + \frac{1}{2}) (\ell + 1) (\ell + \frac{3}{2}) (\ell + 2) (\ell + \frac{5}{2})} \quad (\text{A.5})$$

Equations A.4 and A.5 are adoptable for wave functions with  $\ell \geq 1$  and  $\ell \geq 2$ , respectively. The polarization energy can be divided into  $Q_{in}$ -dependent term and  $n, \ell$ -dependent term,

$$E_{pol} = A(Q_{in}) p(n, \ell) (1 + k(Q_{in}) q(n, \ell)), \quad (\text{A.6})$$

$$A(Q_{in}) = \alpha_d Ry Q_{in}^4, \quad (\text{A.7})$$

$$k(Q_{in}) = Q_{in}^2 \frac{\alpha_q}{\alpha_d}, \quad (\text{A.8})$$

$$p(n, \ell) = \frac{\langle r^{-4} \rangle}{Q_{in}^4}, \quad (\text{A.9})$$

$$q(n, \ell) = \frac{\langle r^{-6} \rangle}{Q_{in}^6} \cdot \frac{Q_{in}^4}{\langle r^{-4} \rangle}. \quad (\text{A.10})$$

In the case that the Rydberg electron orbits around the core with comparable velocity with the response of the core charges, a non-adiabatic correction to  $\alpha_d$  must be considered [79]. The correction is given by

$$E_{corr} = -6\beta \langle r^{-6} \rangle, \quad (\text{A.11})$$

which has the same order of contribution to the energy levels as the quadrupole term.

# Appendix B

## Z-dependent Perturbation Theory

In a non-relativistic atomic system with  $N$  electrons, atomic wave functions are obtained solving the Schrödinger equation with the Hamiltonian,

$$\mathcal{H} = \sum_{i=1}^N \left( -\frac{1}{2} \nabla_i^2 - \frac{Z}{r_i} \right) + \sum_{i>j}^N \frac{1}{r_{ij}}, \quad (\text{B.1})$$

where  $Z$  is the nuclear charge of the atom,  $r_i$  is the distance of the  $i$ -th electron from the nucleus, and  $r_{ij}$  is the distance between  $i$ -th and  $j$ -th electrons. In the  $Z$ -dependent perturbation theory developed by Layzer [93, 94], the unit of length is changed by introducing a new variable  $\rho = Zr$ . Then the Hamiltonian can be written as

$$\mathcal{H} = Z^2 (\mathcal{H}_0 + Z^{-1} \mathcal{V}) \quad (\text{B.2})$$

with

$$\mathcal{H}_0 = \sum_{i=1}^N \left( -\frac{1}{2} \nabla_i^2 - \frac{1}{\rho_i} \right), \quad (\text{B.3})$$

$$\mathcal{V} = \sum_{i>j}^N \frac{1}{\rho_{ij}}. \quad (\text{B.4})$$

The Schrödinger equation to be solved becomes

$$(\mathcal{H}_0 + Z^{-1} \mathcal{V}) \psi = Z^{-2} E \psi. \quad (\text{B.5})$$

Expanding  $\psi$  and  $E$  in the inverse powers of  $Z$ , *i.e.*,

$$\psi = \psi_0 + Z^{-1} \psi_1 + Z^{-2} \psi_2 + \dots, \quad (\text{B.6})$$

$$E = Z^2 (E_0 + Z^{-1} E_1 + Z^{-2} E_2 + \dots), \quad (\text{B.7})$$

and inserting them to the Schrödinger equation, one obtains equations for  $\psi_k$  and  $E_k$ :

$$(\mathcal{H}_0 - E_0) \psi_0 = 0, \quad (\text{B.8})$$

$$(\mathcal{H}_0 - E_0) \psi_1 = (E_1 - \mathcal{V}) \psi_0, \quad (\text{B.9})$$

$$(\mathcal{H}_0 - E_0) \psi_2 = (E_1 - \mathcal{V}) \psi_1 + E_2 \psi_0. \quad (\text{B.10})$$

The solution of Eq. B.8 can be written using the hydrogen-like wave functions,

$$\mathcal{H}_0|(nj)\gamma J\rangle = -\sum_{i=1}^N \frac{1}{2n_i^2}|(nj)\gamma J\rangle, \quad (\text{B.11})$$

where  $(nj)$  represents a set of  $N$  quantum numbers  $(n_1j_1, n_2j_2, \dots, n_Nj_N)$ ,  $J$  is the total angular momentum and  $\gamma$  represents the other additional quantum numbers to specify all the states labeled by the same  $J$  and  $(nj)$ . Since  $E_0 = -\sum_{i=1}^N 1/2n_i^2$  depends only upon  $n_i$ 's ( $E_0$  is degenerate.), according to the perturbation theory for degenerate states,  $\psi_0$  is a linear combination of wave functions for the degenerate configurations,

$$\psi_0 = \sum_{j',\gamma'} c_{j',\gamma'} |(nj')\gamma' J\rangle, \quad (\text{B.12})$$

where  $c_{j',\gamma'}$  are determined as coefficients of an eigenvector of the interaction matrix  $\langle (nj)\gamma J | \mathcal{V} | (nj')\gamma' J \rangle$ , which, at the same time, determines corresponding eigenvalue  $E_1$ , *i.e.*,

$$\sum_{(j',\gamma')} \langle (nj)\gamma J | \mathcal{V} | (nj')\gamma' J \rangle c_{j',\gamma'} - E_1 c_{j,\gamma} = 0. \quad (\text{B.13})$$

The first order correction  $\psi_1$  is a solution of Eq. B.9. Since  $(E_1 - \mathcal{V})\psi_0$  in Eq. B.9 is orthogonal to each  $|(nj)\gamma J\rangle$ ,  $\psi_1$  can be expanded as a linear combination of wave functions for intermediate configuration,  $|\gamma_v J\rangle$ ,

$$\begin{aligned} \psi_1 &= \sum_v \frac{|\gamma_v J\rangle \langle \gamma_v J | \mathcal{V} | \psi_0 \rangle}{E_0 - E_{\gamma_v J}}, \\ E_{\gamma_v J} &= \langle \gamma_v J | \mathcal{H}_0 | \gamma_v J \rangle, \end{aligned} \quad (\text{B.14})$$

where  $|\gamma_v J\rangle$  is an eigenvector of  $\mathcal{H}_0$  whose eigenvalue,  $E_{\gamma_v, J}$  is not equal to  $E_0$ . The summation in Eq. B.14 is taken over all of discrete and continuum states except for those with the eigenvalue  $E_0$ . Substituting Eq. B.12 into Eq. B.14 and interchanging the orders of the summation, one gets

$$\psi_1 = \sum_{j',\gamma'} c_{j',\gamma'} \sum_v \frac{|\gamma_v J\rangle \langle \gamma_v J | \mathcal{V} | (nj')\gamma' J \rangle}{E_0 - E_{\gamma_v J}}. \quad (\text{B.15})$$

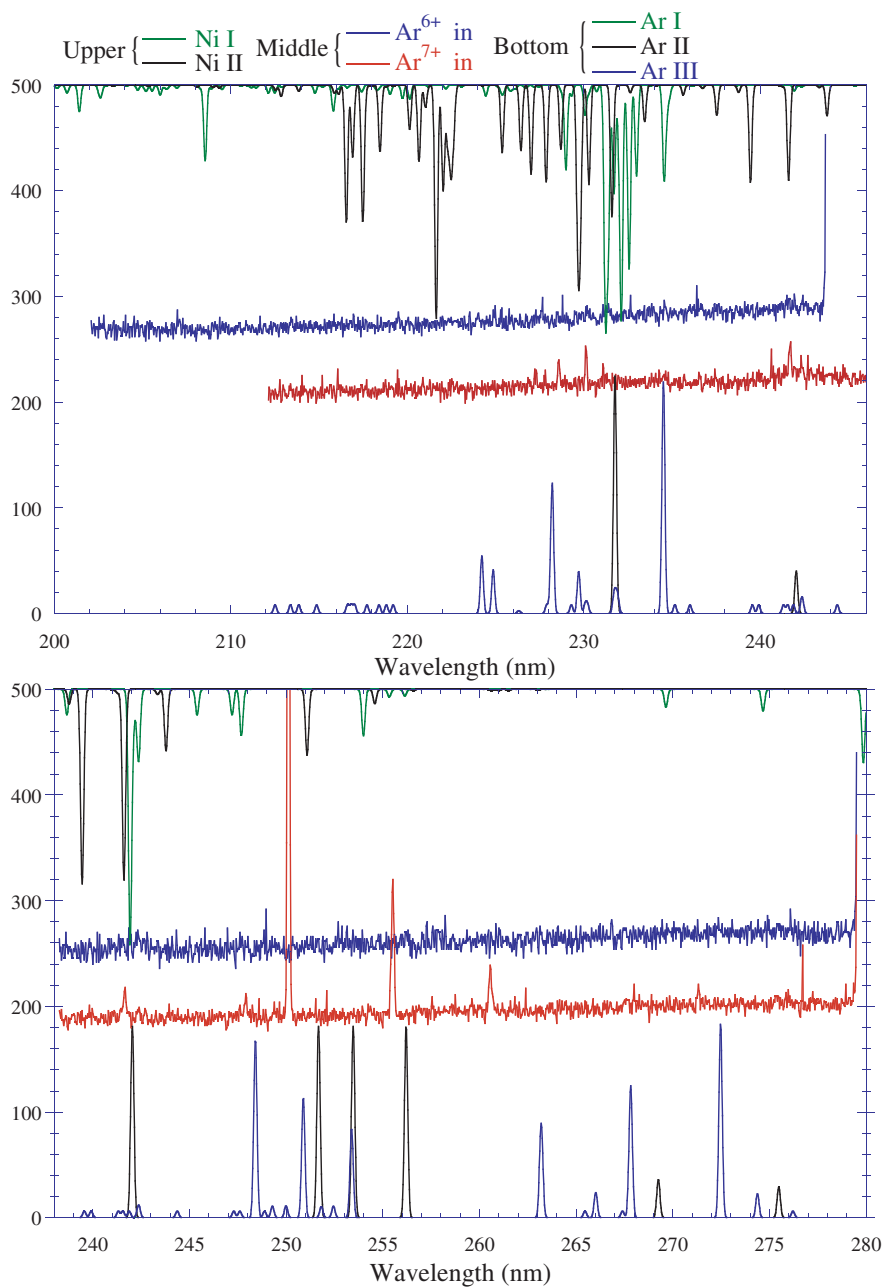
Equation B.15 shows that, through the interaction potential  $\mathcal{V}$ , the total wave functions for the system are deformed from the zeroth order wave functions  $\psi_0$  to those containing wave functions for other configurations  $|\gamma_v J\rangle$ , which has the same  $J$  quantum number as  $\psi_0$ .

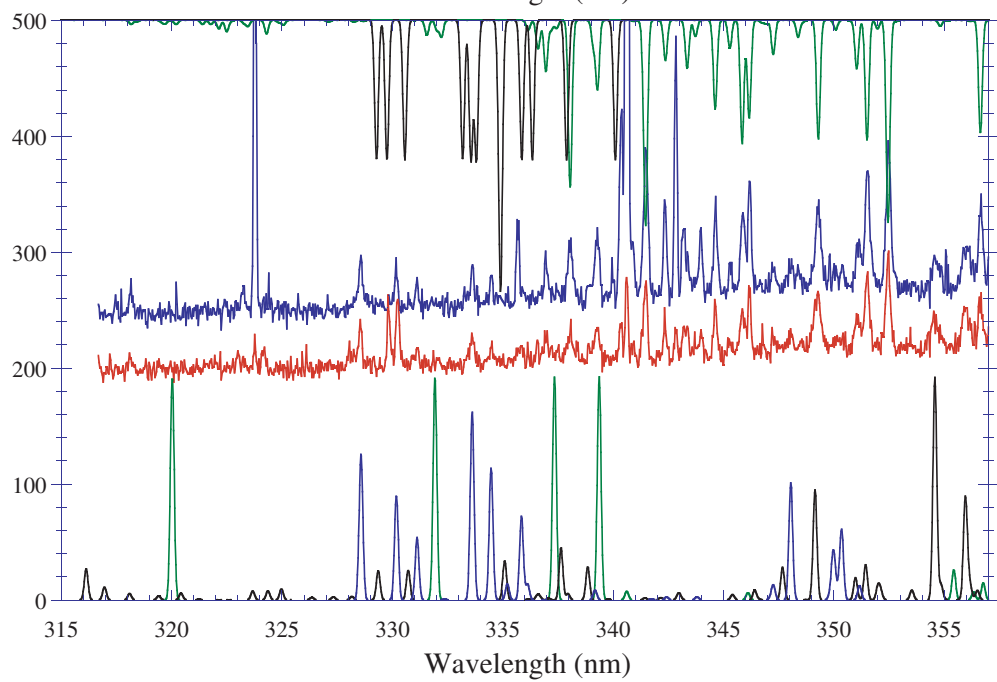
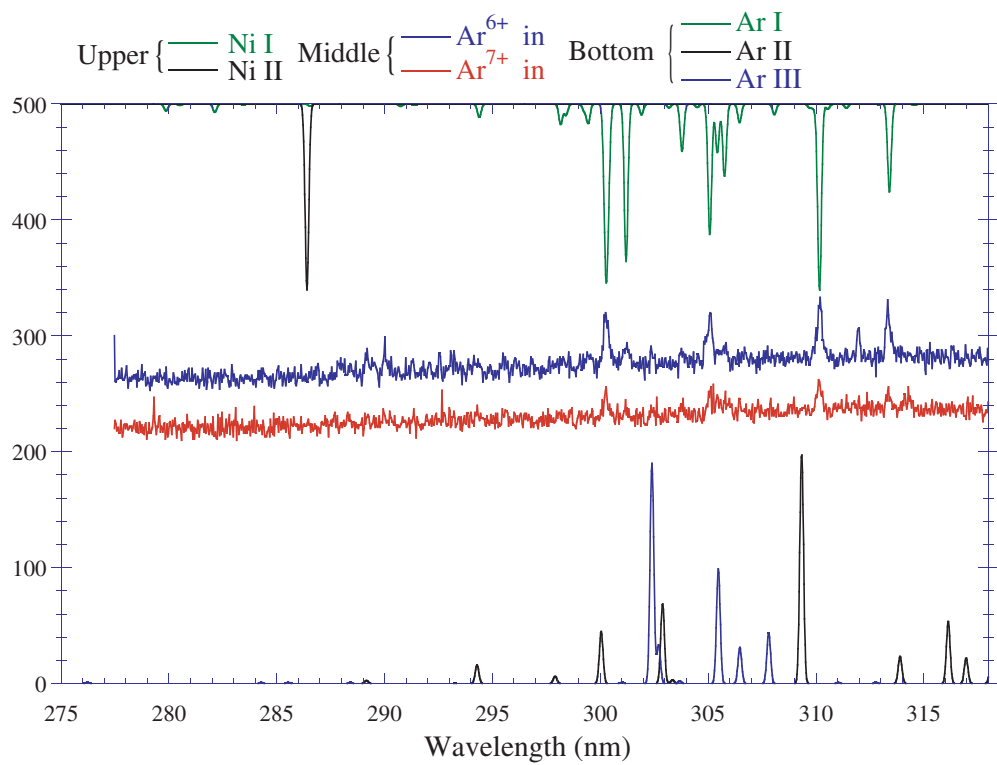
# Appendix C

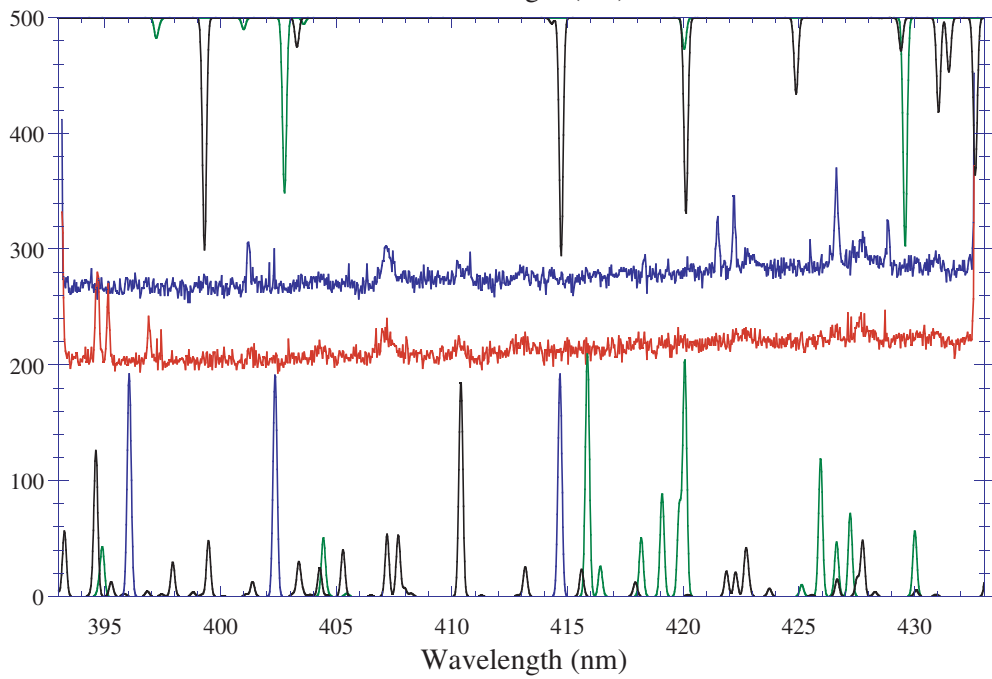
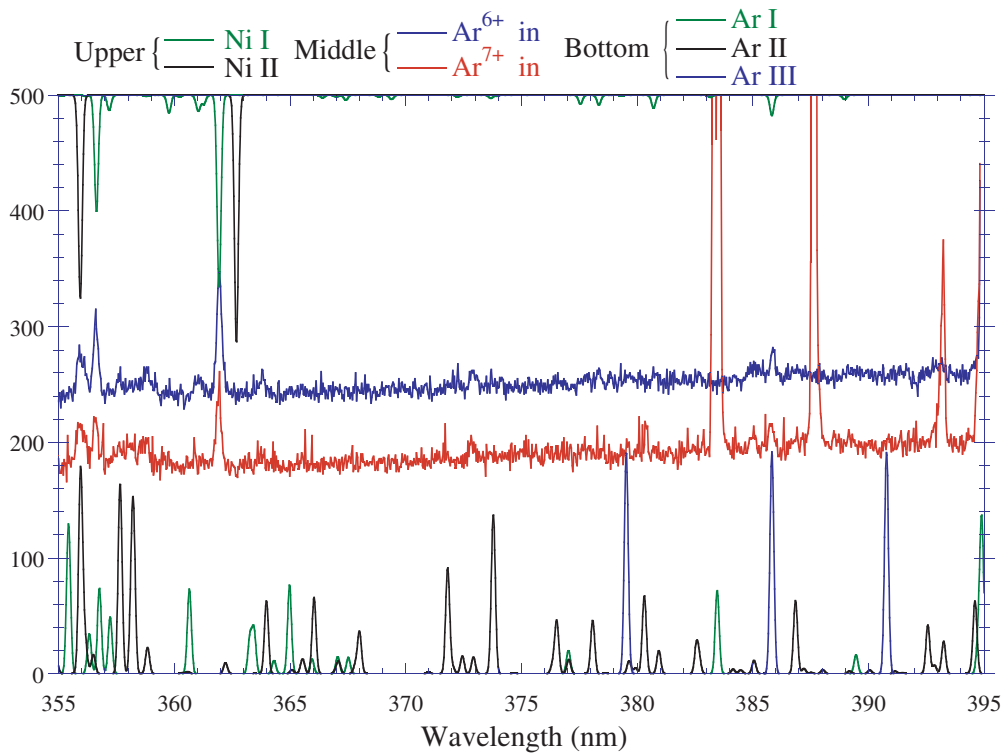
## Ar $^{Q_{in}+}$ Spectra

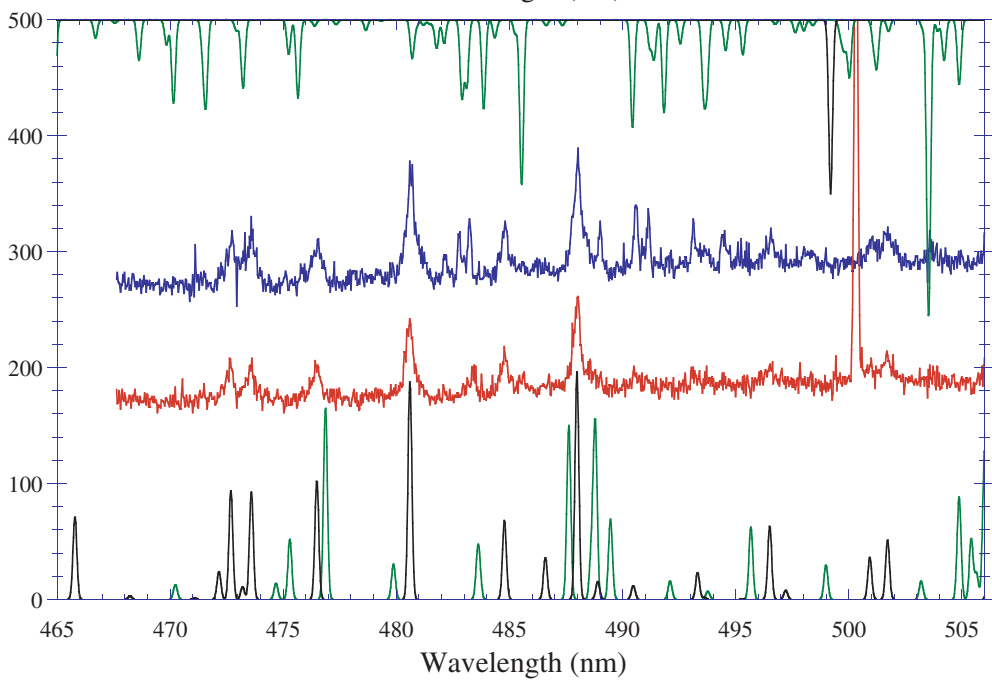
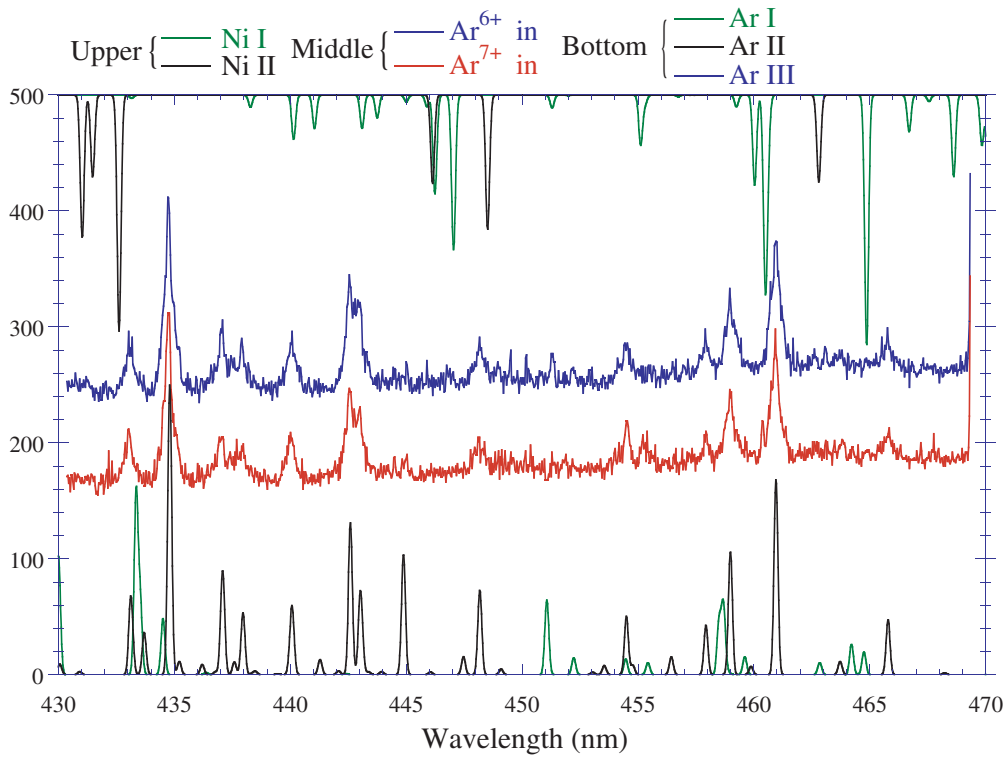
Spectra in the whole range of wavelength from 200 nm to 850 nm are shown for 2.0 keV/amu Ar $^{7+}$  and Ar $^{6+}$  incident on Ni micro-capillaries. The blue and red lines in the middle spectra are  $Q_{in} = 6$  and  $Q_{in} = 7$  spectra, respectively. The green and black lines in the top spectra are synthetic spectra for Ni I and Ni II lines, respectively. The green, black and blue lines in the bottom spectra are synthetic spectra for Ar I, Ar II and Ar III lines, respectively. Detailed values of the wavelengths and their identifications for Ar $^{6+}$  transitions (in Ar $^{7+}$  spectra) are listed in the first and third columns in Table 3.3 (page 72).

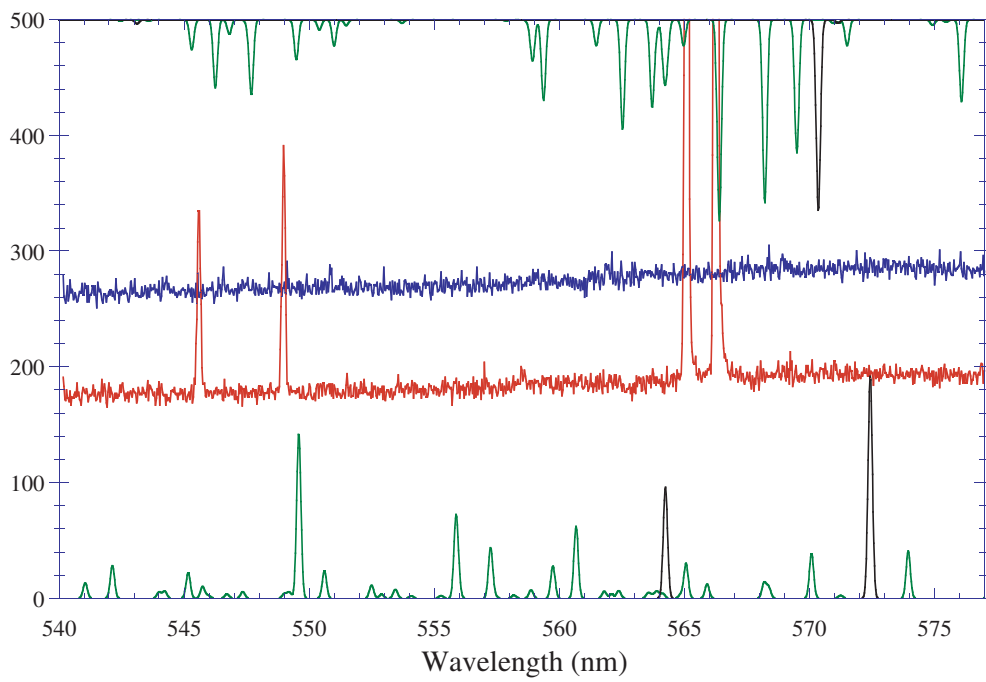
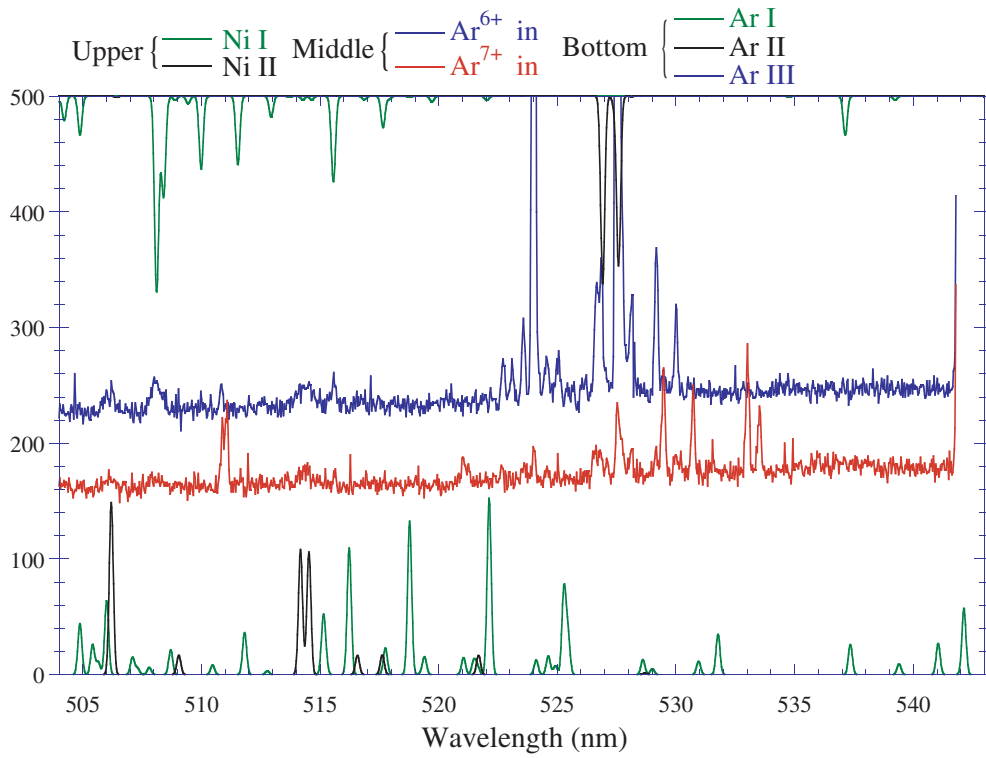
Figure C.1: Whole wavelength range spectra observed when 2.0 keV/amu  $Ar^{7+}$  (up) and  $Ar^{6+}$  (down) ions impinged on a Ni micro-capillary.

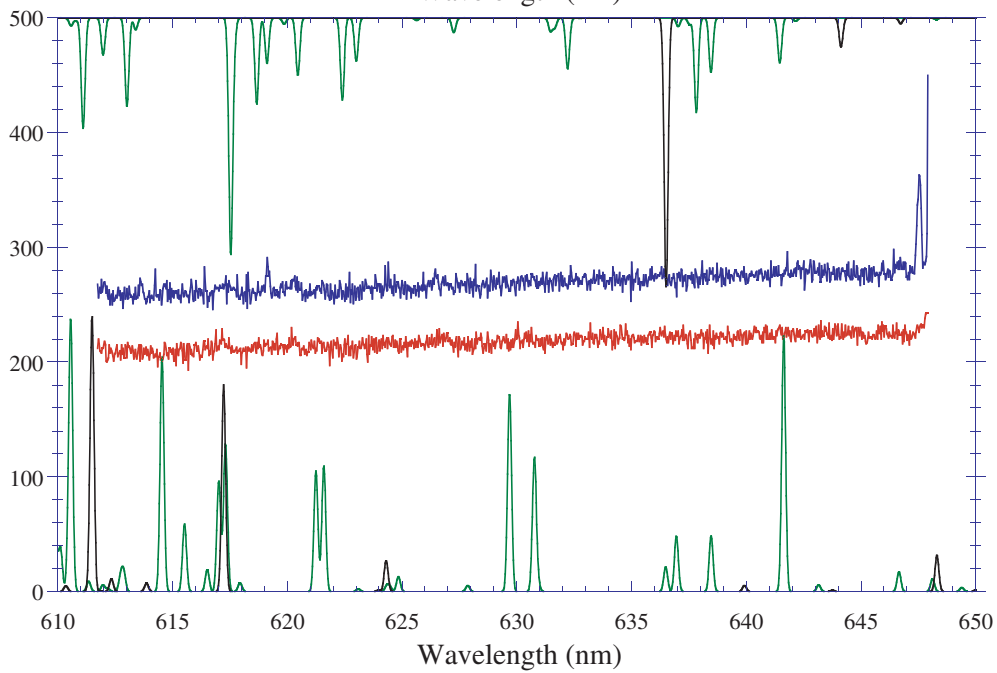
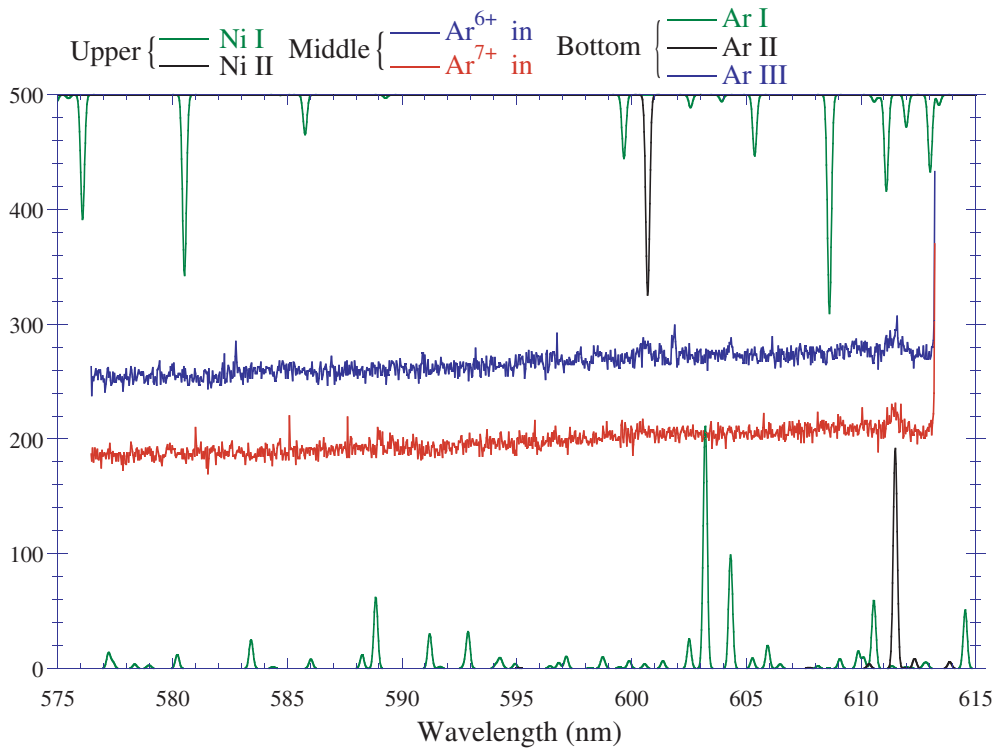


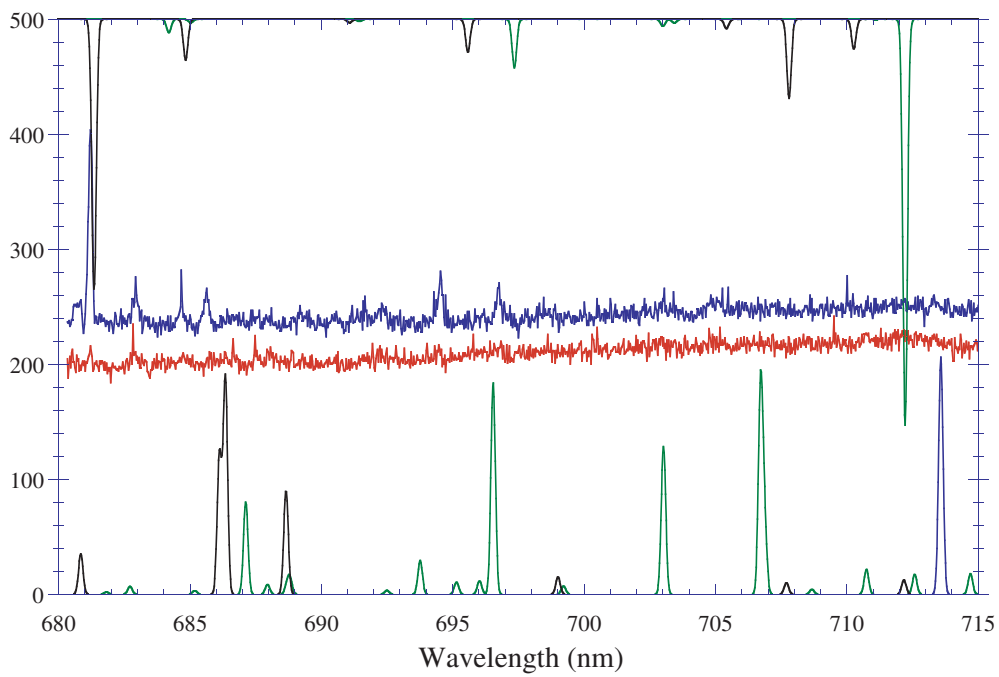
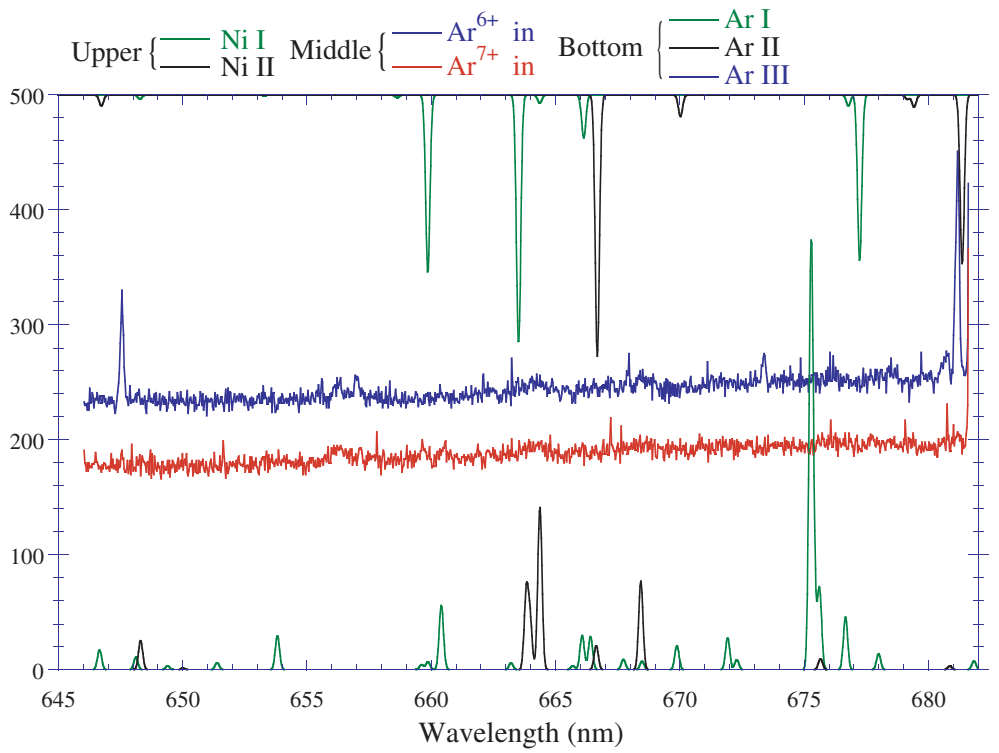


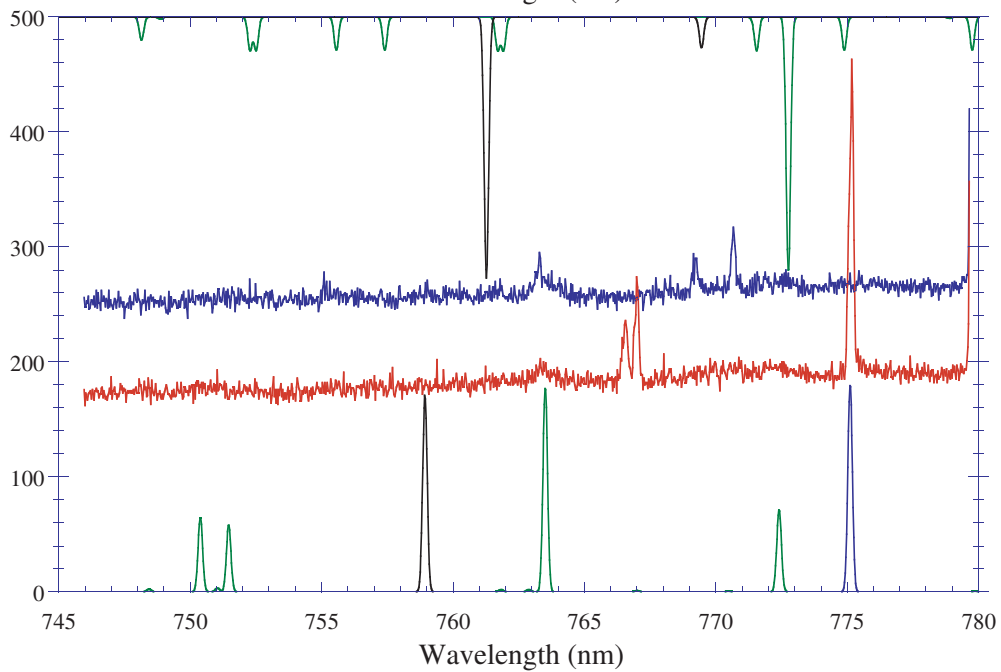
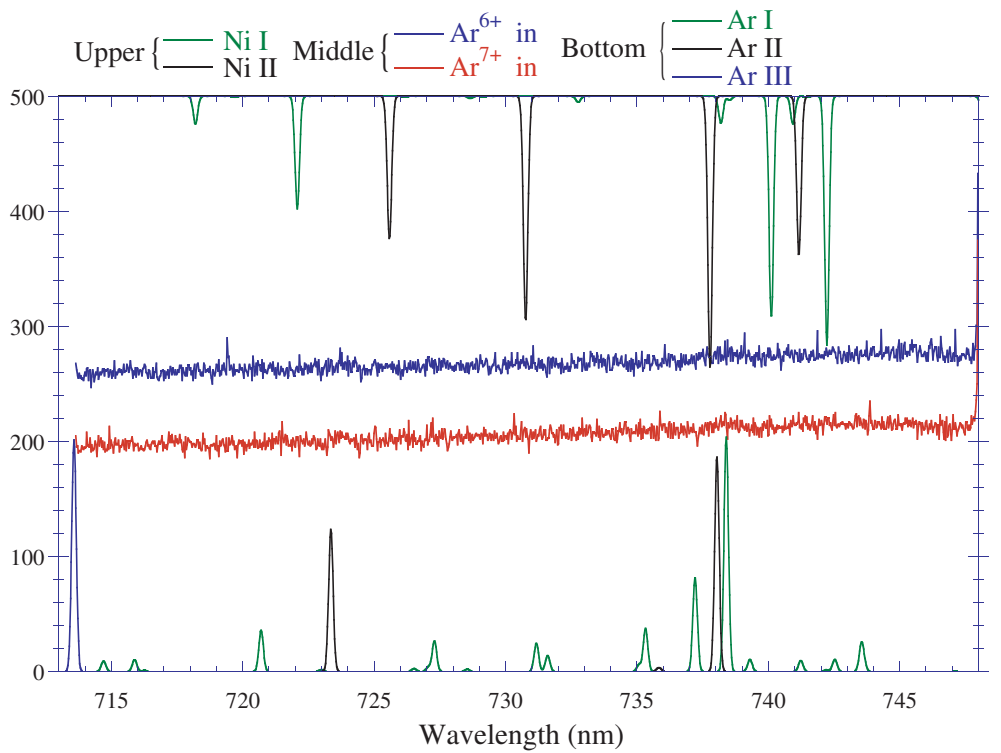


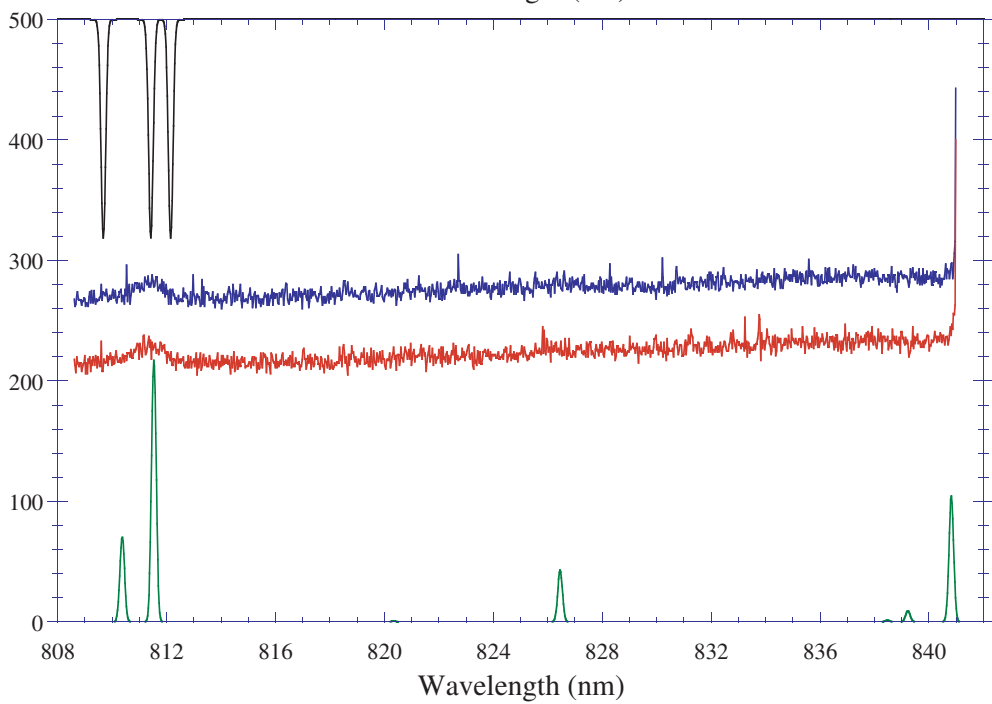
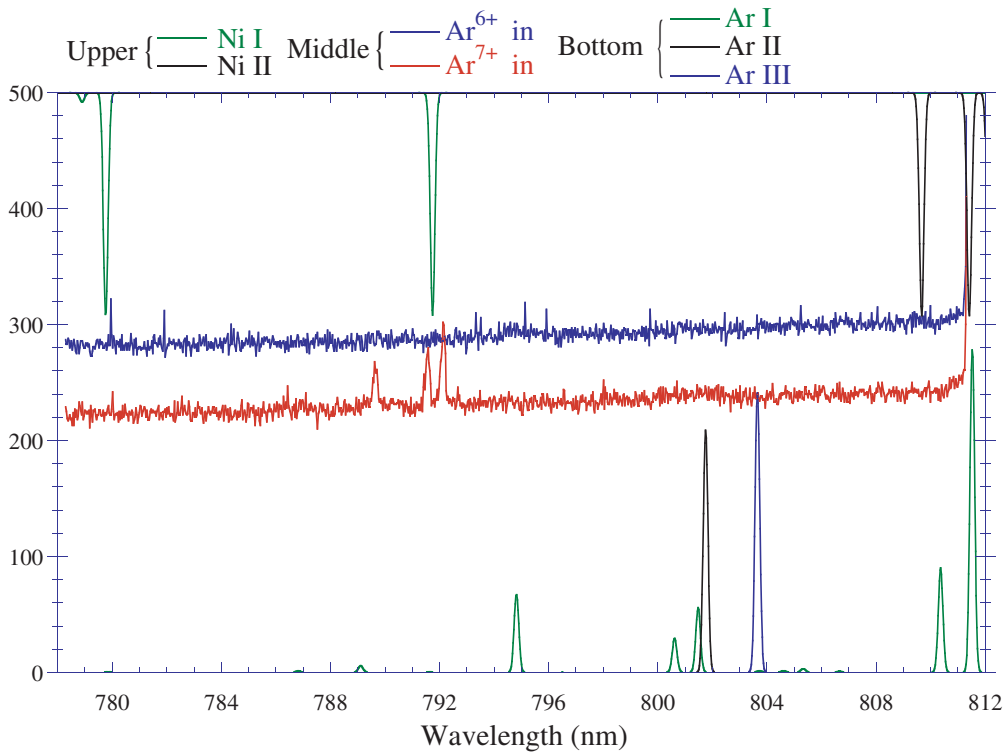












# Appendix D

## Remark

### D.1 Atomic Units

The atomic units make the quantum mechanical equations in atomic and molecular physics much simpler. Table D.1 shows atomic units for various quantities. Physical quantities, which are related to high- $n$  Rydberg atoms, are also shown in the table.

*Table D.1: Atomic units and properties of high- $n$  Rydberg atoms*

Quality	Unit	Value
Mass	$m$	$9.11 \times 10^{-31}$ kg
Charge	$e$	$1.60 \times 10^{-19}$ C
Angular momentum	$\hbar$	$1.05 \times 10^{-34}$ J s
Length	$a_0$	$5.29 \times 10^{-11}$ m
Velocity	$v_0 = \alpha c$	$2.19 \times 10^6$ m s $^{-1}$
Momentum	$p_0 = mv_0$	$1.99 \times 10^{-24}$ kg m s $^{-1}$
Time	$\frac{a_0}{v_0}$	$2.42 \times 10^{-17}$ s
Frequency	$\frac{v_0}{2\pi a_0}$	$6.58 \times 10^{15}$ s $^{-1}$
Energy	$\frac{e^2}{4\pi\epsilon_0 a_0}$	$4.36 \times 10^{-18}$ J = 27.2 eV
Wave number	$\frac{\alpha}{2\pi a_0}$	$2.19 \times 10^7$ m $^{-1}$

Quantity	Expression	Values for $n = Z = 10$
Radius	$a_0 n^2 / Z$	10
Velocity	$Zv_0 / n$	1
Orbiting time	$2\pi a_0 n^3 / Z^2 v_0$	$20\pi$
Ionization potential	$Z^2 Ry / n^2$	0.5

## D.2 Conversion of Energy

In spectroscopic study, various units are used to express the energy of a photon. In this thesis, mainly wavelength in nm is used to represent transition energies. Here conversion formulae from wavelength ( $\lambda_{vac}$ ) in nm to some quantities in other units are given.

$$\begin{aligned}
 k(cm^{-1}) &= \frac{10^7}{\lambda_{vac}} \\
 \lambda(\text{\AA}) &= 10\lambda_{vac} \\
 E(eV) &= \frac{1239.842}{\lambda_{vac}} \\
 E(a.u.) &= \frac{45.5633}{\lambda_{vac}}
 \end{aligned}$$

## D.3 Spectroscopic Notation

In a usual spectroscopy, angular momentum quantum numbers are distinguished with alphabetical letters, some of which have a historical meaning. However as is seen in our spectrum, transitions from somewhat higher angular momentum states are observed. In this thesis, angular momenta are often referred not by alphabetical letters, but by quantum numbers,  $\ell$ . The correspondence between these representations are as follows;

$n$	1	2	3	4	5	6	7	8	9	10	11	12	13
Max $\ell$	0	1	2	3	4	5	6	7	8	9	10	11	12
Alphabetical	<i>s</i>	<i>p</i>	<i>d</i>	<i>f</i>	<i>g</i>	<i>h</i>	<i>i</i>	<i>k</i>	<i>l</i>	<i>m</i>	<i>n</i>	<i>o</i>	<i>q</i>

The subsequent angular momenta are referred by letters in the alphabetical order. In atomic physics, the letter  $j$  is reserved for the total angular momentum quantum number.

Atomic species and charge state of an observed line are shown by the atomic symbol and Roman numerals, *e.g.*, Ar VIII. It is convenient in this book to remember that the Roman numerals shows the core charge.

## D.4 Terminology

<b>HCI</b>	Highly Charged Ion
<b>RN</b>	Resonant Neutralization
<b>QRN</b>	Quasi-Resonant Neutralization
<b>RI</b>	Resonant Ionization
<b>RD</b>	Radiative De-excitation
<b>AN</b>	Auger Neutralization
<b>AD</b>	Auger De-excitation
<b>AI</b>	Auto-Ionization
<b>HA1</b>	Hollow Atom above the surface
<b>HA2</b>	Hollow Atom below the surface
<b>COB model</b>	Classical Over Barrier model
<b>MCP</b>	Micro-Channel Plate
<b>EBIS</b>	Electron Beam Ion Source
<b>ECRIS</b>	Electron Cyclotron Resonance Ion Source
<b>CNS</b>	Center for Nuclear Study, University of Tokyo
<b>RIKEN</b>	Institute of Physical and Chemical Research
<b>SEM</b>	Scanning Electron Microscope
<b>PMT</b>	Photo Multiplier Tube
<b>CCD</b>	Charge Coupled Device
<b>1D/2D</b>	1/2 dimensional
<b>FWHM</b>	Full Width at Half Maximum
<b>MCHF</b>	Multi-Configuration Hartree-Fock method

# Acknowledgment

First of all, I would like to express my sincere thanks to my professors, Dr. Kenichiro Komaki (Univ. Tokyo) and Dr. Yasunori Yamazaki (Univ. Tokyo and RIKEN) for their continuous encouragements and discussions for experiments, and for their careful readings of my manuscripts. I would like to acknowledge Dr. Shiro Ninomiya (RCNP, Osaka Univ.) who taught me how to operate the Hyper-ECRIS installed in CNS(Tanashi-shi) and encouraged me during a long time when I could not observe photons from the transmitted ions. It was spiritually very hard to observe the noises or photons from sputtered Ni day after day. I would like to thank Mr. Kenro Kuroki (National Res. Inst. Police and Sci.) who made a data acquisition program in the preliminary experiment and improved it accounting for my requests. I would like to thank Dr. Hiroyuki A. Torii (Univ. Tokyo) who helped hard experiments just before the shutdown of the Hyper-ECRIS. I would like to thank Dr. Masayuki Sekiguchi (CNS, Univ. Tokyo) for his advice on experiments and on how to operate the Hyper-ECRIS. I would like to thank Dr. Kazuaki Iemura (Tokyo Electro-communications Univ.) for his help whenever the Hyper-ECRIS was in troubles, and for his friendly communications during the research life in CNS. I would like to express a special thank to Dr. Hideki Masuda (Tokyo Metropolitan Univ.) and Mr. Kouichi Yada (Tokyo Metropolitan Univ.) who supplied us nice Ni micro-capillary foils. It was never possible without the foils to observe visible lights as a result of the surface-HCI interaction. I would like to acknowledge Dr. Yasuyuki Kanai (RIKEN) who taught me how to operate the Caprice-ECRIS installed in RIKEN, and joined the experiments lasting in the late at night. I would like to acknowledge Dr. Keishi Ishii (Kyoto Univ.) and Dr. Kozo Ando (RIKEN) who taught me the techniques used in the beam-foil experiments, and recommended to use their mirror imaging system and CCD detector. I would like to thank Dr. Hirofumi Watanabe (Queen's Univ. UK) and Dr. Kiyohiko Okazaki (RIKEN) who lent me the standard deuteron and tungsten lamps, respectively. I would like to appreciate Dr. Roger Hutton (Lund Univ. Sweden) who also joined the experiments during his stay in RIKEN and informed me of a lot of spectroscopic data useful for our experiments. It was a nice experience for me to have a collaboration with foreign researchers throughout the study. I would like to thank Dr. Tomas Brage (Lund Univ. Sweden) for his first MCHF calculation of transition wavelengths and for fruitful discussions of our

spectral lines. I would like to appreciate Dr. Frank B. Rosmej (GSI, Germany) who taught me how to calculate wavelengths with the Cowan code and discussed our spectral lines. I would like to thank Dr. Alexander E. Kramida (Inst. Spectroscopy, Russia). Although we know each other only through e-mail communications, he kindly improved the Cowan code very quickly. I would like to greatly appreciate my colleagues, Dr. Takaomi Ito (Elionix), Dr. Toshiyasu Ichioka (Aarhus Univ. Denmark) and Mr. Toshiyuki Takahira (Hitachi). Although we unfortunately had no overlap in any experiment, I am very glad to spend my student life with them. Lastly I would like to thank many younger students and senior researchers of the laboratories in University of Tokyo (Komaba), CNS and RIKEN for their kind communications.

# List of Tables

2.1	<i>Parameters of Hyper ECRIS and Caprice ECRIS.</i> . . . . .	32
2.2	<i>Maximum beam currents (<math>e\mu A</math>) extractable from Hyper ECRIS for Ne and Ar ions with 20 kV extraction.</i> . . . . .	33
3.1	<i><math>\Delta n = 1</math> transition wavelengths calculated assuming energy levels as hydrogen-like and observed wavelengths. The last column shows the letters in Fig. 2.7 and Fig. 3.1.</i> . . . . .	51
3.2	<i>Wavelengths observed in the high-resolution experiment with 2.0 keV/amu <math>Ar^{8+}</math> incidence. The first and second columns show wavelengths observed and calculated by the polarization formula, respectively. The last column shows the identified <math>(n_u, \ell_u)</math> in the <math>\Delta n = \Delta \ell = 1</math> transition.</i> . . . . .	59
3.3	<i>Wavelengths observed in the high-resolution experiment with 2.0 keV/amu <math>Ar^{7+}</math> incidence. Precisions of the wavelengths are <math>\sim 0.1</math> nm. The first and second columns show wavelengths observed and those calculated with the MCHF code. <math>3\ell 3\ell' + 3sn\ell</math> (<math>n = 4 - 11</math>) + <math>3pn\ell</math> (<math>n = 4 - 6</math>) + <math>3dn\ell</math> (<math>n = 4 - 5</math>) configurations were taken into account in the calculation. The last column shows identified <math>(n_u, \ell_u)</math> in the <math>\Delta n = \Delta \ell = 1</math> transitions.</i> . . . . .	72
4.1	<i>Transition rates (in <math>10^8 \text{ sec}^{-1}</math>) and lifetimes of <math>Ar^{7+}</math> by the HF calculation. The rates and lifetimes for <math>n_u = 8</math> and 9 transitions are compared with those of hydrogen-like ions.</i> . . . . .	77
4.2	<i>Transition rates and lifetimes of <math>Ar^{6+}</math> by the MCHF calculation (see text).</i>	78
4.3	<i>Energy difference, <math>\Delta E_\ell = E_{n-1} - E_\ell</math>, between <math>\ell = n - 1</math> and <math>\ell</math> states (in a.u.) of the <math>Ar^{7+}</math> and <math>Ar^{6+}</math> ions calculated with the MCHF code. The last column shows Stark splitting for each <math>n</math>. <math>a(b)</math> shows <math>a \times 10^{-b}</math>.</i> . . . . .	89
D.1	<i>Atomic units and properties of high-<math>n</math> Rydberg atoms</i> . . . . .	108

# List of Figures

1.1	<i>Total secondary electron yield as a function of incident charge <math>Z</math> (A) and that as a function of the total potential energy stored in the HCIs (B) [2]. . . . .</i>	6
1.2	<i>Possible and elementary electron transfer-, ionization- and de-excitation-processes for ions in front of the metallic surface [5]. . . . .</i>	7
1.3	<i>X-ray spectrum when <math>Ar^{17+}</math> ions were incident onto a beryllium target [13].</i>	8
1.4	<i>High-resolution spectra [16] observed with <math>Ar^{17+}</math> ions impinging on a silver target at normal incidence (A) and grazing angle incidence, (<math>\mathcal{P}</math>), (B) . . . . .</i>	9
1.5	<i>(a): K-Auger electron spectra observed for various grazing angles of incidence of 4.3 keV/amu <math>N^{6+}</math> ions on a gold surface. (b): Above-surface component [19]. . . . .</i>	11
1.6	<i>Energy position of the center of the above-surface component and that of half maximum at the high energy side of the subsurface component as a function of the detection angle [20]. . . . .</i>	12
1.7	<i>Intensity of the above-surface component (<math>\square</math>) and total Auger electrons (<math>\blacksquare</math>) at various detection angles [22]. . . . .</i>	13
1.8	<i>Total potential experienced by an active electron when an HCI with <math>Q_{in} = 10</math> is located at <math>R = 20</math>. . . . .</i>	15
1.9	<i>(A): Schematic [28] drawing of a reflection angle measurement, and (B): energy gain as a function of the incident charge deduced from reflection angle measurements (<math>Q \leq 36</math>) [28, 29, 30, 31] and from secondary electron measurements (closed circle) [32]. . . . .</i>	17
1.10	<i>Total secondary yield, <math>\gamma</math>, vs inverse normal projectile velocity, <math>v_p</math>, for impact of <math>Th^{71+}</math> on a polycrystalline gold surface [32]. . . . .</i>	19
1.11	<i>Photographs of an micro-capillary target by the scanning electron microscope. The left figure was taken in front of the surface, and the right one taken at a diagonal angle. . . . .</i>	21
1.12	<i>Possible process expected in capillary-HCI collision. . . . .</i>	22

1.13	(A) Ne K X-rays emitted downstream of the capillary (closed circle) and those emitted from the entrance surface of the capillary (solid line). (B) Decay curve of the integrated K X-ray yield [44]. . . . .	23
1.14	A target with comparatively uniform in diameter and regularly distributed capillaries. . . . .	24
1.15	Charge state distributions under injection of 800 eV/q Xe <sup>6+</sup> ions to the random target (A), and to the uniform target (B). Theoretical predictions based on the COB model are also shown. . . . .	25
1.16	(A): Experimental configuration. (B): Angular distributions of transmitted Ne <sup>7+</sup> ions for an insulator (broader peaks) and metallic (narrower peaks) capillaries. (C): Time variation of the transmitted Ne <sup>7+</sup> ions. Stored charges on the capillary wall are saturated at ~ 10 min. After the stop of the incident beam, the stored charges dissipate with a time constant of 40 min. . . . .	26
1.17	Wavelengths for $\Delta n = 1$ transitions with their upper principal quantum numbers of $n_u$ for various core charges ( $8 \leq Q_{in} \leq 20$ ). Initial states, which is expected from the COB model to populate most effectively ( $n_c \approx Q_{in} + 1$ ), are connected with the solid line. This shows that the micro-capillary method can serve not only as a tool for the study of electron transfer processes, but also as a visible light source of highly charged ions with various charge states. . . . .	28
2.1	Schematic [57] of (A) an Electron Beam Ion Source (EBIS) and (B) an Electron Cyclotron Resonance Ion Source (ECRIS). . . . .	30
2.2	Ion intensities vs charge states of Xe extracted from ECRIS and EBIS [63].	31
2.3	Schematic [60] of the Hyper ECRIS at Center for Nuclear Study (CNS), University of Tokyo. . . . .	32
2.4	Schematic [60] of the beam-line at Center for Nuclear Study (CNS), University of Tokyo. . . . .	34
2.5	Schematic of the beam-line at atomic physics laboratory, RIKEN [64, 65].	35
2.6	(A) An illustration of the experimental set-up used in the feasibility study. (B) A schematic around the micro-capillary. . . . .	36
2.7	Spectra obtained for the first time in the feasibility study. The incident ions were $10 \times Q_{in}$ keV Ar <sup><math>Q_{in}+</math></sup> ( $8 \leq Q_{in} \leq 11$ ) ions. . . . .	37
2.8	(A) A schematic of the improved set-up. (B) A photograph of it. Each apparatus is placed in the same direction for both figures. . . . .	39
2.9	(A) Reflectivity of mirrors and (B) transmittivity of the optical lens. . .	40
2.10	Quantum efficiencies of (A) PMTs, (B) front illuminated CCD and (C) back illuminated CCD. . . . .	41
2.11	A CCD image of the reticle on the beam trajectory. . . . .	42

2.12	<i>Doppler shift and broadening.</i>	42
2.13	<i>Spectra for (A) 0.1 sec and (B) 300 sec exposure time.</i>	43
2.14	<i>(A): Spectra for 1D (below) and 2D (above) readout with the same exposure time. (B): 1D spectrum under a 500 sec exposure.</i>	44
2.15	<i>Distribution of the dark and hot pixels in the present CCD.</i>	45
2.16	<i>Transmission efficiencies of the cut-off filters for (A) 300 nm and (B) 500 nm.</i>	46
2.17	<i>Relative detection efficiencies for gratings of 300-nm blaze (<math>\circ</math>) and 500-nm blaze (<math>\square</math>).</i>	47
3.1	<i>Spectra observed with 2.0 keV/amu <math>Ar^{Q_{in}^+}</math> ions (<math>6 \leq Q_{in} \leq 10</math>). The ordinate of each spectrum is proportional to the number of the emitted photons. Lines labeled by alphabetical letters are identified as <math>\Delta n = 1</math> transitions, and transitions represented as <math>n_u = Q_{in} + s</math> (<math>-1 \leq s \leq 3</math>) are connected with the solid lines. Lines labeled by dashed letters indicates transitions after multiple electron capture, which are connected by dashed lines. Lines labeled by 2 represent the second order diffraction.</i>	49
3.2	<i>Wavelengths for <math>\Delta n = 2</math> transitions with <math>n_u = Q_{in} + 4</math>.</i>	50
3.3	<i>Two spectra in the middle show observed spectra when 2.0 keV/amu <math>Ar^{6+}</math> (blue) and <math>Ar^{7+}</math> (red) ions impinged onto the capillary. Top and bottom spectra are synthetic spectra generated using tabulated data. Lines around 335 nm were attributed to transitions from Ni I (green) and the lines around 450 nm to transitions from Ar II (black). A fact that observed lines have the same intensities for <math>Ar^{6+}</math> and <math>Ar^{7+}</math> incidences, shows that these atoms/ions are formed in the kinetic sputtering process.</i>	53
3.4	<i><math>Q_{in} = 8</math> spectra for <math>n_u = 8</math> (A), 9 (B) and 10 (C) transitions. In each figure, bars with "Polarization" show transition wavelengths calculated by the polarization formula given by Eq. 3.5 with <math>\alpha_d = 0.0314</math> and <math>\alpha_q = 0.0313</math>.</i>	56
3.5	<i><math>Q_{in} = 7</math> spectra for <math>n_u = 7</math> (A), 8 (B), 9 (C) and 10 (D) transitions. Bars marked by Theoretical and Estimated show wavelengths calculated by the polarization formula with theoretical parameters and those evaluated experimentally, respectively.</i>	57

3.6	<i>Comparisons of energy levels between singly and doubly excited <math>Ar^{6+}</math> (A) and <math>Ar^{7+}</math> (B) ions. The hatched area in each figure corresponds to energy levels to be populated. It is expected from the figures that due to a large energy difference in the <math>Ar^{8+}</math> core (252.1 eV in (B)), singly excited states of <math>Ar^{7+}</math> ions can be described better with a hydrogen-like wave function, however levels involved in the observed transitions in <math>Ar^{6+}</math> ions are perturbed more strongly by doubly excited states of <math>3p5\ell ..</math> levels, which is expected to be a reason why polarization formula is unsuitable for the prediction of the observed line positions. . . . .</i>	62
3.7	<i>Results of the MCHF calculations around <math>\Delta n = 1</math> transitions with <math>n_u = 7</math> when included configuration spaces were varied. Numbers written at the side of lines show angular momentum quantum numbers, <math>\ell_u</math>, for upper states involved in transitions. Changes of line positions are chased by the dotted lines. As was expected in Fig. 3.6(A), the drastic change takes place when <math>3pn\ell</math> (<math>n = 4 - 6</math>) configurations are taken into account in figure (B). . . . .</i>	64
3.8	<i><math>Q_{in} = 6</math> (top), <math>Q_{in} = 7</math> (middle) and synthetic spectra (bottom) around <math>\Delta n = 1</math> transitions with <math>n_u = 10</math> of <math>Ar^{6+}</math> ions. . . . .</i>	66
3.9	<i><math>Q_{in} = 6</math> (top), <math>Q_{in} = 7</math> (middle) and synthetic spectra (bottom) around <math>\Delta n = 1</math> transitions with <math>n_u = 9</math> of <math>Ar^{6+}</math> ions. . . . .</i>	67
3.10	<i><math>Q_{in} = 6</math> (top), <math>Q_{in} = 7</math> (middle) and synthetic spectra (bottom) around <math>\Delta n = 1</math> transitions with <math>n_u = 8</math> of <math>Ar^{6+}</math> ions. . . . .</i>	67
3.11	<i><math>Q_{in} = 6</math> (top), <math>Q_{in} = 7</math> (middle) and synthetic spectra (bottom) around <math>\Delta n = 1</math> transitions with <math>n_u = 7</math> of <math>Ar^{6+}</math> ions. . . . .</i>	68
3.12	<i><math>Q_{in} = 6</math> (top), <math>Q_{in} = 7</math> (middle) and synthetic spectra (bottom) around <math>\Delta n = 2</math> transitions with <math>n_u = 10</math> of <math>Ar^{6+}</math> ions. . . . .</i>	68
3.13	<i><math>Q_{in} = 6</math> (top), <math>Q_{in} = 7</math> (middle) and synthetic spectra (bottom) around <math>\Delta n = 2</math> transitions with <math>n_u = 11</math> of <math>Ar^{6+}</math> ions. . . . .</i>	69
3.14	<i>A Beam foil spectrum [97] observed with impinging 10 MeV <math>Ne^{2+}</math> ions to a thin carbon foil. . . . .</i>	70
4.1	<i>A simplified sketch of the experiment . . . . .</i>	74
4.2	<i>The observed line intensities (circles) for the transition with <math>n_u = 9</math> and <math>\ell_u = 8</math> of <math>Ar^{6+}</math> ions. The observed intensities are larger than those calculated assuming no cascading re-population. . . . .</i>	75
4.3	<i>An energy diagram for <math>Ar^{6+}</math> ions. The solid lines correspond to the transitions observed in Chapter 3. The number shown along the lines shows the number of the resolvable fine-structure components. Region I and II show the group of lines observed in each measurement. . . . .</i>	79

4.4	<i>Decay-curves for <math>\Delta n = 1</math> transitions with <math>7 \leq n_u \leq 10</math> in the region I (Figure 4.3). Left and right side figures correspond to transitions with <math>\ell_u = n_u - 1</math> and <math>n_u - 2</math> states, respectively. Open circles with error bars show measured line intensities and solid lines show analytical decay-curves obtained using the least squares methods. . . . .</i>	80
4.5	<i>Line intensities of Ar VII spectra observed when 2.0 keV/amu <math>Ar^{7+}</math> incident ions were used. . . . .</i>	81
4.6	<i>(A) Analytic decay curves of <math>n_u = 9</math> transitions when the MCHF lifetimes were used. (B) Intensity variations for <math>\ell_u = 5</math> and 6 transitions with <math>n_u = 9</math>. <math>\ell_u = 5</math> transition is reproduced with the evaluated lifetime of the (9, 5) state. . . . .</i>	82
4.7	<i>Line intensities of Ar VII spectra observed when 0.88 keV/amu <math>Ar^{7+}</math> ions impinged. . . . .</i>	83
4.8	<i>Line intensities of Ar VIII spectra observed when 2.0 keV/amu <math>Ar^{8+}</math> ions impinged. Because lines with <math>\ell_u \geq 6</math> were not resolved with the present set-up, it is assumed in the analysis that these states are populated according to their statistical weights, and the solid line in each figure shows summed intensity over these states. . . . .</i>	84
4.9	<i>Initial state distributions of the first electron transfer obtained by fitting the decay-curves in Fig. 4.4. The closed circles and squares correspond to <math>\ell = n - 1</math> and <math>n - 2</math> states, respectively. Decay-curves from <math>n \geq 11</math> states were not measured and, hence, <math>n = 11</math> populations were included to reproduce the other decay-curves and to represent populations with <math>n \geq 11</math>. . . . .</i>	85
4.10	<i>Initial state distributions obtained when 2.0 keV/amu (A) and 0.88 keV/amu (B) <math>Ar^{7+}</math> ions impinged (corresponding to decay-curves in Fig. 4.5 and 4.7, respectively). Although incident velocities are 1.5 times different, there is no remarkable change in the distributions. Both distributions have a peak around <math>n \approx 8.5</math> with the width of <math>\delta n \approx 2</math>. . . . .</i>	86
4.11	<i>Initial state distributions when 2.0 keV/amu <math>Ar^{8+}</math> ions impinged (from decay-analysis in Fig. 4.8). The distributions have a peak around <math>n \approx 9.5</math> with the width of <math>\delta n \approx 2</math>. . . . .</i>	87
4.12	<i>The critical principal quantum number, <math>n_c(\circ)</math>, predicted by the COB model as a function of the incident charge, <math>Q_{in}</math>. Observed average quantum numbers <math>\langle n_{av} \rangle(\blacksquare)</math> are also shown. The <math>\langle n_{av} \rangle</math> values agree quite well with the COB model. The COB prediction is approximately given by <math>n_c \approx Q_{in} + 1.3</math> around <math>Q_{in}</math> studied, which suggests that the COB prediction holds even for <math>Q_{in} = 9</math> and 10 (see text ). . . . .</i>	88

4.13	<i>Energy variations of the two extreme Stark states with <math>n</math> from <math>Q_{in}</math> to <math>Q_{in} + 4</math> as a function of the incident charge <math>Q_{in}</math>. The thin line denoted by <math>E_{COB}</math> shows the energy for the first electron transfer. . . . .</i>	90
4.14	<i>The energy diagram of the hydrogen-like <math>Q_{in} = 8</math> ion in the electronic field <math>F = W^2/8</math>. Numbers in the top show magnetic quantum numbers of the states. <math>E_{COB}</math> is for <math>Q_{in} = 8</math>. . . . .</i>	91
4.15	<i>Sum of squared coefficients, <math>c_i^2</math>, for states involved in the energy <math>E_{COB} - \delta E/2 \leq E \leq E_{COB} + \delta E/2</math>. The open squares and open circles correspond to <math>n_i = 9</math> and 10 states, respectively. . . . .</i>	92
C.1	<i>Whole wavelength range spectra observed when 2.0 keV/amu <math>Ar^{7+}</math> (up) and <math>Ar^{6+}</math> (down) ions impinged on a Ni micro-capillary. . . . .</i>	99

# Bibliography

- [1] M. Inokuti. *Rev. Mod. Phys.*, **43**:297, (1971).
- [2] U. A. Arifov, É. S. Mukhamadiev, É. S. Parilis and A. S. Pasyuk. *Sov. Phys. Tech. Phys.*, **18**:240, (1973).
- [3] U. A. Arifov, L. M. Kishinevskii, É. S. Mukhamadiev and É. S. Parilis. *Sov. Phys. Tech. Phys.*, **18**:118, (1973).
- [4] H. D. Hagstrum. *Phys. Rev.*, **96**:336, (1954).
- [5] P. Varga. *Appl. Phys.*, **A 44**:31, (1987).
- [6] C. D. Lin, editor. *Review of Fundamental Processes and Applications of Atoms and Ions*. World Scientific, (1993).
- [7] J. Gillaspay, editor. *Trapping Highly Charged Ions: Fundamentals and Applications*. Nova Science Publishers, (1999).
- [8] A. Arnau, F. Aumayr, P. M. Echenique, M. Grether, W. Heiland, J. Limburg, R. Morgenstern, P. Roncin, S. Schippers, R. Schuch, N. Stolterfoht, P. Varga, T. J. M. Zouros and HP. Winter. *Surf. Sci. Rep.*, **27**:113, (1997).
- [9] HP. Winter and F. Aumayr. *J. Phys. B: At. Mol. Opt. Phys.*, **32**:R39, (1999).
- [10] H. Winter. *J. Phys.: Condens. Matter*, **8**:10149, (1996).
- [11] J. D. Gillaspay. *J. Phys. B: At. Mol. Opt. Phys.*, **34**:R93, (2001).
- [12] M. O. Krause. *J. Phys. Chem. Ref. Data*, **6**:307, (1979).
- [13] E. D. Donets. *Nucl. Instrum. Meth. Phys. Res., Sect. B*, **9**:522, (1985).
- [14] C. P. Bhalla. *Phys. Rev. A*, **8**:2877, (1973).
- [15] J. P. Briand, L. de Billy, P. Charles, S. Essabaa, P. Briand, R. Geller, J. P. Desclaux, S. Bliman and C. Ristori. *Phys. Rev. Lett.*, **65**:159, (1990).

- [16] B. d'Etat, J. P. Briand, G. Ban, L. de Billy, J. P. Desclaux and P. Briand. *Phys. Rev. A*, **48**:1098, (1993).
- [17] L. Folkerts and R. Morgenstern. *Europhys. Lett.*, **13**:337, (1990).
- [18] H. J. Andrä, A. Simionovici, T. Lamy, A. Brenac, G. Lamboley, J. J. Bonet, A. Fleury, M. Bonnefoy, M. Chassevent, S. Andriamonje and A. Pasnelle. *Z. Phys. D*, **21**:S135, (1991).
- [19] F. W. Meyer, S. H. Overbury, C. C. Havener, P. A. Zeijlmans van Emmichoven and D. M. Zehner. *Phys. Rev. Lett.*, **67**:723, (1991).
- [20] J. Das and R. Morgenstern. *Phys. Rev. A*, **47**:R755, (1993).
- [21] R. Köhrbrück, N. Stolterfoht, S. Schippers, S. Hustedt, W. Heiland, D. Lecler, J. Kemmler and J. Bleck-Neuhaus. *Phys. Rev. A*, **48**:3731, (1993).
- [22] M. Grether, A. Sieler, R. Köhrbrück and N. Stolterfoht. *Phys. Rev. A*, **52**:426, (1995).
- [23] J. Burgdörfer, P. Lerner and F. W. Meyer. *Phys. Rev. A*, **44**:5674, (1991).
- [24] H. Ryufuku, K. Sasaki and T. Watanabe. *Phys. Rev. A*, **21**:7451, (1980).
- [25] A. Bárány, G. Astner, H. Cederquist, H. Danared, S. Huldt, P. Hvelplund, A. Johnson, H. Knudsen, L. Liljeby and K. -G. Rensfelt. *Nucl. Instrum. Meth. Phys. Res. Sect. B*, **9**:397, (1985).
- [26] A. Niehaus. *J. Phys. B: At. Mol. Opt. Phys.*, **19**:2925, (1986).
- [27] J. Burgdörfer, R. Morgenstern and A. Niehaus. *J. Phys. B: At. Mol. Opt. Phys.*, **19**:L507, (1986).
- [28] H. Winter. *Europhys. Lett.*, **18**:207, (1992).
- [29] H. Winter, C. Auth, R. Schuch and E. Beebe. *Phys. Rev. Lett.*, **71**:1939, (1993).
- [30] F. W. Meyer, L. Folkerts, H. O. Folkerts and S. Schippers. *Nucl. Instrum. Meth. Phys. Res. Sect. B*, **98**:441, (1995).
- [31] F. W. Meyer, L. Folkerts and S. Schippers. *Nucl. Instrum. Meth. Phys. Res. Sect. B*, **100**:366, (1995).
- [32] H. Kurz, K. Töglhofer, HP. Winter, F. Aumayr and R. Mann. *Phys. Rev. Lett.*, **69**:1140, (1992).

- [33] H. Kurz, F. Aumayr, C. Lemell, K. Töglhofer and HP. Winter. *Phys. Rev. A*, **48**:2192, (1993).
- [34] H. Kurz, F. Aumayr, HP. Winter, D. Schneider, M. A. Briere and J. W. McDonald. *Phys. Rev. A*, **49**:4693, (1994).
- [35] J. Burgdörfer and F. Meyer. *Phys. Rev. A*, **47**:R20, (1993).
- [36] C. Lemell, HP. Winter, F. Aumayr, J. Burgdörfer and F. Meyer. *Phys. Rev. A*, **53**:880, (1996).
- [37] J. Limburg, S. Schippers, R. Hoekstra, R. Morgenstern, H. Kurz, F. Aumayr and HP. Winter. *Phys. Rev. Lett.*, **75**:217, (1995).
- [38] J. P. Briand, S. Thuriez, G. Giardino, G. Borsoni, M. Froment, M. Eddrief and C. Sébenne. *Phys. Rev. Lett.*, **77**:1452, (1996).
- [39] F. Aumayr, HP. Winter, J. Limburg, R. Hoekstra and R. Morgenstern. *Phys. Rev. Lett.*, **79**:2590, (1997).
- [40] H. Masuda, H. Yamada, M. Satoh and H. Asoh. *Appl. Phys. Lett.*, **71**:2770, (1997).
- [41] H. Masuda, K. Yada and A. Osaka. *Jpn. J. Appl. Phys.*, **37**:L1340, (1998).
- [42] S. Ninomiya, Y. Yamazaki, F. Koike, H. Masuda, T. Azuma, K. Komaki, K. Kuroki and M. Sekiguchi. *Phys. Rev. Lett.*, **78**:4557, (1997).
- [43] S. Ninomiya. *Study of hollow atom; its formation and decay*. PhD thesis, University of Tokyo, (1997).
- [44] Y. Yamazaki, S. Ninomiya, F. Koike, H. Masuda, T. Azuma, K. Komaki, K. Kuroki and M. Sekiguchi. *J. Phys. Soc. Jpn.*, **65**:1199, (1996).
- [45] Y. Yamazaki. *Physica Scr.*, **T73**:293, (1997).
- [46] Y. Yamazaki. *Int. J. Mass Spec.*, **192**:437, (1999).
- [47] Y. Iwai. Study of hollow atom using high resolution soft x-ray spectrometer. Master's thesis, University of Tokyo, (1999).
- [48] S. Thuriez, Y. Iwai, Y. Kanai, H. Oyama, R. Hutton, H. Masuda and Y. Yamazaki. In *Abstracts of contributed papers XXI-ICPEAC Sendai, Japan, (1999)*.
- [49] R. Hutton, S. Thuriez, Y. Iwai, Y. Kanai, H. Oyama, H. Masuda and Y. Yamazaki. In *Abstracts of contributed papers XXI-ICPEAC Sendai, Japan, (1999)*.

- [50] D. Murakoshi. Study of multiple electron transfer processes to highly charged ions with microcapillary targets. Master's thesis, University of Tokyo.
- [51] D. Murakoshi, Y. Kanai, Y. Morishita, Y. Iwai, N. Okabayashi, H. A. Torii, K. Nishio, H. Masuda, M. Nakao, T. Tamamura, K. Tókési, L. Wirtz, C. Lemell, J. Burgdörfer, K. Komaki and Y. Yamazaki. In *Abstracts of contributed papers XXII-ICPEAC*, page 504. Rinton Press.
- [52] Y. Iwai, D. Murakoshi, Y. Kanai, H. Oyama, K. Ando, H. Masuda, M. Nakao, T. Tamamura, K. Komaki and Y. Yamazaki. *Nucl. Instrum. Meth. Phys. Res. Sect. B*, **193**:504, (2002).
- [53] K. Tókési, L. Wirtz, C. Lemell and J. Burgdörfer. *Phys. Rev. A*, **61**:020901(R), (2000).
- [54] K. Tókési, L. Wirtz, and J. Burgdörfer. *Nucl. Instrum. Meth. Phys. Res. Sect. B*, **154**:307, (1999).
- [55] K. Tókési, L. Wirtz, C. Lemell and J. Burgdörfer. *Phys. Rev. A*, **64**:042902, (2001).
- [56] N. Stolterfoht, J. -H. Bremer, V. Hoffman, R. Hellhammer, D. Fink, A. Petrov and B. Sulik. *Phys. Rev. Lett.*, **88**(13):133201, (2002).
- [57] R. Geller. *Annu. Rev. nucl. Part. Sci.*, **40**:15, (1990).
- [58] E. D. Donets. *The Physics And Technology Of Ion Sources*, chapter 12. John Wiley & Sons, Inc., (1989).
- [59] R. E. Marrs, S. R. Elliott, and D. A. Knapp. *Phys. Rev. Lett*, **72**:4082, (1994).
- [60] M. Sekiguchi, Y. Ohshiro, M. Fujita, T. Yamazaki, Y. Yamashita, Y. Isoya, T. Yamada, and A. Kitagawa. In *Proceedings of the 12th International Conference on Cyclotrons and their applications, Vancouver*, (1992).
- [61] G. Shirkov. In *Proceedings of the 11th International Workshop on Electron Cyclotron Resonance Ion Sources (ECRIS11), Groningen*, page 66, (1993).
- [62] A. G. Drentje. *Rev. Sci. Instrum.*, **63**(4):2875, (1992).
- [63] V. B. Kunter. *Rev. Sci. Instrum.*, **65**:1039, (1994).
- [64] Y. Kanai, D. Dumitriu, Y. Iwai, T. Kambara, M. Kitajima, TM. Kojima, A. Mohri, Y. Morishita, Y. Nakai, N. Oshima, H. Oyama, M. Wada, and Y. Yamazaki. *Riken Rev.*, **31**:62, (2000).

- [65] Y. Kanai, D. Dumitriu, Y. Iwai, T. Kambara, T. M. Kojima, A. Mohri, Y. Morishita, Y. Nakai, H. Oyama, N. Oshima, and Y. Yamazaki. *Physica. Scr.*, **T92**:467, (2001).
- [66] D. H. Crandall, R. A. Phaneuf, and F. W. Meyer. *Phys. Rev. A*, **22**:379, (1980).
- [67] W. Fielder, Jr., D. L. Lin and D. Ton-That. *Phys. Rev. A*, 19:741, (1979).
- [68] Y. Morishita, S. Ninomiya, Y. Yamazaki, K. Komaki, K. Kuroki, H. Masuda, and M. Sekiguchi. *Physica. Scr.*, **T80**:212, (1999).
- [69] Data sheets from a catalogue by Sigma Koki Corporation.
- [70] Data sheets from a catalogue by Hamamatsu Photonics Corporation (A), by Princeton Instruments (B), and (C).
- [71] B. Edlén. *Metrologia*, **2**:71, (1966).
- [72] J. Sugar and C. Corliss. Atomic energy levels of the iron period elements: Potassium through Nickel. *J. Chem. Ref. Data*, **14**(2), (1985). Data are compiled in the web site <http://physics.nist.gov/PhysRefData/contents.html> . .
- [73] T. Shirai, J. Sugar and A. Musgrove. Wavelengths and energy levels for all spectra of Argon (Ar I through Ar VXIII). (*unpublished*), (1999). Data are compiled in the web site <http://physics.nist.gov/PhysRefData/contents.html> .
- [74] V. Vujnović and W. L. Wiese. *J. Chem. Ref. Data*, **21**(5), (1992). Data are compiled in the web site <http://physics.nist.gov/PhysRefData/contents.html> .
- [75] *Sputtering by particle bombardment I (in Topics in applied physics, volume 47, ed. by R. Behrisch. Springer-Verlag, (1981).*
- [76] P. Williams. *Phys. Rev. B*, **23**(11):6187, (1981).
- [77] T. F. Gallagher. *Rydberg Atom*. Cambridge University Press, (1994).
- [78] B. Edlén. *Atomic Spectra, in Handbuch Der Physik*. Springer-Verlag, (1984).
- [79] G. W. F. Drake. *Long-Range Casimir Forces, Theory and Recent Experiments on Atomic Systems*. Plenum Publishing Corp, (1993).
- [80] Compiled data at <http://www.pa.uky.edu/~peter/atomic>.
- [81] K. Bockasten. *Phys. Rev. A*, **9**(3):1087, (1974).
- [82] I. Johansson. *Arikiv. Fysik*, **20**:135, (1961).
- [83] P. Risberg. *Arikiv. Fysik*, **10**:583, (1956).

- [84] B. Isberg. *Arikiv. Fysik*, **9**:483, (1955).
- [85] B. Isberg. *Arikiv. Fysik*, **35**:531, (1968).
- [86] Y. Toresson. *Arikiv. Fysik*, **17**:179, (1960).
- [87] C. E. Magnusson and P. O. Zetterberg. *Physica Scr.*, **10**:177, (1974).
- [88] B. Edlén. *Physica Scr.*, **17**:565, (1978).
- [89] E. Ya. Kononov, V. I. Kovalev, A. N. Ryabtsev and S. S. Kvantovaya. *Elektronika*, **4**:190, (1977).
- [90] L. J. Curtis. *Physica Scr.*, **21**:162, (1980).
- [91] L. J. Curtis. *Phys. Rev. A*, **23**:362, (1981).
- [92] R. L. Kelly. *J. Phys. Chem. Ref. Data*, **16**(1), (1987).
- [93] D. Layzer. *Ann. Phys.*, **8**:271, (1959).
- [94] D. Layzer, Z. Horák, M. N. Lewis and D. P. Thompson. *Ann. Phys.*, **29**:101, (1964).
- [95] R. D. Cowan. *The Theory of Atomic Structure and Spectra*. University of California Press, (1981). The original code written by Cowan is distributed at an internet web site, <ftp://aphysics.lanl.gov/pub/cowan/>. A PC version ported by Kramida is also available, which is distributed at <ftp://plasma-gate.weizmann.ac.il/pub/software/dos/cowan>.
- [96] C. F. Fischer, T. Brage and P. Jönsson. *Computational Atomic Structure; An MCHF Approach*. Institute of Physics Publishing, (1997). The original code is distributed at <http://kurslab.fysik.lu.se/casbook.html>.
- [97] A. Lapiere and E. J. Knystautas. *Physica Scr.*, **59**, (1999).
- [98] K. Ishii, S. Kawae, T. Nakano, K. Ando, H. Oyama and T. Kambara. *Physica Scr.*, T80, (1999).
- [99] We made use of a computational routine developed by R. Bauman for hydrogen-like rates. The routine is distributed at <http://nimbus.pa.uky.edu/hydrogen/>.
- [100] B. G. Baker, B. B. Johnson and G. L. C. Maire. *Surf. Sci.*, **24**, (1971).
- [101] H. A. Bethe and E. E. Salpeter. *Quantum mechanics of one- and two-electron atoms*. Plenum, (1977).